Crystal Structures, Rotational, Vibrational Dynamics, and Optoelectronic Properties of Two-Dimensional Hybrid Organic-Inorganic Perovskites

Depei Zhang

Changzhou, Jiangsu, China

Bachelor of Science in Physics, Nanjing University, June 2013

A Dissertation Presented to the Graduate Faculty of the University of Virginia in

Candidacy for the Degree of Doctor of Philosophy

Department of Physics

University of Virginia

August 2019

Abstract

Hybrid organic-inorganic perovskites (HOIPs), also known as organic metal halide perovskites (MHPs), have shown promising success in the solar cell and light-emitting diode (LED) industries by showing their remarkable photovoltaic and optoelectronic performances. The 25.2% record power conversion efficiency from the perovskite solar cells has been achieved by polycrystalline thin films produced through simple, low-cost and low-temperature methods [1-7], which have an electronic quality that is comparable to, or surpasses, that of the state-of-the-art epitaxial grown semiconductors [8-12]. On the other hand, the perovskite LEDs have shown high quantum efficiencies, with a recent record of 21.6% [13].

The long carrier lifetime and defect tolerance are the two key characteristics that are responsible for superb optoelectronic device performance in HOIPs, and yet their origins are still under intense debate. Here we show significant differences in the charge carrier dynamics between the two-dimensional (2D) and three-dimensional (3D) HOIPs, using time-resolved photoluminescence (TRPL) measurements and time-of-flight (TOF) neutron scattering measurements.

In this thesis, $(BA)_2PbI_4$ ($(C_4H_9NH_3)_2PbI_4$) and $MAPbI_3$ ($CH_3NH_3PbI_3$), the prototypes of 2D and 3D HOIPs, are selected to be the materials to study. The TRPL measurements showed short and nearly temperature-independent charge carrier lifetimes, within 0.1 ~ 1.1 ns, for the *majority* charge carriers in the 2D HOIP, $(BA)_2PbI_4$, which is in contrast with the long-lived and temperature-dependent *majority* carriers in the 3D HOIP, $MAPbI_3$. In $MAPbI_3$, the lifetimes of the *majority* charge carriers are 0.7 ~ 60 ns, which show a gradual decrease within each structural phase, while exhibits a significant

increase at the orthorhombic-to-tetragonal phase transition when a C_4 rotational mode of the MA^+ molecule gets activated [14]. The short, temperature-independent and long, temperature-dependent charge carrier lifetimes are consistent with the excitonic and polaronic pictures of the *majority* carriers in the 2D and 3D HOIPs, respectively.

On the other hands, our TOF neutron scattering measurements revealed two types of jump rotational modes for $(BA)_2PbI_4$: the C_3 modes of the NH_3, CH_3 groups with smaller rotational radii and shorter relaxation time, which exist in the entire temperature range; and the C_4 mode of the whole BA^+ molecule with larger rotational radii and longer relaxation time, which is only activated in the high-temperature phase. The C_4 mode appears right after the phase transition at 280 K upon heating, showing a characteristic relaxation time of ~ 53 ps.

Furthermore, from the TOF neutron scattering measurements, the phonon melting features were observed on both 2D and 3D HOIPs, when the phonon modes gradually lose their time coherences as the temperature increases, while the spatial correlations are still conserved. Most prominently, for the mostly-inorganic and hybrid modes, the sharp coherent phonon peaks at the base temperature become broad continuums during heating within the low-temperature phases.

Combining the TRPL measurements and the TOF neutron experiments, we conclude that the 2D HOIP, $(BA)_2PbI_4$, which is dominated by excitons, does not show correlations between PL lifetime and rotational dynamics, phonon melting. On the other hand, for the 3D HOIP in which polaronic features are prominent, the major factors which enhance the charge carrier lifetime are both the rotations of the MA^+ molecules and the liquid-like vibrations of the inorganic atoms.

Author’s Biographical Sketch

Depei Zhang was born in Changzhou, Jiangsu Province, China, on March 2nd, 1991. He started his study in physics at Nanjing University in 2009, and then received the Bachelor of Science degree in 2013. In 2014, he moved to Charlottesville, Virginia, United States, where he continued his study and research as a graduate student in the Department of Physics, University of Virginia. Then in the summer of 2015, he joined Prof. Seung-Hun Lee’s group as a Ph.D. candidate and research assistant. In Prof. Lee’s group, he studied the crystal structures, rotational, vibrational dynamics, and optoelectronic properties of two-dimensional hybrid organic-inorganic perovskites, as well as exotic behaviors in magnetic materials, including memory effects in spin glasses and magnetic orders, magnetic excitations in frustrated magnetics.

Acknowledgments

Firstly, I would like to express my sincere gratitude to Prof. Seung-Hun Lee, my Ph.D. advisor, for his continuous support of my study and research. His guidance and encouragement helped me throughout my Ph.D. period. Besides my advisor, I would like to thank the other members of my defense committee: Prof. Despina Louca, Prof. Gia-Wei Chern, Prof. Joshua J. Choi, for their insightful comments, suggestions, and questions which help improve my research from various perspectives.

Next, I thank Dr. Maiko Kofu, Dr. Craig M. Brown, Dr. Douglas L. Abernathy, Dr. Guangyong Xu, Dr. Leland W. Harriger, Dr. Ryoichi Kajimoto, Dr. Mitsutaka Nakamura and Dr. Seiko Ohira-Kawamura for their help in neutron scattering experiments. I especially thank Dr. Maiko Kofu for her tremendous effort during the neutron scattering experiments in Japan. I also give my thanks to Dr. Wei-Liang Chen and Dr. Yu-Ming Chang, for their work in the photoluminescence measurements. I would like to thank Dr. Mina Yoon for her valuable help in the density functional theory calculations. I also thank Dr. Alexander Z. Chen, Dr. Benjamin J. Foley, Dr. Chinnambedu Murugesan Raghavan, Ms. Tzu-Pei Chen and Dr. Chun-Wei Chen for providing the high-quality samples for my experiments.

My deep gratitude also goes to my fellow lab-mates, Dr. Tianran Chen, Dr. Anjana M. Samarakoon and Mr. Xiao Hu, for the days and nights we were working together, and for all the fun we shared in the past five years. I am particularly grateful to Dr. Tianran Chen, who taught me lots of experimental and calculational techniques. Furthermore, I thank my parents and all my friends for their continuous supports and encouragement during my Ph.D. period.

Finally, I acknowledge the funding sources in my research. The work at the University of Virginia was supported by the U.S. Department of Energy, Office of Science, Office of Basic Energy Sciences under Award Number DE-SC0016144. The neutron scattering experiments at the Material and Life Science Experimental Facility, Japan Proton Accelerator Research Complex was performed under a user program (Proposal No. 2017AU0101 and 2017BU1402). The research at Oak Ridge National Laboratory's Spallation Neutron Source was sponsored by the U.S. Department of Energy, Office of Basic Energy Sciences. The work at National Taiwan University was supported by the Center of Atomic Initiative for New Materials (AI-MAT) from the Featured Areas Research Center Program within the framework of the Higher Education Sprout Project by the Ministry of Education in Taiwan (108L9008). Additional supports were provided by the Ministry of Science and Technology of Taiwan (Grant No. MOST 105-2119-M-002-046-MY3 and MOST 107-2112-M-002-024-MY3). The computational work was performed by utilizing the resources at the National Energy Research Scientific Computing (NERSC) Center, which is supported by the Office of Science of the U.S. Department of Energy (Contract No. DE-AC02-05CH11231). We also acknowledge the support of the National Institute of Standards and Technology, U.S. Department of Commerce, in providing the neutron research facilities used in this work.

Table of Contents

List of Tables

List of Figures

Chapter 1.

Introduction

1.1 Introduction to Optoelectronic Devices

Optoelectronic devices are those electronic devices that operate on both light and electrical currents [15]. Based on their applications, the optoelectronic devices can fall into four categories: 1) electrically driven light sources, such as laser diodes and light-emitting diodes (LEDs); 2) components for converting the light energy to electricity, such as solar cells; 3) devices for light detection, such as optical sensors; 4) electronically controlled light propagation components, such as optical fibers and optical modulators.

Optoelectronic devices were first studied in the 1950s – 1960s, and since then, the diversity and scope of optoelectronic researches and applications have been growing steadily [16]. In the following, we will use solar cells and light-emitting diodes as two examples to introduce the development of optoelectronic devices.

1.1.1 Development in Solar Cells

Solar cell is a device that converts light energy into electrical energy. This energy conversion process is known as the photovoltaic effect, which was first discovered by A. E. Becquerel in 1839. By illuminating the AgCl (or AgBr) coated Pt electrodes, Becquerel observed the generation of voltage and current between the electrodes [17]. Within a century after Becquerel’s discovery, solar cells had drawn continuous attention from the scientists and engineers. Much work had been done in this field, including explaining the nature behind the photovoltaic effect and improving the solar cell efficiency. However, the output power remained to be so low that those solar cells can only be used for light detection.

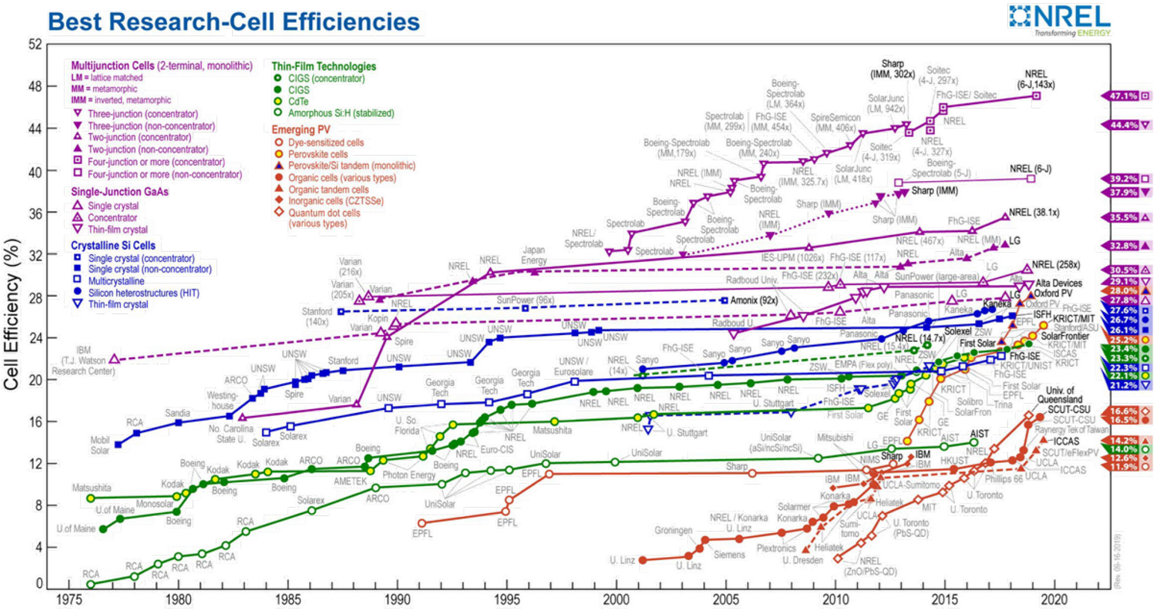

Figure 1. Best Research-Cell Efficiency.

The development of the state-of-the-art solar cells, with their efficiencies confirmed by recognized test labs. The standard measurements are performed under the IEC 60904-3 edition 2 or ASTM G173 spectrum illumination at 25 °C. The figure is obtained from Ref. [2].

The breakthrough happened in the 1940s and 1950s, when the p-n junction transistor was discovered, and impurity doping was found to improve the semiconductor's quality. The first practical working solar cell was invented in 1954, when D. M. Chapin, C. S. Fuller, and G. L. Pearson built the first Si-transistor based cell at Bell Labs [18]. By doping Ga into Si and treated with a Li bath, the Si cell showed a high efficiency, i.e., initially at 4%, and later improved to 11%. The Bell solar cell proposed a prototype for the modern high-efficiency cells, and hereafter, the cell efficiency has been growing steadily, reaching ~ 36 % for single p-n junction cells and ~ 46 % for the multi-junction cells [2, 19]. The recent development of research cell efficiency is shown in Figure 1.

Solar cells provide us a cleaner and renewable energy source than the conventional fossil fuels, however, the high cost of the solar panel is still the major impediment to their broad commercial applications. In the 1950s, not long after the invention of the Bell solar cell, the solar panels cost over \$300 per watt. Until the 1970s, the price remains above \$100 per watt. [20] During that time, the solar panels can only be used to power the satellites and for other research purposes. Since the 1980s, due to the rapid developments in manufacturing technology, especially for polymer thin films, the price of solar panels has dropped by over 10% every year. Nowadays, the cost of a solar panel is as low as \$0.5 per watt. The continuously reducing price has made solar panels a reliable power source for various industries.

1.1.2 Development in Light-Emitting Diodes

Light-emitting diode (LED) is a light source which uses the electroluminescence effect of semiconductors to generate light. The electroluminescence effect was first reported by H. J. Round in 1907, when he discovered the yellow light emission after applying an electric voltage on the SiC crystal [21]. O. V. Losev also performed an independent study on the electroluminescence phenomena, and he published a report on the light emission from SiC in the 1920s [22].

In the 1950s, along with rapid development in semiconductor diodes, the idea for light-emitting diodes appeared. At that time, GaAs and Ge were the first semiconductors used before Si became the preferred material in the industry. In 1961, J. R. Biard and G. E. Pittman at Texas Instruments made the first infrared LED by placing the tunnel diode on a

GaAs substrate. And one year later, N. Holonyack Jr. at General Electric invented the first visible red-light LED with GaAsP on a GaAs substrate. Hereafter, the LED industry started to grow vigorously; in the 1970s, the yellow-light (GaAsP) and blue-light (GaN) LEDs were invented successively by M. G. Craford and S. Nakamura.

In the 1960s, the electroluminescence effect on organic materials was discovered [23]. The first organic light-emitting diode (OLED) was made in 1987, by C. W. Tang and S. V. Slyke at Kodak [24]. The OLED they made had a sandwiched structure, which consists of an organic material layer and two transparent electrodes. The OLED is lighter and thinner than the conventional LEDs, so it has broader applications.

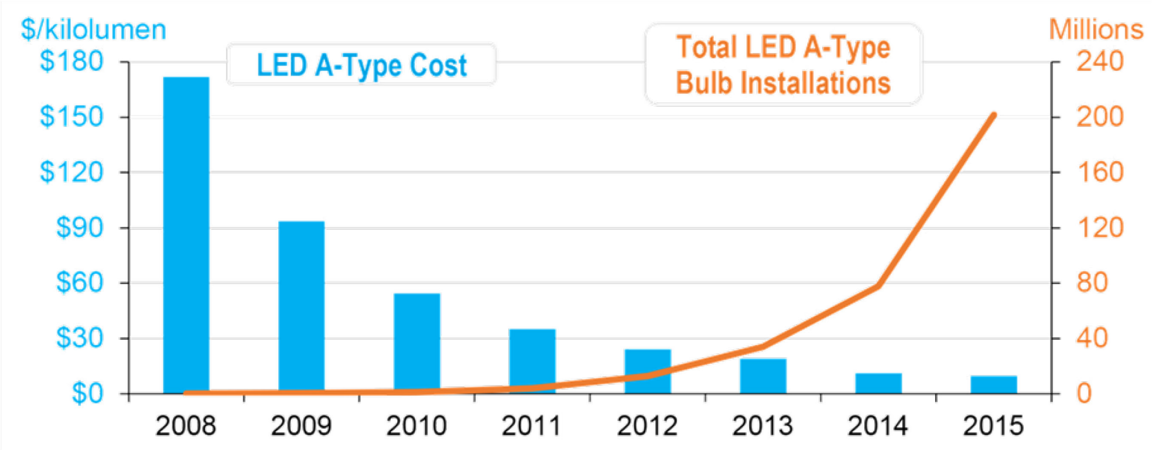

Figure 2. LED Cost and Deployment Chart.

The blue bar shows the cost of LED A-type bulb per kilolumen from the year 2008 to 2015, and the orange line represents the total installation number of LED bulbs each year. The figure is taken from Ref. [25].

As the LED technology evolves, their high energy efficiency, durability and adaptability have been improved continuously, and the cost for LED devices keeps reducing. In the 1960s, the first LED made by Texas Instruments was sold for $130, while the current price is under \$0.10 for a single LED indicator. The cost and deployment data for LED bulbs are shown in Figure 2. The reducing price encourages people to replace their conventional displays and light bulbs with the LED-based devices.

1.2 Metal Halide Perovskites

1.2.1 Perovskite Materials

Perovskite materials are referred to as a class of condensed matter materials, which has the same crystal structure as $CaTiO_3$. The generic perovskite structure can be expressed as ABX_3, where A is a large-sized cation, B is a small-sized cation, and X is an anion. At high temperatures, the unit cell of a perovskite compound usually has the cubic symmetry, where cation A and B occupy the corner and body-center position respectively, while the anion X is located at the face-center position. The ABX_3 perovskite crystal structure is shown in Figure 3.

Since the discovery of the first perovskite compound $CaTiO_3$ by L. A. Perovski in 1839, perovskite materials were mainly studied for their mechanical and electrical properties, among which the most well-known application is the high-temperature CuO_2 superconductors. However, the outstanding optoelectronic properties of perovskite materials were discovered until the 1990s. Studies on hybrid organic-inorganic perovskites revealed the high light absorption coefficient, long charge carrier diffusion length and suitable exciton binding energy of these materials [1, 14, 26-30], which have attracted massive attention to the perovskite materials for optoelectronic and photovoltaic applications.

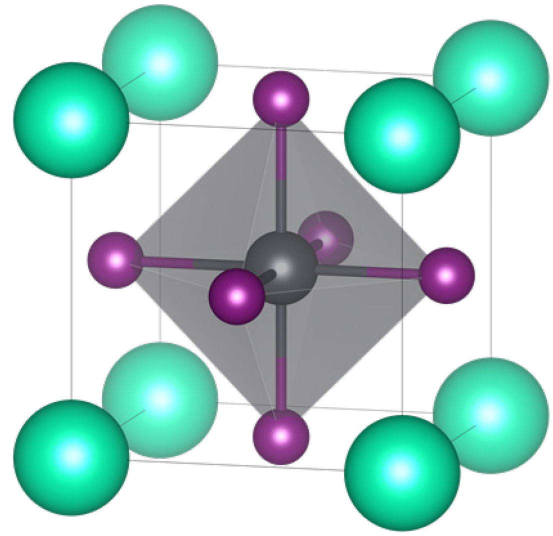

Figure 3. Perovskite Crystal Structure.

The crystal structure of the perovskite compound ABX_3*, where the cyan, gray and violet spheres represent the cation A, B and anion X.*

1.2.2 Organic Metal Halide Perovskites

Organic metal halide perovskites (MHPs), also known as the hybrid organic-inorganic perovskites (HOIPs), are crystallized from organic halide AX and metal halide BX_2 salts to form the perovskite ABX_3 structure, where A is the organic cation, B can be Pb^{2+} or Sn^{2+}, and X can be Cl^-, Br^- or I^-. The structures of the two most popular HOIPs, methylammonium lead iodide ($MAPbI_3$, $MA=CH_3NH_3$) and formamidinium lead iodide ($FAPbI_3$, $FA=HC(NH_2)_2$), are shown in Figure 4A and B, respectively.

The first studied HOIPs, $CH_3NH_3PbX_3$, were synthesized by D. Weber at the University of Stuttgart, in 1978 [31]. Until nearly two decades later, the optoelectronic properties of HOIPs were discovered and immediately gained a huge interest. In 1994, M. Era, et al. , at Kyushu University developed light-emitting devices from a layered HOIP,

$(PEA)_2PbI_4$ ($PEA=C_6H_5CH_2CH_2NH_3$), with an efficiency of 0.5 cd·A^{-1} [32]. And 2009, A. Kojima, et al., at the University of Tokyo, fabricated the first perovskite solar cell with $CH_3NH_3PbI_3$ as the light absorber, yielding a power conversion efficiency (PCE) of 3.8% [33]. In the year 2012 and 2013, due to the developments in the sensitized planar TiO_2 (charge transporter) architectures, higher efficiencies above 10% had been achieved [34, 35]. With the continuous exploration in deposition techniques and structure designs, the efficiencies are glowing in an unprecedented speed, reaching the record of 25.2% [2, 19] in September 2019 (see the red-edged circle with the yellow face filling in Figure 1).

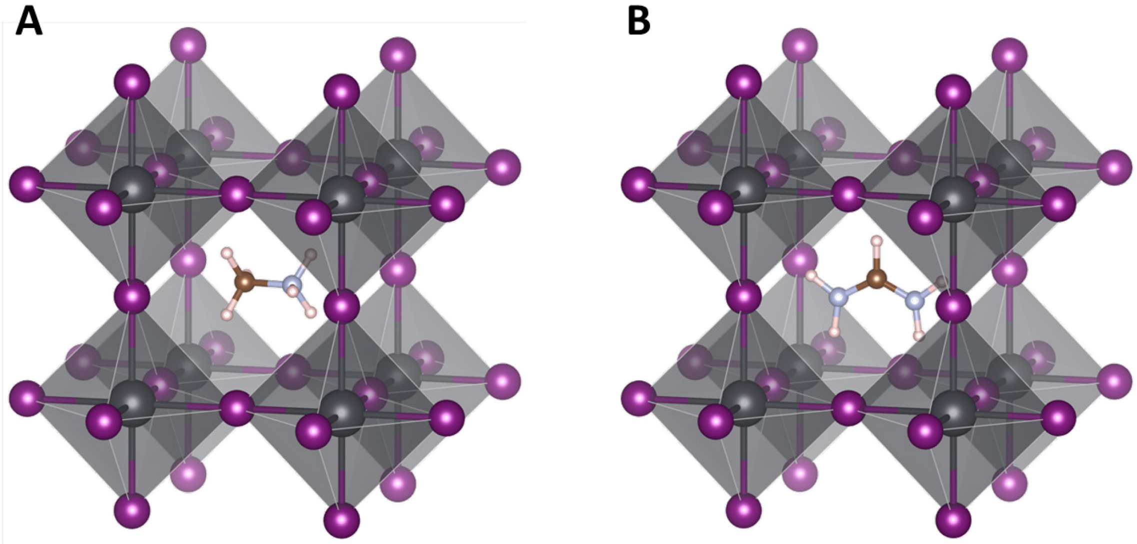

Figure 4. Crystal Structures of Hybrid Organic-Inorganic Perovskites.

(A and B) show the crystal structures of $MAPbI_3$ and $FAPbI_3$, where the gray, violet, cyan, brown and pink spheres represent the Pb, I, N, C and H atoms, respectively.

Compared to the conventional Si solar cells, the most significant advantage of HOIPs lies in the material and fabrication costs. The manufacturing of Si wafers needs high temperatures (> 2000 K) and will generate high levels of chemical wastes, and thus is highly expensive. On the other hand, the production of perovskite cells is much simpler; the liquid formulation of HOIPs can be obtained by simply mixing the two halide salts AX, BX_2 in an organic solvent. And then, followed by the low temperature crystallization and deposition processes, which is usually below 400 K, the perovskite thin films can be synthesized for the solar panel usage.

1.2.3 Comparison with Inorganic Metal Halide Perovskites

The all-inorganic counterpart of organic MHPs (or HOIPs), i.e., the all-inorganic MHPs, was discovered early than HOIPs. In 1958, C. K. Møller at the Royal Veterinary and Agricultural College (Denmark) observed the perovskite structure in $CsPbX_3$ (X=Cl, Br, or I) and discovered the photoconductivity in these compounds [36]. The high-temperature crystal structures of $CsPbX_3$ are the same as ABX_3 in Figure 3, where the cation A and B are replaced by Cs and Pb, respectively.

Compared to the HOIPs, the all-inorganic MHPs are not optimized for photovoltaic applications. The best power conversion efficiencies for all-inorganic MHPs achieved by $CsPbI_3$ is ~ 16% [37, 38], which is ~ 9% smaller than the record efficiency of HOIPs. Although the electronic band edge properties are mainly determined by the inorganic network, the organic molecules still seem to play a crucial role in the charge carrier dynamics of HOIPs, through mechanisms such as the molecular rotation [14].

1.3 Two-Dimensional Metal Hybrid Perovskites

1.3.1 Crystal Structures

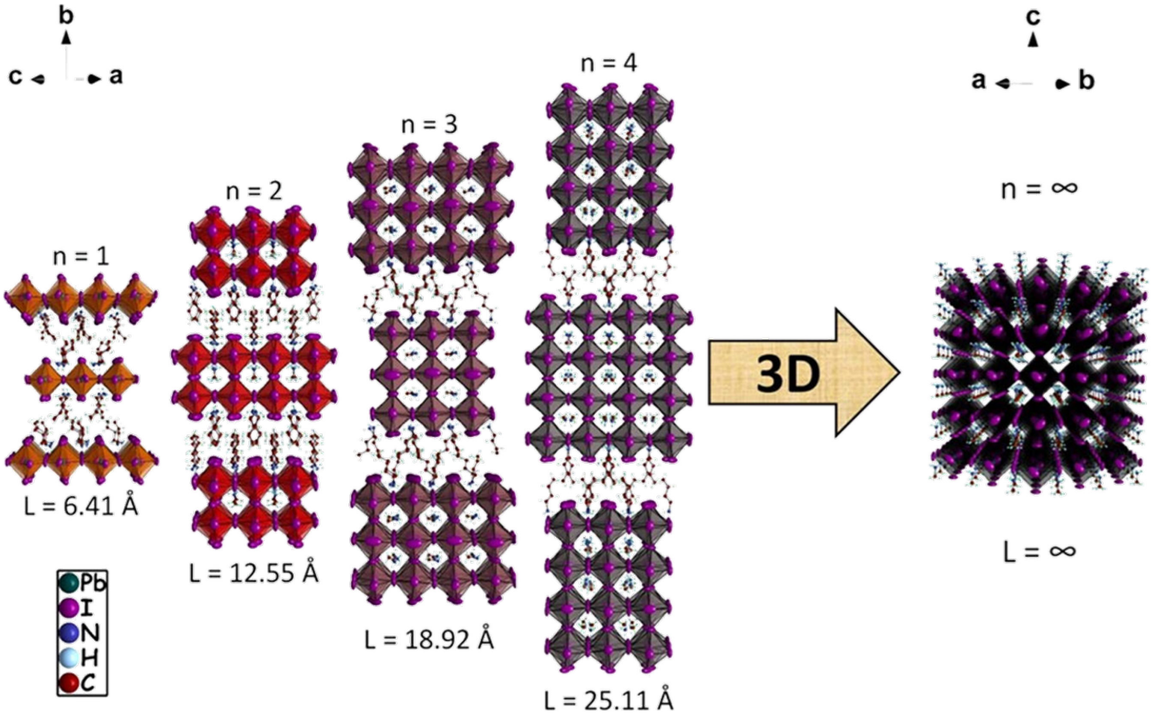

Figure 5. Crystal Structures of Two-Dimensional Hybrid Organic-Inorganic Perovskites.

The crystal structures are shown for the two-dimensional hybrid organic-inorganic perovskites (2D HOIPs), $(BA)_2(MA)_{n-1}Pb_nI_{3n+1}$*, extending from* $n = 1$ *to* ∞ *(3D* $MAPbI_3$*). The L values denote the thickness of the inorganic perovskite layers, i.e., the distance between the terminal I atoms belonging to the same inorganic layer. The figure is taken from Ref. [39].*

The hybrid organic-inorganic perovskites, e.g., $MAPbI_3$ and $FAPbI_3$, have the bulk perovskite structures, therefore, can be denoted as three-dimensional (3D) HOIPs. However, there exists another type of HOIPs, the two-dimensional (2D) HOIPs, which are formed by slicing the 3D frameworks into well-defined 2D slabs and inserting some large-sized organic molecules to segregate the adjacent slabs [39]. The large organic spacers can be ammonia or diammonia with linear, non-linear carbon chains or benzene rings. Among these, the most well-known 2D HOIP compounds are the butylammonium-methylammonium lead iodides, $(BA)_2(MA)_{n-1}Pb_nI_{3n+1}$, where the butylammonium (BA) is $CH_3(CH_2)_3NH_3$ and the methylammonium (MA) is CH_3NH_3, and n denotes the thickness of the perovskite layers [39-41]. The crystal structures of $(BA)_2(MA)_{n-1}Pb_nI_{3n+1}$ are shown in Figure 5.

The discovery of 2D HOIPs can be traced back to 1986, when Y. I. Dolzhenko, et al., reported their x-ray studies on two different 2D perovskite materials, $(CH_3(CH_2)_8NH_3)_2PbI_4$ and $(CH_3(CH_2)_9NH_3)_2CdCl_4$ [42]. However, the initially studied 2D HOIPs with low inorganic layer numbers (n) were not suitable for photovoltaic applications, instead they showed great potential for LED and laser diodes. And until this decade, in order to solve the instability issue in the 3D HOIPs, the high-layer members of 2D HOIPs were studied for solar cells.

1.3.2 Moderate Power Conversion Efficiency

The most critical factor that determines the power conversion efficiency (PCE) is the electronic bandgap, which is working through the so-called Shockley-Queisser limit [43]. The Shockley-Queisser limit predicts the theoretical maximum PCE of a single junction solar cell based on its electronic bandgap. Shown in Figure 6, under the standard solar spectrum (AM 1.5) illumination, the maximum PCE of a single junction cell is 33.7%, when the bandgap is ~ 1.34eV [44].

The Si cells have an electronic bandgap of ~ 1.1 eV, resulting in a maximum theoretical PCE of ~ 32%. However, the sample quality, surface reflection, and light blockage, will cause significant losses to the output electric power. The record efficiency of crystalline Si cells is 27.6% [2]. And for 3D HOIPs, such as $MAPbI_3$, the bandgap is 1.60 eV [39], corresponding to a maximum theoretical efficiency of ~ 30%. As we previously mentioned, by September 2019, the best efficiency of 3D HOIPs has exceeded 25 % [2].

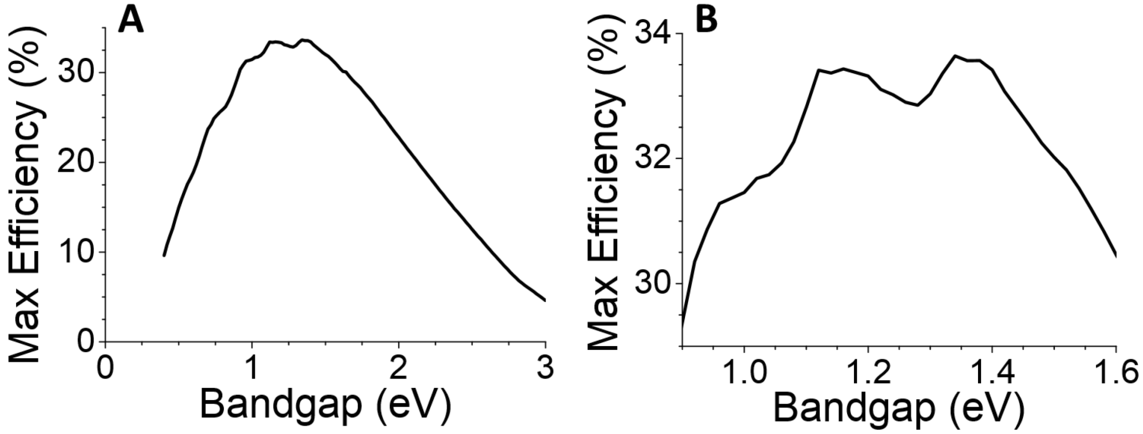

Figure 6. Shockley-Queisser Limit.

(A) The Shockley–Queisser limit for the efficiency of a single junction solar cell, without the concentration of solar radiation. The curve is wiggly because of the infrared radiation (IR) absorption bands in the atmosphere. (B) The zoomed Shockley–Queisser limit in the region of peak efficiency. The figures are extracted from Ref. [45].

However, in 2D HOIPs, the dimension of the inorganic perovskite structure, where the band-edge charge carrier sits in, is reduced. According to the quantum confinement effect, the reduced dimension will enhance the electronic bandgap. A previous photoluminescence study on the 2D HOIPs, $(BA)_2(MA)_{n-1}Pb_nI_{3n+1}$, shows a reduced bandgap from 1.60 eV for n = ∞ ($MAPbI_3$) to 1.90, 2.01, 2.12 and 2.35, when the thickness of perovskite layer is reduced to n = 4, 3, 2 and 1, respectively [39]. Therefore, for 2D

HOIPs, especially the low-n members, the electronic bandgap is much higher than the optimized solar cell bandgap at 1.34 eV, which will lead to low efficiencies.

It should be noted that the Shockley-Queisser limit only applies to the single junction cells, while those cells with multiple junctions can surpass this limit by harvesting a larger portion of the solar spectrum. Figure 1 shows that the maximum PCE of multiple junction cells has reached 46.0%. However, the high fabrication costs of the multiple junction solar cells have restricted their commercial applications.

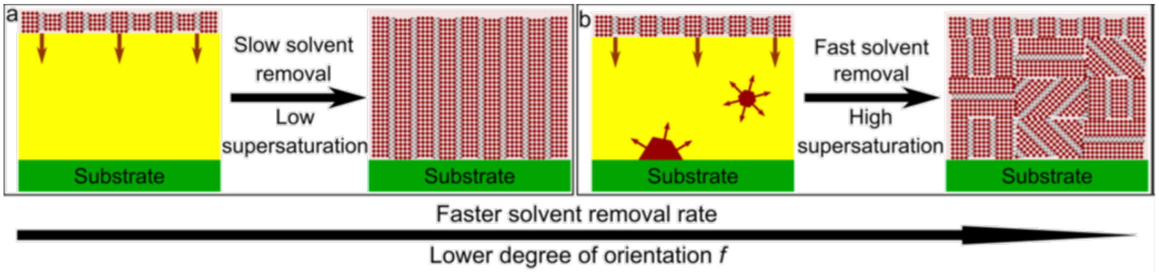

Figure 7. Crystal Orientation of 2D Perovskites.

(A) Continuous crystal growth of a vertically oriented thin film at low supersaturation, provided by a slow solvent removal rate, results in a vertically oriented thin film. (B) Additional nucleation events, due to high supersaturation with fast solvent removal rate, introduce orientation randomness. The figure is extracted from Ref. [46].

Another important factor that affects the efficiencies of the 2D HOIPs is the grain orientation in the polycrystal thin film. In 2D HOIPs, since the band-edge charge carrier can only transport along the perovskite layers, in order to allow the charge carriers to travel successfully to the electrodes, the perovskite layers in different grains must be aligned parallelly, connecting the two electrodes, as shown in Figure 7A. On the other hand, if the grain orientations are randomly distributed, as shown in Figure 7B, the charge carrier mobility and diffusion length will be significantly reduced. Fortunately, by utilizing proper synthesis methods, the crystal orientation in 2D HOIP can be controlled, and hence assisting the charge transportation [8, 46].

The first 2D HOIP-based solar cells were made by I. C. Smith, et al., at Stanford University in 2014, which used three-layered $(PEA)_2(MA)_2Pb_3I_{10}$ ($PEA=C_6H_5(CH_2)_2NH_3$) to realize a PCE of 4.73% [47]. And only 4 years later, this value was increased to 14.9%, which was reported by C. Zuo, et al., at the University of Chinese Academy of Sciences [48].

1.3.3 Moisture and Illumination Tolerances

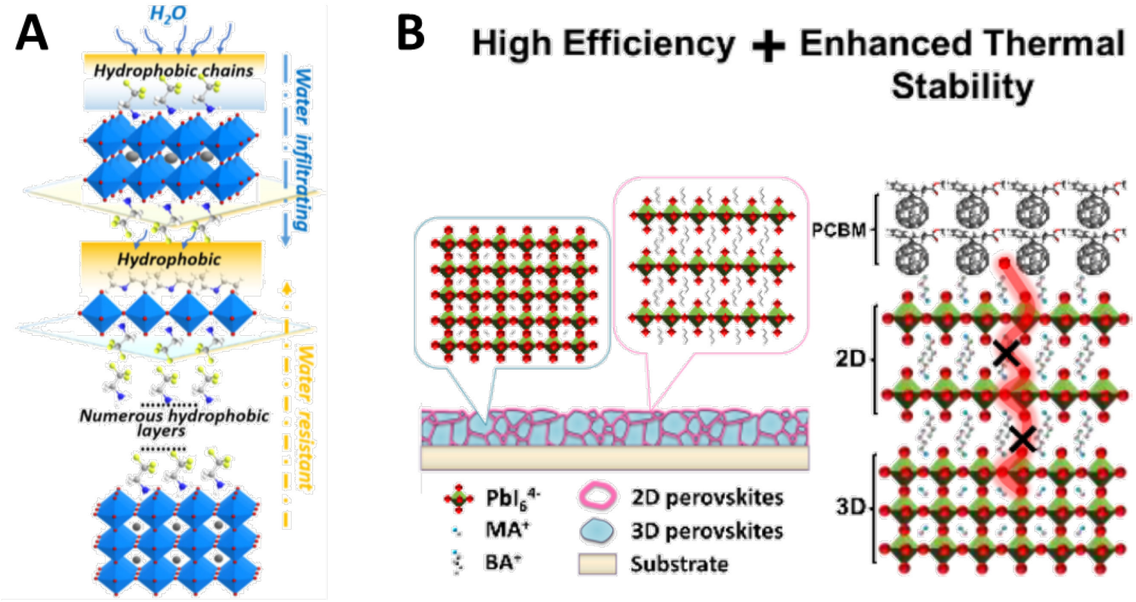

Figure 8. Mechanisms under Moisture and Illumination Tolerances.

(A) The moisture tolerance mechanism of 2D HOIPs: the hydrophobic organic spacers prevent the water infiltration along with increasing depth. (B) The heat (illumination) stability mechanism of 2D HOIPs: cation exchange becomes more difficult due to the large size of organic spacers. Figure (A) and (B) are obtained from Ref. [49] and [50], respectively.

Compared to the 3D counterparts, although the 2D HOIPs have a nearly 10% lower power conversion efficiency, their existences solve the stability problem of 3D perovskites. Even without encapsulation, 2D HOIP devices retain over 60% of their maximum efficiency for over 2250 hours under standard illumination and also exhibit a greater tolerance to 65% relative humidity than the 3D HOIPs [51]. After the device encapsulation, the 2D perovskite devices do not show any degradation under standard illumination or humidity.

The enhanced moisture tolerance is caused by the hydrophobic organic spacers inserted between the perovskite layers. These large size organic spacers, such as BA ($CH_3(CH_2)_3NH_3$) molecules, contain the hydrophobic CH_3- and -CH_2- groups, which can prevent the water from penetrating into the material [49] (see Figure 8A). On the other hand, due to the large size of the organic spacers, it is extremely difficult for them to travel through the perovskite layers [50] (see Figure 8B). Therefore, the cation escaping caused by illumination-induced thermal activation is also reduced.

1.3.4 Light Emitting Applications

Another important application of 2D HOIPs, especially for the low inorganic layer members, is the light-emission diodes (LEDs). Due to the quantum confinement effect caused by the reduced perovskite layer dimension, the exciton binding energy of 2D HOIPs is relatively large, having the order of hundred milli-electron-volts [52]. A large number of stable excitons will form when applying a voltage larger than the electronic bandgap to the metarial, and thus the bright emission light will be generated through the radiative recombination process of excitons.

The first 2D HOIP-based LED was made by M. Era, et al., at Kyushu University in 1994, which used the one-layered $(PEA)_2PbI_4$ material to produce a green color emission light with an efficiency of 0.5 $cd \cdot A^{-1}$ [32]. And in 2018, X. Yang, et al., at Chinese Academy of Sciences reported that the three-layered $(PEA)_2(FA)_2Pb_3Br_{10}$ can reach a current efficiency of 62.4 $cd \cdot A^{-1}$ and external quantum efficiency of 14.36% [53], which surpassed the best efficiency for 3D HOIPs, i.e., 42.9 $cd \cdot A^{-1}$ and 8.53% for $MAPbBr_3$ [54].

1.4 Materials to Study

The material will be discussed in this thesis is a 2-dimensional hybrid organic-inorganic perovskite (2D HOIP), i.e., the 1-layered butylammonium lead iodide, (BA)-$_2PbI_4$, The structural, rotational, vibrational, and optoelectronic properties of $(BA)_2PbI_4$ will be studied thoroughly. And a 3-dimensional methylammonium lead iodide, $MAPbI_3$, will also be discussed, especially for its vibrational properties, for the comparison purpose.

1.4.1 2D HOIP: $(BA)_2PbI_4$

The 1-layered butylammonium lead iodide, $(BA)_2PbI_4$, is a prototype of the 2D HOIP materials. The crystal structure of $(BA)_2PbI_4$ is shown in Figure 9. Compared to the higher members ($n > 1$) of 2D HOIPs, $(BA)_2(MA)_{n-1}Pb_nI_{3n+1}$ (shown in Figure 5), $(BA)_2PbI_4$ only contains one type of organic molecules, the long-chain butylammonium ($BA=CH_3(CH_2)_3NH_3$). The major purpose of this thesis to understand how the organic molecules and inorganic atoms affect the optoelectrical properties in 2D HOIPs. When multiple types of molecules are involved, then the interactions between different molecules and the charge carriers are coupled and difficult to isolate. By choosing the 1-layered $(BA)_2PbI_4$, it will be easier to study the role that the long-chain organic spacers play in the optoelectrical processes in 2D HOIPs. As for the small sized molecules located inside the inorganic framework, such as the MA molecules, their influences can be studied using the 3D HOIPs.

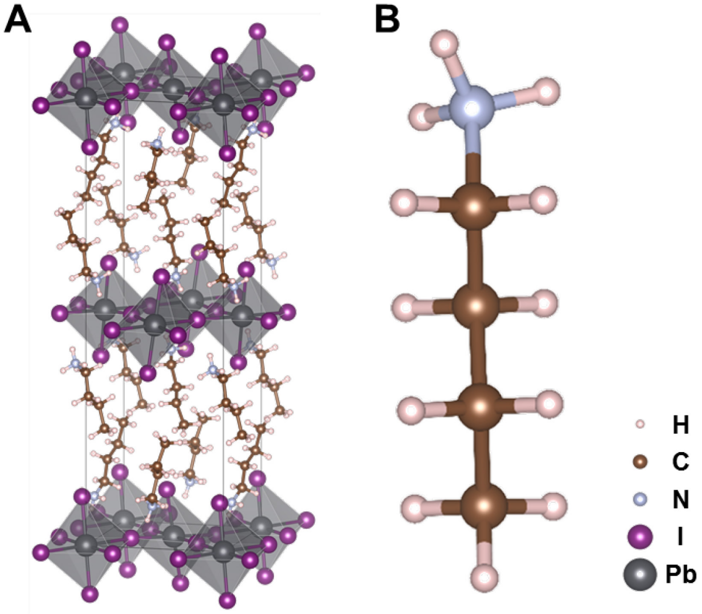

Figure 9. Crystal Structure of $(BA)_2PbI_4$.

(A) The crystal structures of $(BA)_2PbI_4$*. (B) The zoomed molecule structure of* BA^+ *cation. The gray, violet, cyan, brown and pink spheres represent the Pb, I, N, C and H atoms, respectively.*

1.4.2 3D HOIP: $MAPbI_3$

$MAPbI_3$ is a prototype and the most well studied material among all the 3D HOIPs. The single crystal $MAPbI_3$ perovskite solar cell has reached a power conversion efficiency of 21.09% [55]. The current (September 2019) record perovskite cell efficiency, 25.2%, was also achieved by materials with a similar structure as $MAPbI_3$ [2, 4, 19].

The structural, rotational and optoelectronic properties of $MAPbI_3$ have been thoroughly studied [9, 12, 14, 56-69]. $MAPbI_3$ has three structural phases, i.e., low-temperature orthorhombic phase, intermediate-temperature tetragonal phase and high-temperature cubic phase [56-58]. There are two types of rotation modes for the MA^+ cations, i.e., C_3 and C_4 jump mode, where C_3 mode exists for all three phases, C_4 mode can only survive in the cubic and tetragonal phases [58]. In $MAPbI_3$, the charge carrier lifetime shows a 3-times increase, from 5.9 ns to 24 ns, when the system undergoes a structural transition from the orthorhombic phase to the tetragonal phase [14]. However, the microscopic mechanism behind the high photovoltaic performance of $MAPbI_3$ is still under debate. Some believe that the photovoltaic performance is merely related to the inorganic framework through the inorganic-structure-related polarons and phonon liquid properties [68, 69]. Others believe that the screening effect of rotating organic molecules is the major contribution to the long-lived charge carriers [14].

In this thesis, we will show our research on the structural, rotational, vibrational, and optoelectronic properties of the 2D HOIP, $(BA)_2PbI_4$ and the vibrational properties of the 3D HOIP, $MAPbI_3$. Comparing all these results, we will be able to discuss which factor, i.e., inorganic framework or organic molecule, vibrational or rotational modes, is the more important for determining the outstanding optoelectronic performance in HOIPs.

Chapter 2.

Methods

In this thesis, a combination of various experimental and theoretical techniques is used to study the microscopic mechanisms in HOIPs. The experimental tools used in this work include elastic neutron diffraction for the crystal structure refinement and structural phase transition study, quasi-elastic neutron scattering for analyzing the rotational dynamics, inelastic neutron scattering for studying the vibrational dynamics, and photoluminescence measurements for detecting the charge carrier lifetimes. The theoretical techniques employed are the group theoretical analysis for rotational dynamics, density-functional theory (DFT) calculations for estimating the properties for specific rotational and vibrational modes.

2.1 Sample Preparation

Three different $(BA)_2PbI_4$ samples were used in this thesis: i) a non-deuterated $(BA)_2PbI_4$ (H-$(BA)_2PbI_4$=$(C_4H_9NH_3)_2PbI_4$) powder sample for the time-of-flight neutron scattering measurements (quasi-elastic and inelastic), ii) a partially deuterated $(BA)_2PbI_4$ (D-$(BA)_2PbI_4$=$(C_4D_9NH_3)_2PbI_4$) powder sample for elastic neutron diffraction experiments, and iii) a non-deuterated $(BA)_2PbI_4$ single crystal sample for the photoluminescence measurements. For 3D HOIP, a non-deuterated powder sample of $MAPbI_3$ ($CH_3NH_3PbI_3$), was used.

2.1.1 H-$(BA)_2PbI_4$ Powder Sample

The synthesis of the non-deuterated $(BA)_2PbI_4$ powder sample was adopted from the method reported by C. C. Stoumpos, et al. [39]. PbI_2 was dissolved in a mixture of HI and H_3PO_2 under heating. An equal molar of BAI was then added to the solution. After dissolution, the heating and stirring were discontinued and the solution was left to cool to the room temperature, when $(BA)_2PbI_4$ crystalized into orange plates. The crystals were then collected by suction filtration and washed 3 times with ethyl ether before vacuum-dried overnight.

2.1.2 D-$(BA)_2PbI_4$ Powder Sample

The partially deuterated $(BA)_2PbI_4$ powder sample, was synthesized using the same method as the non-deuterated $(BA)_2PbI_4$ powder sample as shown in Section 2.1.2, except that the non-deuterated BAI was replaced by partially deuterated BACl, i.e., $CD_3(CD_2)_3NH_3Cl$.

2.1.3 $(BA)_2PbI_4$ Crystal Sample

The non-deuterated $(BA)_2PbI_4$ single crystal was grown using the slow evaporation at constant temperature (SECT) solution-growth method, which is able to control the rapid nucleation effectively and reduces the multi-crystalline stacking of 2D perovskite flakes [70]. To synthesize the $(BA)_2PbI_4$ crystals, 10 mmol PbO was dissolved in 76 mmol HI and 15.5 mmol H_3PO_2 in a sample vial and kept heating. Thereafter, 10 mmol of cold BAI solution was added and the precipitate dissolved by stirring at high temperature. The solution was then left to cool slowly to room temperature to deposit the $(BA)_2PbI_4$ single crystal flakes.

2.1.4 $MAPbI_3$ Powder Sample

The non-deuterated $MAPbI_3$ powder sample was prepared using the method reported by X.-Y. Zhu, et al. [71]. 33% methylamine in ethanol, hydroiodic acid (57% by weight in water), ethanol, diethyl ether, lead iodide (PbI_2) (99.999%) were purchased from Sigma Aldrich. $MAPbI_3$ was synthesized via solution crystallization by mixing methylammonium iodide (MAI) with PbI_2 in aqueous hydrogen iodide solution and slowly evaporating the liquids via heating in ambient air.

2.2 Neutron Scattering Experiments

Neutron scattering is a powerful tool to probe the structural and dynamical properties of condensed matter materials. In this section, the theory and experimental details of the neutron scattering experiments used in this thesis will be discussed.

2.2.1 Basics of Neutron Scatterings

Neutron scattering refers to a phenomenon that energy and moving direction of the incident neutrons are changed after they interact with the atomic or molecular systems. Depending on the type of interactions, i.e., the neutron-nucleus strong interaction, or the electromagnetic interaction between the magnetic moments of a neutron and a magnetic ion, the neutron scattering can be divided into two categories, i.e., the nuclear scattering and magnetic scattering. In this thesis, only the nuclear scattering is considered since the HOIP materials we studied do not involve magnetic ions. By following the Introduction to the Theory of Thermal Neutron Scattering written G. L. Squires [72], we will show the basic theories of neutron scatterings.

The experiment geometry of neutron scattering is shown in Figure 10, where $\boldsymbol{k}_i$, E_i ($\boldsymbol{k}_f$, E_f) represent the momentum, energy of the incident (scattered) neutrons. And for neutrons, the relation between the momentum and energy is $E_i = \frac{\hbar^2 {k_i}^2}{2m}$, or $E_f = \frac{\hbar^2 {k_f}^2}{2m}$, where $m = 1.675 \times 10^{-27}$ kg is the neutron mass, $\hbar = 1.054 \times 10^{-34}$ J · s is the reduced Planck constant, $k_i = |\boldsymbol{k}_i|$, $k_f = |\boldsymbol{k}_f|$ are the momentum amplitudes.

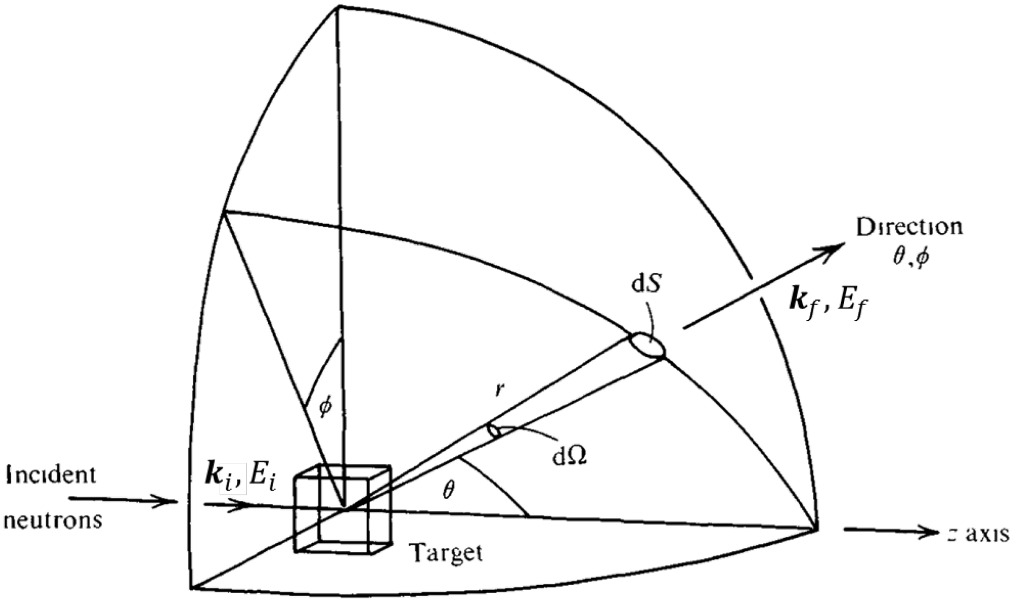

Figure 10.Experiment Geometry of Neutron Scattering.

$\boldsymbol{k}_i$, E_i ($\boldsymbol{k}_f$, E_f) represent the momentum, energy of the incident (scattered) neutrons, where $\boldsymbol{k}_i$ is along the +z direction, and $\boldsymbol{k}_f$ is along an arbitrary direction, denoted by the spherical coordinates (θ, ϕ). $d\Omega$ and dS are the differential solid angle and the differential area on the unit sphere along $\boldsymbol{k}_f$. This figure is adapted from Figure 1.2 in Ref. [72].

The quantity to be measured in the neutron scattering experiments is the number of the scattered neutrons per unit time into a small solid angle $d\Omega$ along the direction $\boldsymbol{k}_f$ with the scattered neutron energy between E_f and $E_f + dE$, i.e., the partial differential cross section, $\frac{d^2\sigma}{d\Omega dE}$. The partial differential cross section associated with the transition from the intial neutron state $\boldsymbol{k}_i$ and initial scattering system state λ_i to the final neutron state $\boldsymbol{k}_f$ and final scattering system state λ_f to can be derived from Fermi's golden rule,

$$\left(\frac{d^2\sigma}{d\Omega dE}\right)_{\boldsymbol{k}_i,\lambda_i\to\boldsymbol{k}_f,\lambda_f} = \frac{k_f}{k_i}\left(\frac{m}{2\pi\hbar^2}\right)^2 \left|\langle \boldsymbol{k}_f\lambda_f|V|\boldsymbol{k}_i\lambda_i\rangle\right|^2 \delta\left(\hbar\omega + E_i - E_f\right),$$

(Eq. 1)

where $\langle \boldsymbol{k}_f\lambda_f|V|\boldsymbol{k}_i\lambda_i\rangle$ is the inner product between the initial state $\langle \boldsymbol{k}_f\lambda_f|$, the neutron-nucleus potential function V and the final state $|\boldsymbol{k}_i\lambda_i\rangle$, $\hbar\omega = E_i - E_f$ is the energy transferred from the neutron to the scattering system.

For the nuclear scattering, the strong interaction between the neutron and nuclei is approximate to some δ-functions, i.e., $V(\boldsymbol{r}) = \frac{2\pi\hbar^2}{m}\sum_j b_j\, \delta\left(\boldsymbol{r} - \boldsymbol{R}_j\right)$, where b_j, $\boldsymbol{R}_j$ are the scattering length and position of the j-th nucleus. Therefore, after averaging over all the λ_i and summing over all the λ_f, (Eq. 1) can be transformed to

$$\frac{d^2\sigma}{d\Omega dE} = \frac{k_f}{k_i}\frac{1}{2\pi\hbar}\sum_{jj'} b_{j'}b_j \int_{-\infty}^{\infty}\langle j',j\rangle \mathrm{e}^{-i\omega t}dt,$$

(Eq. 2)

where $\langle j',j\rangle = \langle e^{-i\boldsymbol{Q}\cdot\boldsymbol{R}_{j'}(0)}e^{i\boldsymbol{Q}\cdot\boldsymbol{R}_j(t)}\rangle$ denotes the thermal average of $\langle\lambda|e^{-i\boldsymbol{Q}\cdot\boldsymbol{R}_{j'}(0)}e^{i\boldsymbol{Q}\cdot\boldsymbol{R}_j(t)}|\lambda\rangle$.

Let us first limit our discussion to the Bravais lattice case, which has only one nucleus per unit cell, then the index j and j' represent the nucleus in different unit cells. Considering that the scattering length b_j differs between different nucleus, the $b_{j'}b_j$ in (Eq. 2) should be rewritten as nuclei average $\overline{b_{j'}b_j}$, which equals to $\overline{b^2}$ if $j' = j$, or $\bar{b}^2$ if $j' \neq j$.

Based on this difference, $\frac{d^2\sigma}{d\Omega dE}$ can be separated into two terms, i.e., $\frac{d^2\sigma}{d\Omega dE} = \left(\frac{d^2\sigma}{d\Omega dE}\right)_{coh} + \left(\frac{d^2\sigma}{d\Omega dE}\right)_{inc}$,

$$\left(\frac{d^2\sigma}{d\Omega dE}\right)_{coh} = \frac{\sigma_{coh}}{4\pi}\frac{k_f}{k_i}\frac{1}{2\pi\hbar}\sum_{jj'}\int_{-\infty}^{\infty}\langle j',j\rangle \mathrm{e}^{-i\omega t}dt,$$

$$\left(\frac{d^2\sigma}{d\Omega dE}\right)_{inc} = \frac{\sigma_{inc}}{4\pi}\frac{k_f}{k_i}\frac{1}{2\pi\hbar}\sum_{j}\int_{-\infty}^{\infty}\langle j,j\rangle \mathrm{e}^{-i\omega t}dt,$$

(Eq. 3)

where $\sigma_{coh} = 4\pi\bar{b}^2$ and $\sigma_{inc} = 4\pi\left(\overline{b^2} - \bar{b}^2\right)$ are the coherent and incoherent neutron scattering cross sections. Sometimes, the neutron scattering lengths, $b_{coh} = \bar{b}$ and $b_{coh} = \sqrt{\overline{b^2} - \bar{b}^2}$, are used, instead of the cross sections, and we have $\sigma_{coh} = 4\pi {b_{coh}}^2$ and $\sigma_{inc} = 4\pi {b_{inc}}^2$. It should be noted that the term $\left(\frac{d^2\sigma}{d\Omega dE}\right)_{coh}$ contains the interference between the nuclei in different sites, i.e., $\langle j',j\rangle$, thus is referred to as the coherent scattering term, while the other term, $\left(\frac{d^2\sigma}{d\Omega dE}\right)_{inc}$, only contain the time correlation between the same nucleus, and is referred to as the incoherent scattering term.

2.2.1.1 Elastic Scattering

According to (Eq. 3), the coherent and incoherent scattering terms of a Bravais lattice can be written as

$$\left(\frac{d^2\sigma}{d\Omega dE}\right)_{coh} = \frac{\sigma_{coh}}{4\pi}\frac{k_f}{k_i}\frac{N}{2\pi\hbar}\sum_{l} e^{i\boldsymbol{Q}\cdot\boldsymbol{l}}\int_{-\infty}^{\infty}\langle e^U e^V\rangle \mathrm{e}^{-i\omega t}dt,$$

$$\left(\frac{d^2\sigma}{d\Omega dE}\right)_{inc} = \frac{\sigma_{inc}}{4\pi}\frac{k_f}{k_i}\frac{N}{2\pi\hbar}\int_{-\infty}^{\infty}\langle e^U e^V\rangle_{\boldsymbol{l}=\boldsymbol{0}} \mathrm{e}^{-i\omega t}dt,$$

(Eq. 4)

where $\boldsymbol{l}$ is the atomic position on the Bravais lattice, $U = -i\boldsymbol{Q}\cdot\boldsymbol{u}_0(0) = -i\sqrt{\frac{\hbar}{2MN}}\sum_s \frac{\boldsymbol{Q}\cdot\boldsymbol{e}_s}{\sqrt{\omega_s}}(a_s + a_s^+)$ and $V = i\boldsymbol{Q}\cdot\boldsymbol{u}_l(t) = i\sqrt{\frac{\hbar}{2MN}}\sum_s \frac{\boldsymbol{Q}\cdot\boldsymbol{e}_s}{\sqrt{\omega_s}}\left(\mathrm{e}^{+i\boldsymbol{q}\cdot\boldsymbol{l}-i\omega_s t}a_s + \mathrm{e}^{-i\boldsymbol{q}\cdot\boldsymbol{l}+i\omega_s t}a_s^+\right)$, $\boldsymbol{u}_l(t) = \boldsymbol{R}_l(t) - \boldsymbol{l}$ is the displacement of site $\boldsymbol{l}$ from its equilibrium position, M is atomic mass, N is the nuclei number in crystal, ω_s, $\boldsymbol{e}_s$, a_s^+ and a_s are the angular frequency, polarization vector, creation and annihilation operators of phonon mode s (with a wavevector $\boldsymbol{q}$ and a polarization index j), respectively.

At the thermal average, the $\langle e^U e^V\rangle$ term can be further expressed as $\langle e^U e^V\rangle = e^{\langle U^2\rangle}e^{\langle UV\rangle}$, where $e^{\langle UV\rangle} = 1 + \langle UV\rangle + \cdots$. Keep the 1st term of $e^{\langle UV\rangle}$ and apply Fourier transforms to the coherent scattering, $\left(\frac{d^2\sigma}{d\Omega dE}\right)_{coh}$, in (Eq. 4), we will get,

$$\left(\frac{d^2\sigma}{d\Omega dE}\right)_{coh\ el} = \frac{\sigma_{coh}}{4\pi}\frac{k_f}{k_i}\frac{N}{2\pi\hbar}e^{\langle U^2\rangle}\sum_l e^{i\boldsymbol{Q}\cdot\boldsymbol{l}}\int_{-\infty}^{\infty}\mathrm{e}^{-i\omega t}dt$$

$$= \frac{\sigma_{coh}}{4\pi}N\frac{(2\pi)^3}{v_0}e^{-2W}\sum_{\boldsymbol{\tau}}\delta(\boldsymbol{Q}-\boldsymbol{\tau})\,\delta(\hbar\omega),$$

(Eq. 5)

where v_0 is the volume of the unit cell, $\boldsymbol{\tau}$ is the vectors in the reciprocal lattice. Note that the δ-function, $\delta(\hbar\omega)$, confines $\hbar\omega$ to 0, hence $\left(\frac{d^2\sigma}{d\Omega dE}\right)_{coh\ el}$ is referred to as the coherent elastic scattering. Moreover, when $\hbar\omega = E_i - E_f = 0$, we have $k_f = k_i$ the term $\frac{k_f}{k_i}$ becomes 1 and vanishes in (Eq. 5). The term $e^{-2W} = e^{\langle U^2\rangle}$ is called the Debye-Waller factor, and according to (Eq. 4), $2W = -\langle U^2\rangle = \frac{\hbar}{2MN}\sum_s\frac{(\boldsymbol{Q}\cdot\boldsymbol{e}_s)^2}{\omega_s}\langle a_s a_s^+ + a_s^+ a_s\rangle = \frac{\hbar}{2MN}\sum_s\frac{(\boldsymbol{Q}\cdot\boldsymbol{e}_s)^2}{\omega_s}\langle 2n_s + 1\rangle$, where $\langle n_s\rangle$ is the thermal averaged quantum number of s-th phonon mode and it follows the Bose-Einstein distribution, i.e., $\langle n_s \rangle = \frac{1}{e^{\beta\hbar\omega_s - 1}}$ $(\beta = \frac{1}{k_B T}$, where $k_B = 1.381 \times 10^{-23}\ \mathrm{J} \cdot \mathrm{K}^{-1}$ is the Boltzmann constant).

Similarly, the incoherent scattering term in (Eq. 3) also has an elastic component,

$$\left(\frac{d^2\sigma}{d\Omega dE}\right)_{inc\ el} = \frac{\sigma_{inc}}{4\pi} N e^{-2W}\, \delta(\hbar\omega),$$

(Eq. 6)

The elastic scattering experiments, which probe the $\frac{d^2\sigma}{d\Omega dE}$ at $\hbar\omega = 0$, measure the total elastic cross section, $\left(\frac{d^2\sigma}{d\Omega dE}\right)_{coh\ el} + \left(\frac{d^2\sigma}{d\Omega dE}\right)_{inc\ el}$, in which the coherent elastic scattering, $\left(\frac{d^2\sigma}{d\Omega dE}\right)_{coh\ el}$, gives a finite intensity at $\boldsymbol{Q} = \boldsymbol{\tau}$. And since the reciprocal lattice $\boldsymbol{\tau}$ is a Fourier transform of the real space $\boldsymbol{l}$, the elastic neutron scattering provides us an important tool to probe the crystal structures of different condensed matter samples. The incoherent term $\left(\frac{d^2\sigma}{d\Omega dE}\right)_{inc\ el}$, on the other hand, contributes to a continuum along $\boldsymbol{Q}$ and brings down the signal-to-noise ratio of the structural signal. Therefore, σ_{inc} needs to be reduced in the elastic scattering experiments.

2.2.1.2 Inelastic Phonon Scattering

Phonon is an excited quasi-particle representing a periodic, collective vibration of atoms or molecules in condensed matter materials. For a crystal with N nuclei, the total number of phonon modes is $3N$. And for the j-th mode, it has a wavevector ($\boldsymbol{q}$) dependent angular frequency $\omega_j(\boldsymbol{q})$ with the eigen-energy $\hbar\,\omega_j(\boldsymbol{q})$ and a $\boldsymbol{q}$ dependent polarization vector $\boldsymbol{e}_j(\boldsymbol{q})$, which describes how each nucleus moves in a specific phonon mode. The creation and annihilation operators of the j-th phonon mode are also $\boldsymbol{q}$ dependent, i.e.,

$a_j^+(\boldsymbol{q})$ and $a_j(\boldsymbol{q})$. And as is discussed in Section 2.2.1.1, the wavevector $\boldsymbol{q}$ and mode index j can be combined to a single index s, and thus we have ω_s, $\boldsymbol{e}_s$, a_s^+ and a_s.

The scattering between neutron and a single phonon is described by the linear term of $e^{\langle UV\rangle}$, i.e., $\langle UV\rangle$ in (Eq. 3) and (Eq. 4). Since $\langle UV\rangle = \frac{\hbar}{2MN}\sum_{ss'}\frac{(\boldsymbol{Q}\cdot\boldsymbol{e}_s)(\boldsymbol{Q}\cdot\boldsymbol{e}_{s'})}{\sqrt{\omega_s\omega_{s'}}}\langle(a_s + a_s^+)\left(\mathrm{e}^{+i\boldsymbol{q}\cdot\boldsymbol{l}-i\omega_{s'}t}a_{s'} + \mathrm{e}^{-i\boldsymbol{q}\cdot\boldsymbol{l}+i\omega_{s'}t}a_{s'}^+\right)\rangle = \frac{\hbar}{2MN}\sum_s\frac{(\boldsymbol{Q}\cdot\boldsymbol{e}_s)^2}{\omega_s}\left[\mathrm{e}^{-i\boldsymbol{q}\cdot\boldsymbol{l}+i\omega_s t}\langle a_s a_s^+\rangle + \mathrm{e}^{+i\boldsymbol{q}\cdot\boldsymbol{l}-i\omega_s t}\langle a_s^+ a_s\rangle\right] = \frac{\hbar}{2MN}\sum_s\frac{(\boldsymbol{Q}\cdot\boldsymbol{e}_s)^2}{\omega_s}\left[\mathrm{e}^{-i\boldsymbol{q}\cdot\boldsymbol{l}+i\omega_s t}\langle n_s + 1\rangle + \mathrm{e}^{+i\boldsymbol{q}\cdot\boldsymbol{l}-i\omega_s t}\langle n_s\rangle\right]$, the coherent scattering term can be expressed as

$$\left(\frac{d^2\sigma}{d\Omega dE}\right)_{coh\ 1ph} = \frac{\sigma_{coh}}{4\pi}\frac{k_f}{k_i}\frac{1}{4\pi M}e^{-2W}\sum_l e^{i\boldsymbol{Q}\cdot\boldsymbol{l}}\sum_s\frac{(\boldsymbol{Q}\cdot\boldsymbol{e}_s)^2}{\omega_s}\int_{-\infty}^{\infty}\left[\mathrm{e}^{-i\boldsymbol{q}\cdot\boldsymbol{l}+i\omega_s t}\langle n_s + 1\rangle + \mathrm{e}^{+i\boldsymbol{q}\cdot\boldsymbol{l}-i\omega_s t}\langle n_s\rangle\right]\mathrm{e}^{-i\omega t}dt = \frac{\sigma_{coh}}{4\pi}\frac{k_f}{k_i}\frac{(2\pi)^3}{v_0}\frac{1}{2M}e^{-2W}\sum_s\sum_{\boldsymbol{\tau}}\frac{(\boldsymbol{Q}\cdot\boldsymbol{e}_s)^2}{\omega_s}\langle n_s + 1\rangle\,\delta(\boldsymbol{Q} - \boldsymbol{q} - \boldsymbol{\tau})\,\delta(\omega - \omega_s) + \frac{\sigma_{coh}}{4\pi}\frac{k_f}{k_i}\frac{(2\pi)^3}{v_0}\frac{1}{2M}e^{-2W}\sum_s\sum_{\boldsymbol{\tau}}\frac{(\boldsymbol{Q}\cdot\boldsymbol{e}_s)^2}{\omega_s}\langle n_s\rangle\,\delta(\boldsymbol{Q} + \boldsymbol{q} - \boldsymbol{\tau})\,\delta(\omega + \omega_s),$$

(Eq. 7)

where the 1st and 2nd terms represent the one-phonon creation and annihilation processes, which can be labeled as $\left(\frac{d^2\sigma}{d\Omega dE}\right)_{coh+1}$ and $\left(\frac{d^2\sigma}{d\Omega dE}\right)_{coh-1}$, respectively.

Similarly, the incoherent counterpart of the one-phonon scattering can be written as $\left(\frac{d^2\sigma}{d\Omega dE}\right)_{inc\ 1ph} = \left(\frac{d^2\sigma}{d\Omega dE}\right)_{inc+1} + \left(\frac{d^2\sigma}{d\Omega dE}\right)_{inc-1}$, where

$$\left(\frac{d^2\sigma}{d\Omega dE}\right)_{inc+1} = \frac{\sigma_{inc}}{4\pi}\frac{k_f}{k_i}\frac{1}{2M}e^{-2W}\sum_s\frac{(\boldsymbol{Q}\cdot\boldsymbol{e}_s)^2}{\omega_s}\langle n_s + 1\rangle\,\delta(\omega - \omega_s),$$

$$\left(\frac{d^2\sigma}{d\Omega dE}\right)_{inc-1} = \frac{\sigma_{inc}}{4\pi}\frac{k_f}{k_i}\frac{1}{2M}e^{-2W}\sum_s\frac{(\boldsymbol{Q}\cdot\boldsymbol{e}_s)^2}{\omega_s}\langle n_s\rangle\,\delta(\omega + \omega_s).$$

(Eq. 8)

The coherent and incoherent phonon scatterings, $\left(\frac{d^2\sigma}{d\Omega dE}\right)_{coh\ 1ph}$ and $\left(\frac{d^2\sigma}{d\Omega dE}\right)_{inc\ 1ph}$, can be measured by the inelastic neutron scattering (INS), which detects the $\frac{d^2\sigma}{d\Omega dE}$ as a function of the momentum transfer $\boldsymbol{Q}$ and energy transfer $\hbar\omega$. The phonon scattering allows us to obtain information about the phonon energies and phonon dispersions, which are crucial to the understanding of atomic dynamics and interatomic interactions in the material.

2.2.1.3 Quasi-Elastic Rotational Scattering

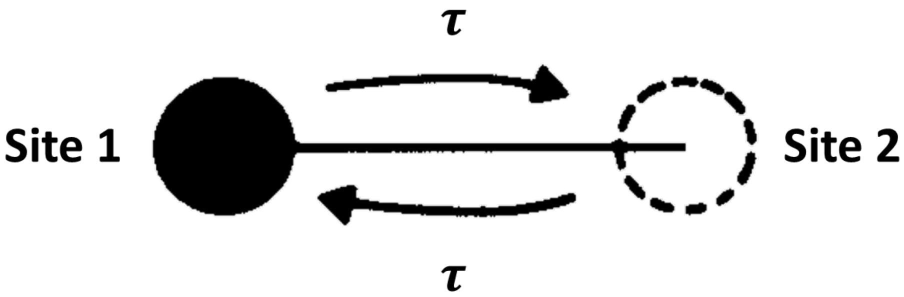

Figure 11.Jump-Diffusion Model between Two Equivalent Sites.

There exist two equivalent sites for a single particle, 1 and 2, each with the identical mean residence time, τ. At the moment, site 1 is occupied by the particle (black solid circle), and site 2 is unoccupied (dashed circle) and is available for the particle to jump into. The figure is extracted from Ref. [73].

Molecular rotation, or reorientation, usually exists in molecule-involved systems. For 3D HOIPs, e.g., $MAPbI_3$ and $FAPbI_3$, previous study in our group revealed the existence of molecular rotation of MA^+ and FA^+ cations at high temperature phases [14, 58, 74]. Generally, the rotational modes in HOIPs can be described by the jump-diffusion model [73]. In this section, we will discuss the basics of the jump-diffusion model by following the Quasielastic Neutron Scattering written by M. Bée [73].

The two equivalent site jump-diffusion model is shown in Figure 11. Assuming a particle is initially located at site 1, then in the two equivalent site jump-diffusion model, it can keep staying at site 1 with an average residence time τ, or jump from site 1 to site 2 with a probability rate $\frac{1}{\tau}$. The probability of finding the particle at site 1 or 2 at time t, denoted as $p_1(t)$ or $p_2(t)$, follows

$$p_1(t) = -\frac{1}{\tau}p_1(t) + \frac{1}{\tau}p_2(t),$$

$$p_2(t) = +\frac{1}{\tau}p_1(t) - \frac{1}{\tau}p_2(t).$$

(Eq. 9)

The solutions of (Eq. 9) with the initial condition $p_1(0) = 1$ and $p_2(0) = 0$ are

$$p_1(t) = \frac{1}{2}\left(1 + e^{-\frac{t}{2\tau}}\right),$$

$$p_2(t) = \frac{1}{2}\left(1 - e^{-\frac{t}{2\tau}}\right),$$

(Eq. 10)

while assuming site 2 to be the initial location of the particle, we will have $p_1(t) = \frac{1}{2}\left(1 - e^{-\frac{t}{2\tau}}\right)$ and $p_2(t) = \frac{1}{2}\left(1 + e^{-\frac{t}{2\tau}}\right)$.

By averaging these two scenarios, the $\langle e^U e^V \rangle$ can be rewritten as $\frac{1}{2}\left[\frac{1}{2}\left(1 + e^{-\frac{t}{2\tau}}\right) + \frac{1}{2}\left(1 - e^{-\frac{t}{2\tau}}\right)e^{+i\boldsymbol{Q}\cdot\boldsymbol{r}_{12}} + \frac{1}{2}\left(1 - e^{-\frac{t}{2\tau}}\right)e^{-i\boldsymbol{Q}\cdot\boldsymbol{r}_{12}} + \frac{1}{2}\left(1 + e^{-\frac{t}{2\tau}}\right)\right] = \frac{1}{2}[1 + \cos(\boldsymbol{Q}\cdot\boldsymbol{r}_{12})] + \frac{1}{2}[1 - \cos(\boldsymbol{Q}\cdot\boldsymbol{r}_{12})]e^{-\frac{t}{2\tau}}$, which $\boldsymbol{r}_{12}$ is displacement vector pointing from site 1 to site 2. Therefore, based on (Eq. 4), the differential scattering cross section contributed by the particle's rotation can be expressed as

$$\left(\frac{d^2\sigma}{d\Omega dE}\right)_{rot} = \frac{\sigma}{4\pi}\frac{k_f}{k_i}\frac{1}{2\pi\hbar}\int_{-\infty}^{\infty}\left[A_0(\boldsymbol{Q}) - A_1(\boldsymbol{Q})e^{-\frac{t}{2\tau}}\right]\mathrm{e}^{-i\omega t}dt = \frac{\sigma}{4\pi}\frac{k_f}{k_i}\frac{1}{\hbar}\left[A_0(\boldsymbol{Q})\,\delta(\omega) - A_1(\boldsymbol{Q})\frac{1}{\pi}\frac{\frac{1}{2\tau}}{\omega^2+\left(\frac{1}{2\tau}\right)^2}\right],$$

(Eq. 11)

where $A_0(\boldsymbol{Q}) = \frac{1}{2}[1 + \cos(\boldsymbol{Q}\cdot\boldsymbol{r}_{12})]$ and $A_1(\boldsymbol{Q}) = \frac{1}{2}[1 - \cos(\boldsymbol{Q}\cdot\boldsymbol{r}_{12})]$ are the structure factors. In the case of a powder sample, the spherical average of $\left(\frac{d^2\sigma}{d\Omega dE}\right)_{rot}$ becomes $\frac{\sigma}{4\pi}\frac{k_f}{k_i}\frac{1}{\hbar}\left[A_0(Q)\,\delta(\omega) - A_1(Q)\frac{1}{\pi}\frac{\frac{1}{2\tau}}{\omega^2+\left(\frac{1}{2\tau}\right)^2}\right]$, where $A_0(Q) = \frac{1}{2}[1 + j_0(Qr_{12})]$ and $A_0(Q) = \frac{1}{2}[1 - j_0(Qr_{12})]$. $j_0(x)$ is the 0-th order Bessel function, i.e., $j_0(x) = \frac{\sin x}{x}$.

The analysis of the two equivalent site jump-diffusion model applies for simple rotational symmetries. However, the rotational symmetries in HOIPs are more complicated, in order to study the rotational dynamics in HOIPs, group theoretical analysis must be used. The rotational motions of a molecule are restricted by its own molecule symmetry and the local crystal symmetry. The possible rotational modes can be described by the irreducible representations of the direct product $\Gamma = C \otimes M$, where C and M are the point groups of the local crystal symmetry and the molecule symmetry [58, 73]. With the Γ symmetry, the powder averaged differential scattering cross section of an atom in the molecule can be written as

$$\left(\frac{d^2\sigma}{d\Omega dE}\right)_{\Gamma} = \frac{\sigma}{4\pi}\frac{k_f}{k_i}\frac{1}{\hbar}\sum_{\gamma} A_{\gamma}(Q)\frac{1}{\pi}\frac{\tau_{\gamma}}{1+\omega^2{\tau_{\gamma}}^2},$$

(Eq. 12)

where $\sum_{\gamma}$ ... is the sum over all the irreducible representations Γ_{γ} of Γ. $A_{\gamma}(Q)$ and τ_{γ} are the structure factor and the relaxation time for the rotational mode of the irreducible representation Γ_{γ}, respectively,

$$A_{\gamma}(Q) = \frac{l_{\gamma}}{g}\sum_{\alpha}\sum_{\beta}\chi_{\gamma}^{\alpha\beta}\sum_{C_{\alpha}}\sum_{M_{\beta}} j_0\left(Q\left|R - C_{\alpha}M_{\beta}R\right|\right),$$

(Eq. 13)

$$\frac{1}{\tau_{\gamma}} = \sum_{\alpha}\frac{n_{\alpha}}{\tau_{\alpha}}\left(1 - \frac{\chi_{\gamma}^{\alpha e}}{\chi_{\gamma}^{Ee}}\right) + \sum_{\beta}\frac{n_{\beta}}{\tau_{\beta}}\left(1 - \frac{\chi_{\gamma}^{E\beta}}{\chi_{\gamma}^{Ee}}\right),$$

(Eq. 14)

where g is the order of group Γ, l_{γ} is the dimensionality of the irreducible representation Γ_{γ}, $\sum_{\alpha}$ ... and $\sum_{\beta}$ ... sum over all the classes of the point group C (α) and M (β), respectively, while $\sum_{C_{\alpha}}$ ... and $\sum_{M_{\beta}}$ ... run over all the symmetry operations that belong to the class α (C_{α}) and β (M_{β}), respectively. The character $\chi_{\gamma}^{\alpha\beta}$ is the product of $\chi_{\gamma C}^{\alpha}$ (the character of $C_{\gamma C}$) and $\chi_{\gamma M}^{\beta}$ (the character of $M_{\gamma M}$), i.e., $\chi_{\gamma}^{\alpha\beta} = \chi_{\gamma C}^{\alpha}\chi_{\gamma M}^{\beta}$. $j_0(\ldots)$ is the zeroth order spherical Bessel function, and $\left|R - C_{\alpha}M_{\beta}R\right|$ is the jump distance between the initial position R and final position $C_{\alpha}M_{\beta}R$. n_{α} and n_{β} are the number of symmetry operations of the class α and β, respectively, while τ_{α} and τ_{β} are the corresponding relaxation times. E and e represent the identity operations in group C and M, respectively [58].

In HOIPs, the molecule rotations are usually incoherent, i.e., no correlation between two different molecules. And due to the extremely large incoherent scattering length and cross section of the H atom (see Table 1 for details), the total differential scattering cross section caused by the molecular rotation can be calculated by summing the $\left(\frac{d^2\sigma}{d\Omega dE}\right)_{\Gamma}$ in (Eq. 12) over all the H atoms in the system. During the calculation, the neutron cross section σ

in (Eq. 11) and (Eq. 12) can be replaced by the incoherent cross section of H, $\sigma_{inc}^{H} = 4\pi(b_{inc}^{H})^2$.

2.2.1.4 Non-Bravais Lattice

The discussion on elastic and inelastic scatterings are based on the Bravais lattice scenario. For a Non-Bravais lattice, i.e., more than one nucleus in one unit cell, the coherent elastic scattering (Eq. 5), incoherent elastic scattering (Eq. 6), coherent one-phonon scattering (Eq. 7) and incoherent one-phonon scattering (Eq. 8) can be expressed as [72]

$$\left(\frac{d^2\sigma}{d\Omega dE}\right)_{coh\ el} = N\frac{(2\pi)^3}{v_0}\sum_{\boldsymbol{\tau}}\left|\sum_d b_{coh,d}e^{-W_d}e^{i\boldsymbol{Q}\cdot\boldsymbol{d}}\right|^2\delta(\boldsymbol{Q}-\boldsymbol{\tau})\,\delta(\hbar\omega),$$

(Eq. 15)

$$\left(\frac{d^2\sigma}{d\Omega dE}\right)_{inc\ el} = N\sum_d b_{inc,d}^2 e^{-2W_d}\,\delta(\hbar\omega),$$

(Eq. 16)

$$\left(\frac{d^2\sigma}{d\Omega dE}\right)_{coh\pm1} = \frac{k_f}{k_i}\frac{(2\pi)^3\hbar}{2v_0}\sum_s\sum_{\boldsymbol{\tau}}\frac{1}{\omega_s}\left|\sum_d\frac{b_{coh,d}}{\sqrt{M_d}}e^{-W_d}e^{i\boldsymbol{Q}\cdot\boldsymbol{d}}(\boldsymbol{Q}\cdot\boldsymbol{e}_{ds})\right|^2\langle n_s+\frac{1}{2}\pm\frac{1}{2}\rangle\,\delta(\boldsymbol{Q}\mp\boldsymbol{q}-\boldsymbol{\tau})\,\delta(\hbar\omega\mp\hbar\omega_s),$$

(Eq. 17)

$$\left(\frac{d^2\sigma}{d\Omega dE}\right)_{inc\pm1} = \frac{k_f}{k_i}\frac{\hbar}{2}\sum_s\frac{1}{\omega_s}\sum_d\frac{b_{inc,d}^2}{M_d}e^{-2W_d}|\boldsymbol{Q}\cdot\boldsymbol{e}_{ds}|^2\langle n_s+\frac{1}{2}\pm\frac{1}{2}\rangle\,\delta(\hbar\omega\mp\hbar\omega_s),$$

(Eq. 18)

where N is the unit cell number in the crystal, $\boldsymbol{d}$, M_d, $b_{coh,d}$ and $b_{inc,d}$ are the equilibrium position, mass, coherent and incoherent scattering length of nucleus d, $\boldsymbol{e}_{ds}$ is the polarization vector of nucleus d associated with phonon mode s, e^{-2W_d} is the Debye-Waller factor of nucleus d,

$$2W_d = \frac{\hbar}{2M_dN}\sum_s \frac{|\boldsymbol{Q}\cdot\boldsymbol{e}_{ds}|^2}{\omega_s}\langle 2n_s + 1\rangle.$$

(Eq. 19)

The reason that we use the neutron scattering, instead of other techniques, such as x-ray scattering, is mainly that neutron scattering is more sensitive to the organic atoms in HOIPs since the neutron scattering lengths for light organic atoms are much larger compared to x-ray. See Table 1 for details.

Table 1. Masses and Neutron Scattering Lengths of the Atoms in HOIPs.

atom	Pb	I	N	C	H	D
m (u)	207.200	126.904	14.007	12.011	1.008	2.014
b_{coh} (fm)	9.405	5.28	9.36	6.6460	-3.7390	6.671
b_{inc} (fm)	0.031	1.58	1.99	-0.0057	25.2708	4.04

The masses, m*, (in the unit of atomic mass unit, u), coherent and incoherent neutron scattering lengths,* b_{coh} *and* b_{inc} *(in the unit of fm) are listed for the atoms in the HOIPs, Pb, I, N, C, H (and its isotope, D). The neutron scattering length data are extracted from Ref. [75].*

2.2.2 Neutron Scattering Instruments

In the neutron scattering facilities, several different types of neutron scattering instruments are designed for different measurements. In this section, three types of instruments used in this thesis will be briefly discussed: i) the triple-axis spectrometers for elastic neutron scattering measurements, ii) the neutron powder diffractometer for elastic neutron scattering measurements, iii) the time of flight spectrometer for quasi-elastic and inelastic neutron scattering measurements.

2.2.2.1 Triple-Axis Spectrometer

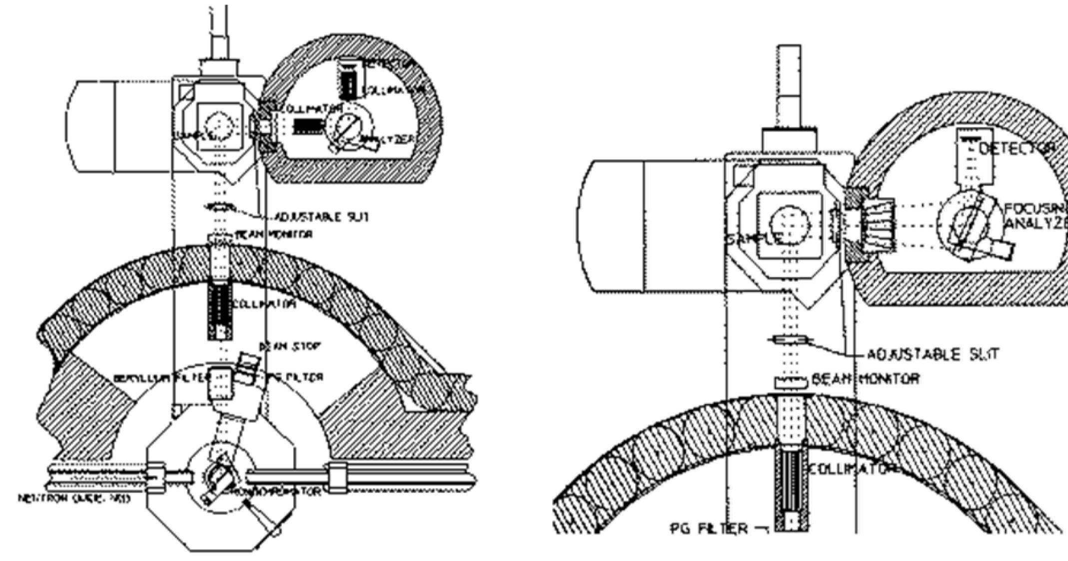

STANDARD TRIPLE-AXIS MODE

FOCUSING ANALYZER MODE

Figure 12.Schematic View of SPINS.

The schematic view of the Spin Polarized Inelastic Neutron (SPINS, NG-5), at the NIST Center for Neutron Research (NCNR), National Institute of Standard and Technology (NIST). Two modes are available for SPINS, i.e., the standard triple-axis mode and the focusing analyzer mode. The figure is obtained from Ref. [76].

The triple-axis spectrometer (TAS) is referred to as a neutron spectrometer which includes a monochromator axis, a sample axis, and an analyzer axis. The first monochromator axis is located next to the neutron guide, where it selects the wavelength (or energy, E_i) and direction ($\boldsymbol{k}_i$) of the incident neutrons. Then the second sample axis is placed along the incident neutron beam, and it defines the scattering angle, i.e., the angle between the incident ($\boldsymbol{k}_i$) and the diffracted ($\boldsymbol{k}_f$) beams. And the third analyzer axis, which controls the orientation of analyzer crystals, is placed after the sample axis, where it can choose the energy of the neutrons to be detected (E_f). By rotating these three axes, the TAS allows measurement of the partial differential cross section, $\frac{d^2\sigma}{d\Omega dE}$, at any energy transfer $\hbar\omega = E_i - E_f$ and momentum transfer $\boldsymbol{Q} = \boldsymbol{k}_i - \boldsymbol{k}_f$.

In this thesis, the triple-axis spectrometer we used is the Spin Polarized Inelastic Neutron Spectrometer (SPINS, NG-5) located at the National Institute of Standards and Technology Center for Neutron Research (NCNR). See Figure 12 for the instrument details. At SPINS, we performed elastic neutron scattering measurements on 3 grams of D-$(BA)_2PbI_4$ deuterated powder sample to study the temperature dependent crystal structures and phase transition for the 2D HOIP, $(BA)_2PbI_4$. As shown in Table 1, the deuterium (D) has a 5-times smaller incoherent scattering length than the hydrogen (H), so using the deuterated sample helps reduce the large incoherent scatterings from H atoms.

During the SPINS experiments, the D-$(BA)_2PbI_4$ sample was sealed into a cylindrical aluminum can with an indium ring in the dry helium (He) environment. The sample can was then mounted in a closed-cycle refrigerator (CCR), which allowed us to reach the temperature range from 10 K to 400 K. In order to access the elastic scattering ($\hbar\omega = 0$), the monochromator axis and analyzer axis were aligned to have $E_i = E_f =$ 5 meV, and the collimation configuration was open-80'-80'-open. Two beryllium (Be) filters cooled by liquid nitrogen (N_2) were placed before and after the sample to eliminate high order neutron contaminations. The measurements were performed at 28 different temperatures during both heating and cooling in the range of 13 K ~ 370 K. At each temperature, we scanned two ranges of scattering angle (A4 at the sample axis): 24 ~ 51° and 52 ~ 60°, both with a 0.2° step, to cover several nuclear Bragg peaks. The total counting time of the two scans at each temperature was 23 mins to achieve reasonable data statistics.

2.2.2.2 Neutron Powder Diffractometer

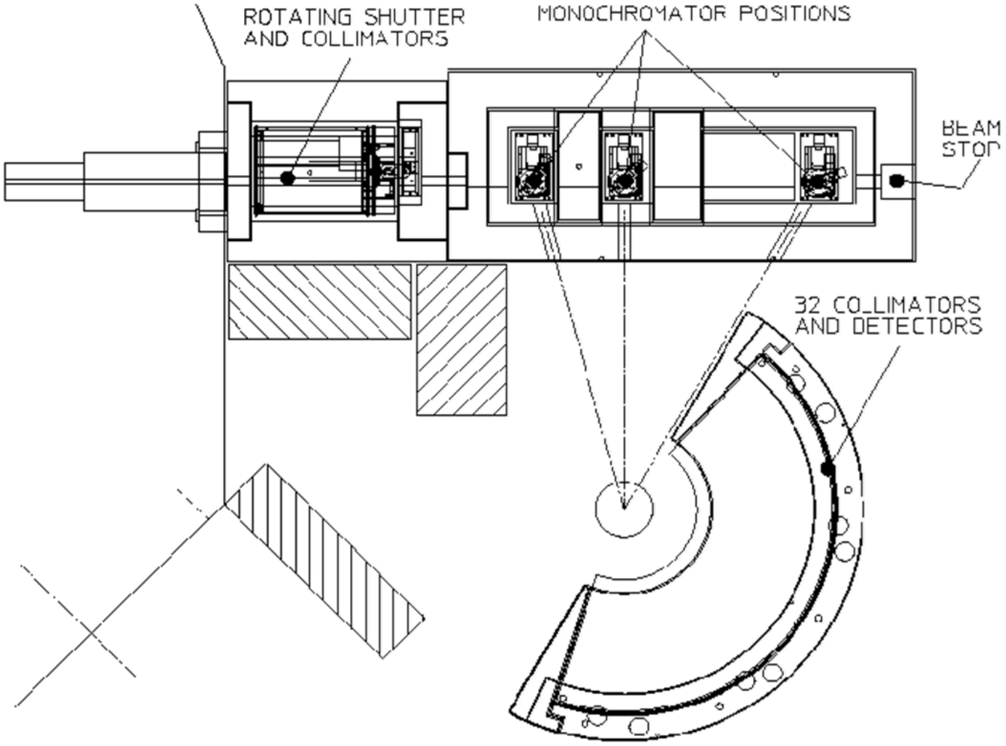

Figure 13.Schematic View of BT-1.

The schematic view of the High-Resolution Powder Diffractometer (BT-1), at the NIST Center for Neutron Research (NCNR), National Institute of Standard and Technology (NIST). The figure is obtained from Ref. [77].

Neutron powder diffractometer (NPD) is a neutron instrument specialized for the structural studies in a variety of materials. Compared to the triple-axis spectrometers, an NPD usually provides higher Q resolutions and larger Q coverages, and it can produce high-quality data for the crystallographic analysis, e.g., LeBail and Rietveld refinements. The NPDs can only measure the elastic scatterings at $\hbar\omega = 0$, so they do not have the analyzer axis, which is used to the energy of the diffracted neutrons, E_f. Theoretically, the detectors in an NPD collect neutrons with all the different E_f's, however, in practice, the detector efficiency is usually designed to be optimal at $E_f = E_i$. Therefore, the major signal obtained by the NPD is from the elastic channel.

The High-Resolution Powder Diffractometer (BT-1) at the NCNR was used for the crystal structure refinements for $(BA)_2PbI_4$. As shown in Figure 13, there are 32 He-3 detectors (separated by 5° intervals) in BT-1, which can rotate together by an angle of 13° to cover the scattering angle range of $0 < 2\theta < 167°$. At BT-1, the same D-$(BA)_2PbI_4$ powder sample was sealed into a cylindrical vanadium (V) can with an indium (In) ring in the dry helium (He) environment, then mounted into a 10 – 400 K CCR. The germanium (Ge-311) monochromator and a 60' in-pile Soller collimator were used to provide a high flux with the incident neutron energy of $E_i = 18.9$ meV. The data were then collected at three temperatures upon heating, i.e., 13 K, 200 K, and 350 K. The neutron counting time was ~ 7 hrs at each temperature.

It should be noted that in order to eliminate the dependence of the measured neutron intensity on the instrumental parameters, i.e., the $\frac{k_f}{k_i}$ factor in $\frac{d^2\sigma}{d\Omega dE}$, the intensity is usually reduced to $S(\boldsymbol{Q}, \hbar\omega) = \frac{k_i}{k_f}\frac{d^2\sigma}{d\Omega dE}$, which is known as the scattering function. Furthermore, the powder averaged $S(Q, \hbar\omega) = \frac{1}{4\pi}\int_{|\boldsymbol{Q}|=Q} S(\boldsymbol{Q}, \hbar\omega)\, d\Omega_{\boldsymbol{Q}}$, where $\Omega_{\boldsymbol{Q}}$ is the solid angle in the $\boldsymbol{Q}$ space, was calculated for all the data. Both the intensity conversion and powder average were done automatically during the data reduction process, with an open-source software, DAVE Mslice [78].

2.2.2.3 Neutron Time of Flight Spectrometer

The neutron time of flight (TOF) spectrometer is a different type of neutron spectrometers, which is used to determine the microscopic dynamics in different materials. The momentum ($\boldsymbol{Q}$) and energy ($\hbar\omega$) dependent neutron scattering spectra provide information about how the nuclei move as a function of the time and real space coordinates. Taking advantage of the time-of-flight technology and the large area detectors, the TOF spectrometers can access a large volume of the $(\boldsymbol{Q}, \hbar\omega)$ space simultaneously, which provides a much faster spectral measurement than the triple-axis spectrometers.

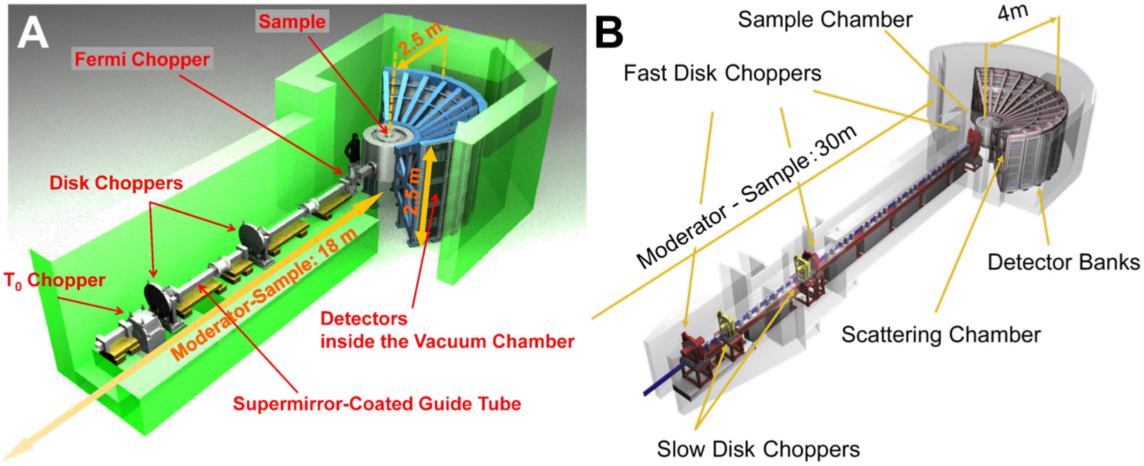

Figure 14.Schematic Views of 4SEASONS and AMATERAS.

(A and B) The schematic view of the 4D-Space Access Neutron Spectrometer (4SEASONS, BL01) [79] and the Cold-Neutron Disk-Chopper Spectrometer (AMATERAS, BL14) [80] at the Materials and Life Science Experimental Facility (MLF), Japan Proton Accelerator Research Complex (J-PARC). The figures are obtained from Ref. [81].

The schematic views of the TOF spectrometers are shown in Figure 14A, Figure 14B and Figure 15 for the the 4D-Space Access Neutron Spectrometer (4SEASONS, BL01) [79], the Cold-Neutron Disk-Chopper Spectrometer (AMATERAS, BL14) [80] at the Materials and Life Science Experimental Facility (MLF), Japan Proton Accelerator Research Complex (J-PARC), and the Wide Angular-Range Chopper Spectrometer (ARCS, BL-18) [68] located at the Spallation Neutron Source (SNS), Oak Ridge National Laboratory (ORNL), respectively. There exist several disk choppers in these TOF spectrometers, which have special openings that only allow the incident neutrons with a particular velocity to pass at some periodic time intervals. After the neutrons are diffracted by the sample, they are collected by the area detectors inside the vacuum chamber. The momentum ($\boldsymbol{k}_f$) and energy (E_f) of each scattered neutron, and hence the momentum transfer ($\boldsymbol{Q}$) and energy transfer ($\hbar\omega$), are determined by the position that neutron hits the area detector and the neutron's time of flight between the sample and detector.

The TOF spectrometers, AMATERAS, 4SEASONS and ARCS, were used to study the rotational dynamics of $(BA)_2PbI_4$, the vibration dynamics of $(BA)_2PbI_4$ and the vibration dynamics of $MAPbI_3$, respectively. At AMATERAS, the chopper frequency (f) and incident neutron energy (E_i) were set to be $f = 300$ Hz and $E_i = 3.33$ meV, which can provide an energy resolution of ~ 30 μeV. A 2.3 grams of H-$(BA)_2PbI_4$ powder sample was sealed into an annular aluminum can, in order to reduce multiple scatterings. The annular can was then mounted in a top-loading closed cycle refrigerator (TL-CCR). The measurements were done at 14 different temperatures at 10 K ~ 370 K during heating.

At 4SEASONS, in order to collect phonon spectra with proper instrument energy resolutions in different energy regions, two chopper frequency (f) settings and five different incident energies (E_i) for each setting were used: $f = 300$ Hz ($E_i = 10, 30, 53, 115, 422$ meV) and $f = 600$ Hz ($E_i = 62, 92, 148, 280, 711$ meV) [82]. A 6.5 grams of H-$(BA)_2PbI_4$ powder sample was sealed into a cylindrical aluminum can in helium gas environment and mounted in a TL-CCR. The sample was first cooled to 10 K, then measured at 23 different temperatures when heated up to 300 K. Similarly, the incident neutron energies used in ARCS were $E_i = 30, 60, 120, 250, 600$ meV. An 8 grams of powder sample of $MAPbI_3$ was sealed with helium gas in an annular aluminum can and mounted in a CCR. The sample was first cooled to 10 K, then measured at 20 different temperatures when heated up to 370 K.

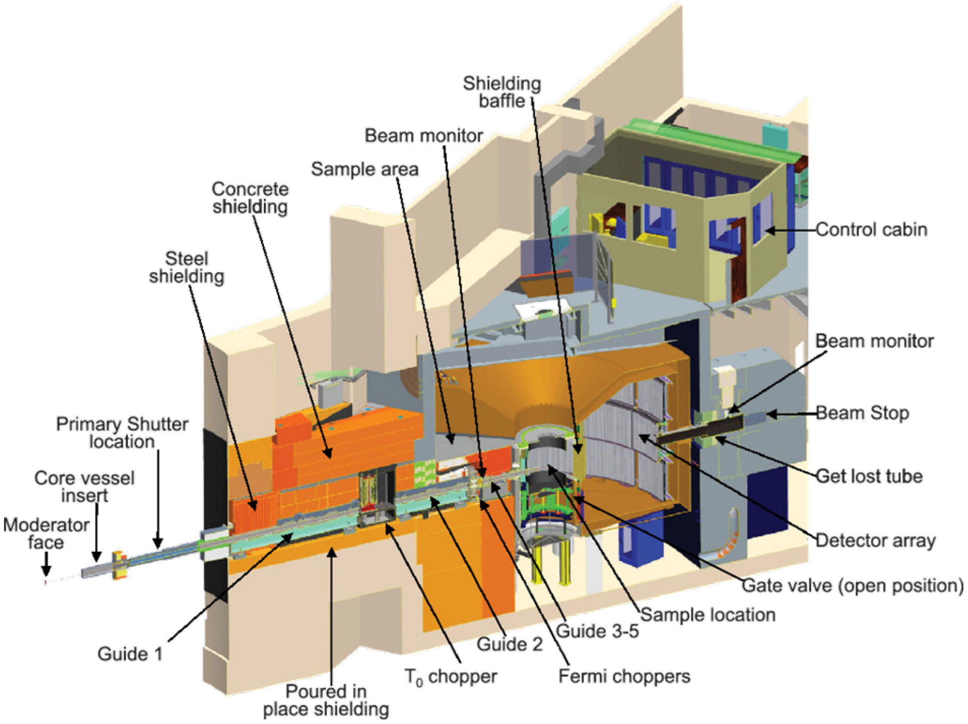

Figure 15.Schematic View of ARCS.

The schematic view of the Wide Angular-Range Chopper Spectrometer (ARCS, BL-18) [83] located at the Spallation Neutron Source (SNS), Oak Ridge National Laboratory (ORNL). The figure is obtained from Ref. [83].

Different from the triple-axis spectrometers, a TOF spectrometer collects the neutrons scattered per unit time of flight (t_f), i.e., $\frac{d^2\sigma}{d\Omega dt_f}$. Since for neutron, $dt_f \propto d\frac{1}{k_f} \propto \frac{dE}{k_f^3}$, the TOF spectrometer follows $\frac{d^2\sigma}{d\Omega dE} \propto \left(\frac{k_i}{k_f}\right)^3 \frac{d^2\sigma}{d\Omega dt_f}$. Therefore, the intensity conversion relation for a TOF instrument should be $S(\boldsymbol{Q}, \hbar\omega) = \frac{k_i}{k_f}\left(\frac{k_i}{k_f}\right)^3 \frac{d^2\sigma}{d\Omega dt_f} = \left(\frac{k_i}{k_f}\right)^4 \frac{d^2\sigma}{d\Omega dt_f}$. The data reductions, including the intensity conversion and powder average, were performed with the software packages, Utsusemi [84] and DAVE Mslice [78] for the TOF spectrometers, 4SEASON, AMATERAS and ARCS, respectively.

2.3 Photoluminescence Measurements

Photoluminescence, abbreviated as PL, is an optical measurement which is usually used to probe the electronic, opto-electronic, and electro-optical properties of various semiconducting materials. In this section, the theoretical and experimental details of the photoluminescence measurements used in this thesis will be discussed.

2.3.1 Basics of Photoluminescence

There are two steps involved in the photoluminescence process, i.e., absorption and emission [85]. The absorption happens when a semiconducting sample is exposed to light, the photons with energy larger than the sample's electronic bandgap (E_g) will be absorbed by the sample. And when the photon is absorbed, its energy will be transformed into the electronic energy of the sample, exciting an electron to the conduction band, and leaving behind a hole at the valance band. Depending on the sample properties, the electron and hole can become free carriers at the conduction band minimum (CBM) and valance band maximum (VBM) after losing the excess energies through collision with the lattice, or they can form a bound state inside the bandgap after losing more energies. Such bound state can be formed with a pair of electron and hole, which is referred to as exciton, or with an electron (a hole) and the ionic lattice, which is called polaron. The details of exciton and polaron will be discussed later in Section 4.1. The absorption step is shown as the arrow G and two following wavy arrows in Figure 16 A and B for the free carriers and bound carriers, respectively. The full (open) circles labeled by n (p) in Figure 16 A and B denote the free and bound electrons (holes) in the two scenarios.

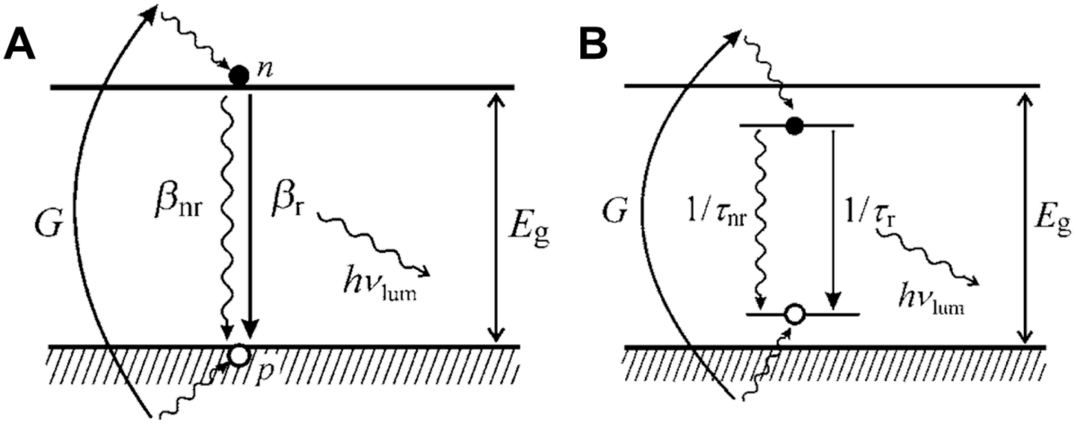

Figure 16.Photoluminescence Processes.

(A and B) show the photoluminescence processes for the free charge carriers and bound charge carriers, respectively. The figures are adapted from Ref. [85].

The free carriers and the bound carriers are metastable states, and they will recombine through the radiative and non-radiative processes, with a recombination rate of $\beta_r = \frac{1}{\tau_r}$ and $\beta_{nr} = \frac{1}{\tau_{nr}}$, where τ_r and τ_{nr} represent the corresponding lifetime for the radiative and non-radiative process, respectively [85]. The radiative and non-radiative recombinations are shown as the wavy and straight vertical arrows in Figure 16. During the radiative recombination, a photon with energy $h\gamma_{lum}$ will be emitted, which is namely the emission step in photoluminescence. As shown in Figure 16 A and B, the emitted photon energy is always equal to the bandgap, i.e., $h\gamma_{lum} = E_g$ for the free carriers. While for the bound carriers, the emitted photon energy is smaller, i.e., $h\gamma_{lum} \lesssim E_g$.

By measuring the photoluminescence (PL) spectrum as a function the photon wavelength (or energy), it will show a sharp peak centered at $h\gamma_{lum}$, which is also known as the optical bandgap. The value of the optical bandgap, as well as the shape of PL peak, can provide us some important information about electronic band structures of the semiconductors. Furthermore, by resolving the time evolution of the PL spectra with the time-resolved photoluminescence (TRPL) measurements, we can obtain information on the τ_r and τ_{nr}, and thus the lifetime of the charge carriers.

2.3.2 Photoluminescence Measurement

An example of the experiment setup for the photoluminescence (PL) measurement is shown in Figure 17. A continuous-wave or pulsed laser with the tunable wavelength (energy) is used as the excitation source. The sample is placed inside a cryostat, which can cool it down to low temperatures. The luminescence is spectrally dispersed in a double-grating monochromator and detected by a photomultiplier tube (PMT) placed behind the exit slit. The signal from the PMT is then processed by a photon counter and recorded on a computer, as a function of the wavelength (or energy). [85]

In this thesis, the PL measurements of $(BA)_2PbI_4$ were performed on a custom-built laser scanning confocal system at the Center for Condensed Matter Sciences (CCMS), National Taiwan University. The 405 nm excitation from a picosecond-pulsed laser (1 MHz repetition rate), was focused with a 5 × objective (Olympus Plan N, NA 0.15) onto a ~ 4 μm spot at a crystal sample of $(BA)_2PbI_4$. The laser power was ~ 0.1 μW on the sample. Instead of the double-grating monochromator and intensimeter photon counter shown in Figure 17, the PL signal was collected using a 200 μm fiber cable and sent to a custom-built spectrometer in our experiments. The integration time was 100 ms per pixel. The PL spectra were average over a 16 × 16 spectral mapping covering 170 μm × 170 μm, to achieve better statistics. The samples were first cooled down to 80 K in an N_2 purged temperature-controlled vacuum stage (Linkam THMS 350V), then measured at 15 different temperatures when heated up to 300 K.

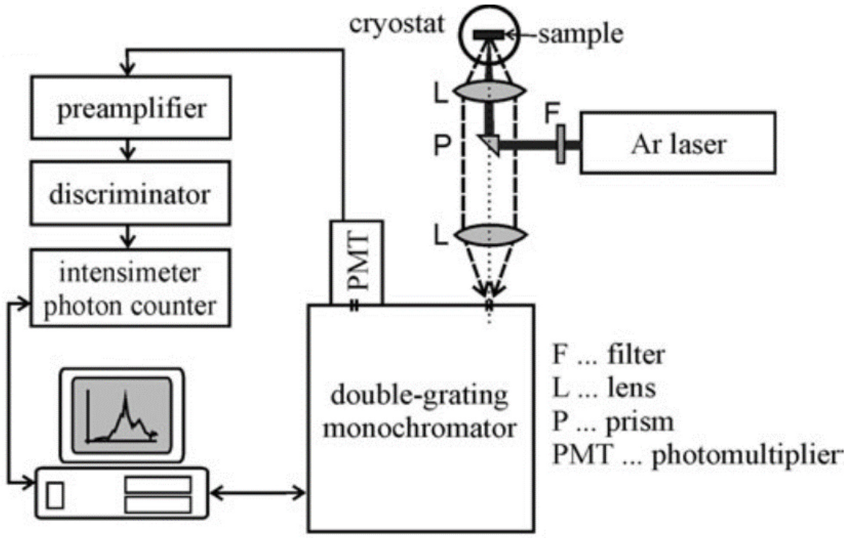

Figure 17.Experiment Setup of a Photoluminescence Measurement.

Experiment setup for detection of the photoluminescence emission spectra in a back-reflection geometry with a double-lens collection system [86]. The figure is obtained from Ref. [85].

2.3.3 Time-Resolved Photoluminescence

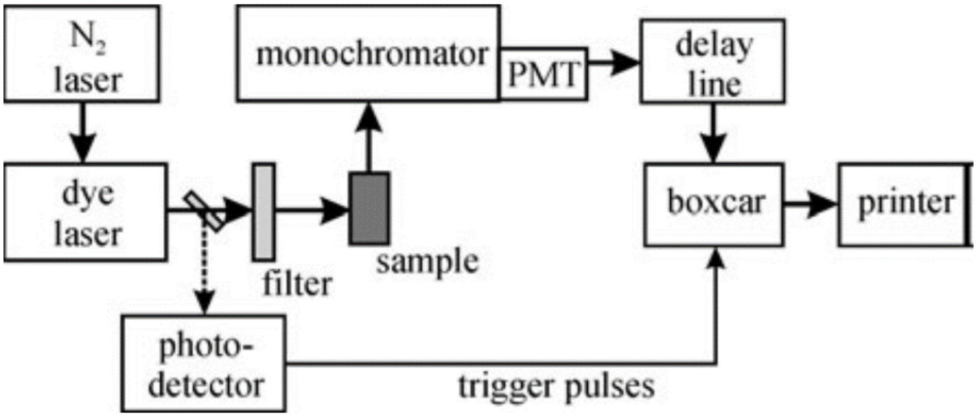

Figure 18.Experiment Setup of a Time-Resolved Photoluminescence Measurement.

Experiment setup for detection of the time-resolved photoluminescence emission spectra. The figure is obtained from Ref. [85], which was initially adapted from Ref. [87].

The experiment setup for a typical time-resolved photoluminescence (TRPL) measurement is shown in Figure 18. The photon pulses generated from a dye laser, which is pumped by a N_2 laser, is divided into two beams by a beam splitter. The transmitted pulse, which contain the majority of the dye laser's energy, excite the sample periodically. And then, the luminescence signal is detected by a PMT placed behind a monochromator, which chooses the wavelength (or energy) window for the luminescence detection. The reflected pulse, on the other hand, is applied to generate trigger pulses for a boxcar integrator with a small fraction of the excitation pulse energy. Then a boxcar integrator can construct a complete time-resolved luminescence spectrum from the PMT signal and the trigger pulses. Note that there also exists a delay line between the photomultiplier and the boxcar signal input, which serves to compensate for internal delay in the circuits. [85]

In this thesis, the TRPL spectra of $(BA)_2PbI_4$ were measured with the same laser scanning confocal system and temperature control system as discussed in Section 2.3.2, and using a PicoHarp 300 time-correlated single photon counting (TCSPC) system for photon detection. The PL signal from the crystal $(BA)_2PbI_4$ sample was first filtered by a custom-built monochromator coupled with a PMT detector (Hamamatsu H10721P-01) before sent to the TCSPC system. It should be noted that our TCSPC system doesn’t have a boxcar integrator, and by adjusting the monochromator slit, we can only detect the time-resolved PL signal at a small range of photon wavelength, with a bandwidth of 1 ~ 2 nm FWHM. The TRPL data were collected at 14 different temperatures when heated up from 80 K to 300 K. The detection (wavelength) window was chosen to be the center of the main PL peak, which is 490 ~ 521 nm at different temperatures. And the integration time used for TRPL measurements was 22 ~ 60 s. The detailed settings of TRPL measurements are shown in Table 7 at Appendix 2.

2.4 Density Functional Theory Calculations

Density functional theory, abbreviated as DFT, is a computational quantum mechanical modeling method widely used in physics, chemistry and material science to investigate the electronic structure or nuclear structure of many-body systems [88]. The name, density functional theory, comes from the fact that the calculations are based on the functionals, i.e., the functions of other functions, of the electron density distribution functions. By minimizing the total energy functional, the electron density representing the ground state of the system can be found. And all the other electronic and structural properties of the many-body system can be derived from this ground-state electron density function. The DFT calculations are entirely based on the basic physical quantities, e.g., the mass and charge of each atom, and the basic principle of quantum mechanics, e.g., Coulomb's law. So one can calculate all sorts of complicated physical quantities of the system by merely putting in the basic information, without using any advanced models or parameters. Therefore, DFT calculations are also known as first-principle, or *ab initio* calculations. The DFT calculations used in this thesis will be briefly introduced in this section.

2.4.1 Self-Consistent Calculations

The DFT calculations were performed to understand the atomic nature of the vibrational modes and the experimental INS spectra of $(BA)_2PbI_4$ and $MAPbI_3$. Our DFT calculations were based on the Vienna *ab initio* Simulation Package (VASP) [89], using the supercomputing clusters, *edison* and *cori*, at the National Energy Research Scientific Computing (NERSC) center. The projector augmented wave (PAW) method [90] is applied during the VASP calculations, and the generalized gradient approximation (GGA) in the form of Perdew–Burke–Ernzerhof (PBE) is adopted for the exchange-correlation functional [91]. The energy cutoff of the plane-wave basis set was 400 eV, and an electron momentum $(\boldsymbol{k})$-mesh with $\boldsymbol{k}$-spacing less than 0.2 $Å^{-1}$ was used.

During the self-consistent calculations, i.e., calculations for the stationary states, we used the experimentally refined low-temperature structures as the initial inputs: the low-temperature orthorhombic ($Pbca$ LT) structure at 13 K for $(BA)_2PbI_4$ with $(a, b, c) = (8.413, 8.978, 25.947)$ Å (obtained from the elastic neutron diffraction experiments and structure refinement, see Table 6 in Appendix 1 for details), and the orthorhombic ($Pnma$) structure at 4 K for $MAPbI_4$ with $(a, b, c) = (8.816, 12.598, 8.564)$ Å [58]. These initial atomic configurations were fully relaxed within a given space group symmetry, which is $Pbca$ for $(BA)_2PbI_4$, or $Pmna$ for $MAPbI_3$. We then determined the universal scaling factor (1.015 for $(BA)_2PbI_4$ and 0.990 for $MAPbI_3$) for lattice constants (a, b, c), which best fit the experimental phonon spectra.

With the relaxed ionic structures, the electronic band structures of $(BA)_2PbI_4$ and $MAPbI_3$ were calculated by non-selfconsistent calculations. The $\boldsymbol{k}$ paths of electronic band structure calculations were set to pass through the orthorhombic high symmetry points, which are $\Gamma(0,0,0) \rightarrow X(1/2\,,0,0) \rightarrow S(1/2\,,1/2\,,0) \rightarrow Y(0,1/2\,,0) \rightarrow \Gamma(0,0,0) \rightarrow Z(0,0,1/2) \rightarrow U(1/2\,,0,1/2) \rightarrow R(1/2\,,1/2\,,1/2) \rightarrow T(0,1/2\,,1/2) \rightarrow Z(0,0,1/2)$ for the $(BA)_2PbI_4$ $Pbca$ LT phase, and $\Gamma(0,0,0) \rightarrow X(1/2\,,0,0) \rightarrow U(1/2\,,0,1/2) \rightarrow Z(0,0,1/2) \rightarrow \Gamma(0,0,0) \rightarrow Y(0,1/2\,,0) \rightarrow S(1/2\,,1/2\,,0) \rightarrow R(1/2\,,1/2\,,1/2) \rightarrow T(0,1/2\,,1/2) \rightarrow Y(0,1/2\,,0)$ for the $MAPbI_3$ $Pnma$ phase.

2.4.2 Phonon Calculations

After the self-consistent calculations, we analyzed phonon eigenmodes with the finite displacement method [92, 93] as implemented in Phonopy [94], an open-source package. We employed van der Waals (vdW) density functionals, vdW-DF [95-97] and vdW-DF2 [98], to account accurately the non-local vdW corrections on top of the PBE functional. The phonon densities of states (PDOS) of $(BA)_2PbI_4$ and $MAPbI_3$ were computed using an 8×8×8 grid in the phonon momentum $\boldsymbol{q}$ space. For the comparison purpose, the Γ-point phonon modes were also calculated for isolated BA^+ and MA^+ molecules, with the same vdW-DF2 correction.

The phonon band structure of $(BA)_2PbI_4$ and $MAPbI_3$ can also be extracted from the Phonopy calculation mentioned above. The phonon band structure was calculated along the high-symmetry $\boldsymbol{q}$ path: $\Gamma(0,0,0) \rightarrow X(1/2\,,0,0) \rightarrow S(1/2\,,1/2\,,0) \rightarrow Y(0,1/2\,,0) \rightarrow \Gamma(0,0,0) \rightarrow Z(0,0,1/2) \rightarrow U(1/2\,,0,1/2) \rightarrow R(1/2\,,1/2\,,1/2) \rightarrow T(0,1/2\,,1/2) \rightarrow Z(0,0,1/2)$ for $(BA)_2PbI_4$ $Pbca$ LT phase. For $MAPbI_3$ $Pnma$ phase, the $\boldsymbol{q}$ path is: $\Gamma(0,0,0) \rightarrow X(1/2\,,0,0) \rightarrow U(1/2\,,0,1/2) \rightarrow Z(0,0,1/2) \rightarrow \Gamma(0,0,0) \rightarrow Y(0,1/2\,,0) \rightarrow S(1/2\,,1/2\,,0) \rightarrow R(1/2\,,1/2\,,1/2) \rightarrow T(0,1/2\,,1/2) \rightarrow Y(0,1/2\,,0)$.

Furthermore, the temperature dependent phonon intensities were simulated for both $(BA)_2PbI_4$ and $MAPbI_3$, using the third-part package, OCLIMAX [99]. During the calculations, the multi-phonon scatterings were considered for up to 10 phonon excitation terms. And similar phonon intensity calculations were also performed for the ionic NaCl lattice and the covalent SiO_2 lattice, by using the pre-calculated VASP files from the Phonopy examples [94].

Chapter 3.

Crystal Structures and Phase Transition

In this chapter, the temperature-dependent crystal structures of the 2D HOIP, $(BA)_2PbI_4$ will be discussed with the elastic neutron diffraction measurements and LeBail, Rietveld refinement techniques.

3.1 Structural Phase Transition of $(BA)_2PbI_4$

In order to experimentally determine the structural phase transition of $(BA)_2PbI_4$, we performed elastic neutron diffraction measurements on a partially deuterated (D-$(BA)_2PbI_4$=$(C_4D_9NH_3)_2PbI_4$) powder sample at SPINS, NCNR (see Section 2.2.2.1 for the experiment details). As shown in Figure 19A (heating) and B (cooling), there is one phase transition at 279(1) K upon heating and 257(1) K upon cooling, which is consistent with a previous differential scanning calorimetry (DSC) study on a crystal sample [40]. At the transition temperature, the positions of the Bragg peaks exhibited abrupt changes, which indicates the 1st order nature of the phase transition.

From the BT-1 data that will be described in Section 3.2, the crystal structures of both structural phases were determined to be orthorhombic with the space group of $Pbca$. With the elastic neutron diffraction data of $(BA)_2PbI_4$ shown in Figure 19A and B, we performed LeBail refinement, using the general structure analysis system (GSAS) [100, 101], to extract the temperature-dependent lattice constants, shown in Figure 19C and D. All three lattice constants (a, b, c) showed sudden shifts at the phase transition, and more prominently, the relative magnitudes of a and b switched at the transition, changing from $a < b$ in the low-temperature (low T) orthorhombic ($Pbca$ LT) phase to $a > b$ in the high-temperature (high T) orthorhombic ($Pbca$ HT) phase.

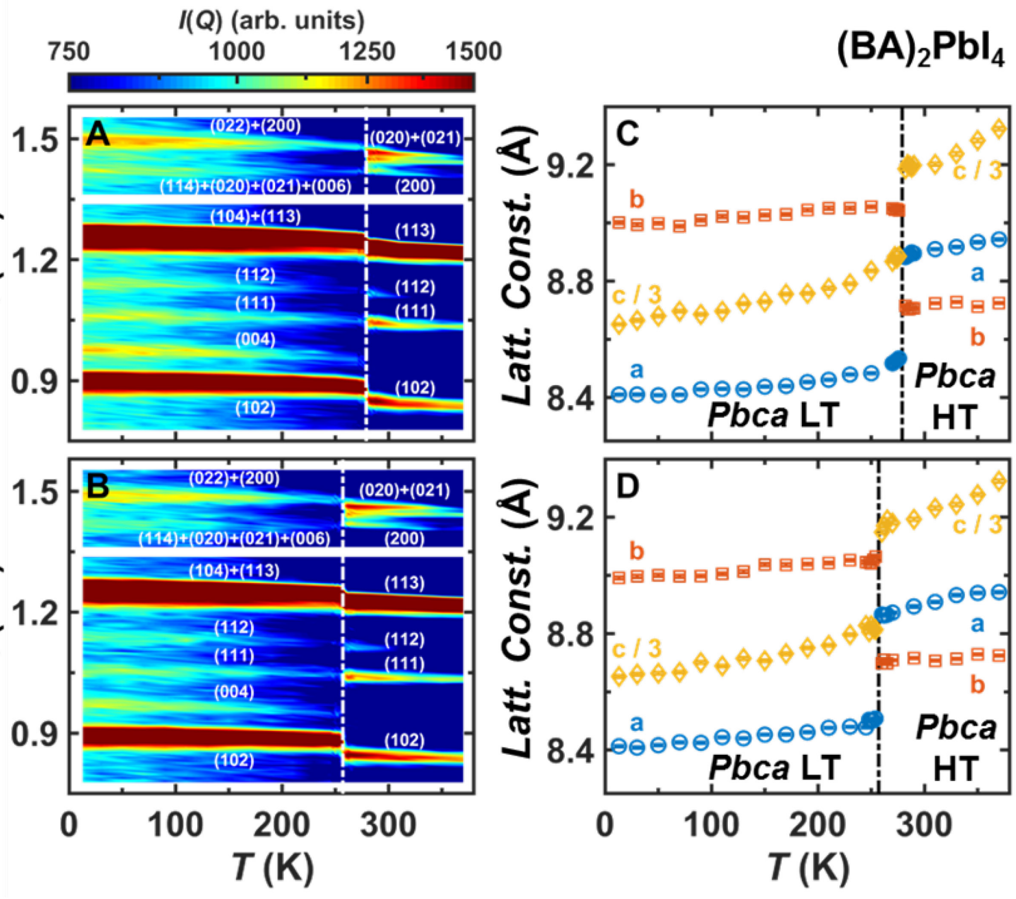

Figure 19. Temperature-Dependent Elastic Neutron Scattering Spectra of $(BA)_2PbI_4$.

(A and B) The contour maps of elastic neutron scattering intensity as a function of temperature T and momentum transfer Q, measured upon heating (A) and cooling (B). The Bragg peaks are indexed in (hkl). (C and D) The temperature-dependent lattice constants upon heating (C) and cooling (D). The blue circles, red squares and yellow diamonds represent the lattice constants a, b and c/3, respectively. The dash-dotted white and black vertical lines in (A), (B) and (C), (D), respectively, show the transition temperature between the low T orthorhombic (Pbca LT) and the high T orthorhombic (Pbca HT) phase.

3.2 Structural Refinement of Two Phases

Neutron diffraction patterns of $(BA)_2PbI_4$, with a higher Q resolution and larger Q coverage, were collected at the BT-1, NCNR (see Section 2.2.2.2 for the experiment details). The BT-1 data are shown as the black circles in Figure 20A, B and C for the diffraction patterns, $I(Q)$s, collected at 350 K for the $Pbca$ HT phase, 200 K and 13 K for the $Pbca$ LT phase, respectively. The diffraction patterns show a clear difference between the $Pbca$ HT phase (A, at 350 K) and $Pbca$ LT phase (B and C, at 200 K and 13 K), especially for those peaks at $0.8\ \text{Å}^{-1} \leq Q \leq 1.3\ \text{Å}^{-1}$, indicating the structural transition between the two phases. Another prominent difference happens at the high momenta (Qs) region, where the Bragg peak intensities are weak at 350 K, and get stronger to 200 K, and become strongest at 13 K. This feature is due to the large thermal fluctuations in the ionic crystal structure of $(BA)_2PbI_4$, which can be quantified with the Debye-Waller factors.

The crystal structures for both phases of $(BA)_2PbI_4$ were then determined by the Rietveld refinement using GSAS. The initial structures used for the Rietveld refinement were taken from a previous structure study [40] based on the x-ray measurements. Our neutron diffraction measurements, which have a higher sensitivity on the light atoms, provided more accurate organic atom positions than the x-ray results. The crystal structures were determined to be orthorhombic with a $Pbca$ space group. In a unit cell, there are 156 atoms at 20 non-equivalent crystallographic sites. In order to reduce the number of fitting parameters, the isotropic Debye-Waller factor, i.e., $e^{-2W_d} = e^{-U_{iso}[\mathrm{d}]Q^2}$, where $U_{iso}[\mathrm{d}] = \frac{\hbar}{2M_d N}\sum_s \frac{\langle 2n_s+1\rangle}{3\omega_s}$ is the isotropic atomic displacement parameter for the d-th atom (see (Eq. 19) in Section 2.2.1.4 for details). And we further confined the U_{iso}s for the 20 sites to 8 independent values: $U_{iso}[\mathrm{Pb}]$, $U_{iso}[\mathrm{I1}] = U_{iso}[\mathrm{I2}]$, $U_{iso}[\mathrm{N}]$, $U_{iso}[\mathrm{HA}] = U_{iso}[\mathrm{HB}] =$

$U_{iso}[\mathrm{HC}]$, $U_{iso}[\mathrm{C1}] = U_{iso}[\mathrm{C2}] = U_{iso}[\mathrm{C3}]$, $U_{iso}[\mathrm{D1A}] = U_{iso}[\mathrm{D1B}] = U_{iso}[\mathrm{D2A}] = U_{iso}[\mathrm{D2B}] = U_{iso}[\mathrm{D3A}] = U_{iso}[\mathrm{D3B}]$, $U_{iso}[\mathrm{C4}]$, $U_{iso}[\mathrm{D4A}] = U_{iso}[\mathrm{D4B}] = U_{iso}[\mathrm{D4C}]$.

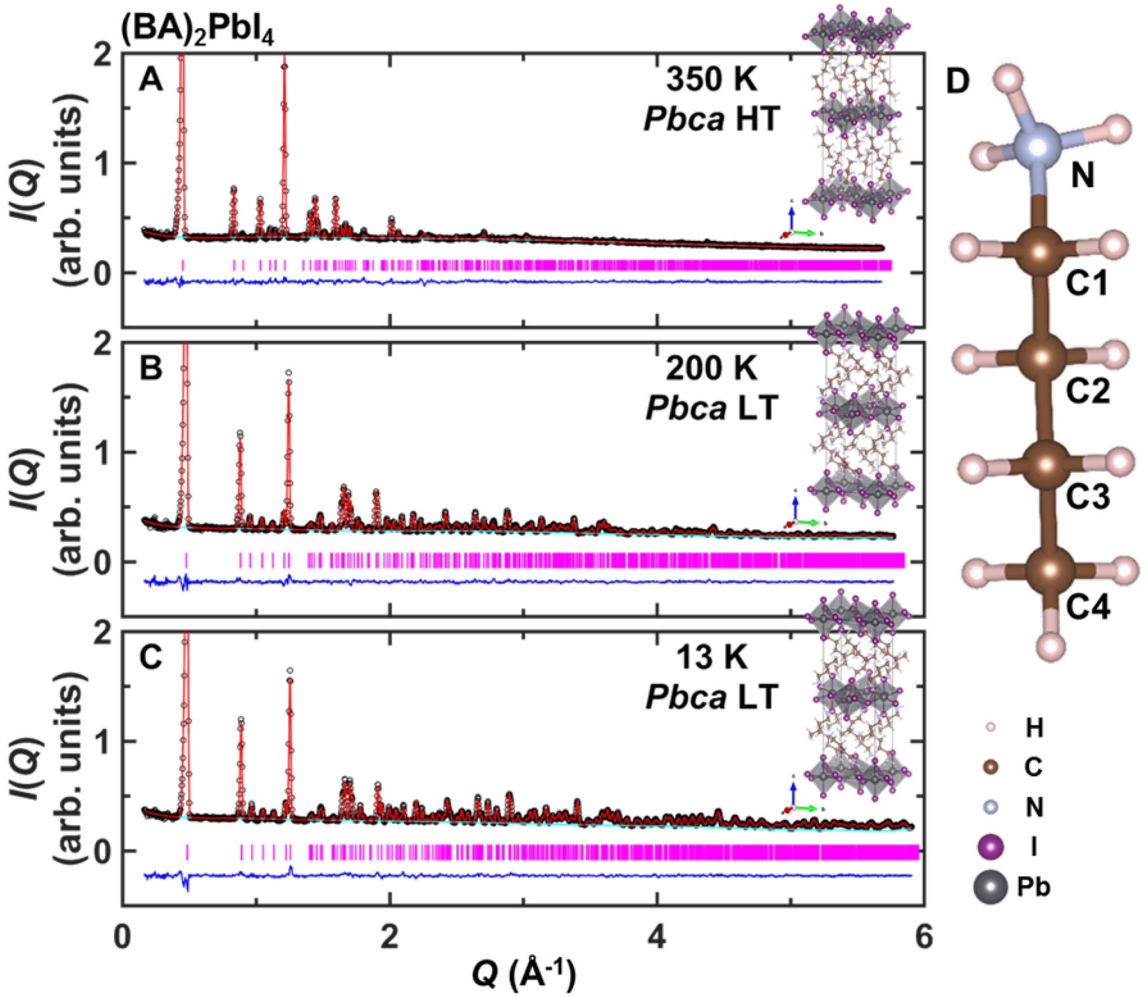

Figure 20.Neutron Diffraction Spectra and Crystal Structures of $(BA)_2PbI_4$.

In (A - C), the black dots are the neutron diffraction intensities $I(Q)$ measured at 350 K (A), at 200 K (B) both in the high T orthorhombic (Pbca HT) phase and at 13 K (C) in the low T orthorhombic (Pbca LT) phase, the red lines are the model calculation data that were obtained from the refined crystal structures shown in the insets, cyan lines are the fitted backgrounds, the blue lines are the differences between the experimental and calculational intensities, and the pink vertical marks correspond to the calculated Bragg positions. (D) The molecule structure of BA^+. In the crystal and molecular structures, the gray, violet, cyan, brown and pink spheres represent the Pb, I, N, C and H atoms, respectively.

There exists one non-equivalent BA^+ molecule, which contains 17 atoms and 51 independent refinement degrees, in the $Pbca$ unit cell of $(BA)_2PbI_4$, therefore, restrained models must be used on the BA^+ molecule to prevent the overfitting. Considering the different high-Q data qualities, different restrained molecule models should be applied at different temperatures. For 350 K ($Pbca$ HT), with the lowest data quality at high Qs, a more restrained model, i.e., the rigid body model, was used. In the rigid body model, the internal structure of the BA^+ molecule was fixed to the structure determined by Ref. [40], while three global translational and three rotational degrees of freedom were allowed for the refinement. For 200 K ($Pbca$ LT), the internal structure of the BA^+ was less constrained; the bond lengths and bond angles in the molecule were allowed to vary in a soft stereochemical restraint [102]. And for 13 K ($Pbca$ LT), since the data quality is high at the high-Q region, the internal structure of BA^+ was refined freely, without any restraint.

The refinement results are shown as red lines in Figure 20A – C that reproduce the diffraction data well, and the refined structural parameters are listed in Table 4 – Table 6 at Appendix 1. The goodness of refinement is defined as $\chi^2 = \frac{1}{N}\sum_i \frac{(y_{C,i}-y_{O,i})^2}{{\sigma_{O,i}}^2}$, where N is the number of data points, $y_{C,i}$ and $y_{O,i}$ are the calculated and experimental neutron intensities, respectively, $\sigma_{O,i}$ is the experimental error for $y_{O,i}$ [100, 103]. The χ^2 values are 1.310, 1.658 and 1.620 for 350, 200 and 13 K, respectively.

Comparing the refined crystal structures of $(BA)_2PbI_4$, there exist a significant difference between the $Pbca$ LT and $Pbca$ HT phase besides the relative magnitude of lattice constants a and b discussed in Section 3.1. The difference lies in the orientation of BA^+ molecules, i.e., the tilting angle between the BA^+ molecule axis (passing through the terminal C and N atoms) and the out-of-perovskite-layer c-axis. The BA^+ tilting angle is ~ 41° is in the $Pbca$ LT phase, which is significantly larger than the 28° angle in the $Pbca$ HT phase.

Chapter 4.

Optoelectronic Properties

In this chapter, we show the optoelectronic properties of $(BA)_2PbI_4$, especially the charge carrier dynamics, using photoluminescence measurements. Comparing with the charge carrier dynamics of the 3D HOIP, $MAPbI_3$, we will discuss the different natures of the charge carriers in these two HOIP systems.

4.1 Exciton and Polaron

The two key characteristics of HOIPs pertinent for high device performance are the extremely low charge recombination rates and charge carrier protection in the presence of defects. Relevant underlying microscopic processes include polaron formation [14, 104-110], exciton formation [52, 111-116], and electron-phonon coupling [111, 117-122]. Experimental consensus is that i) polaronic features exist in both the HOIPs and all-inorganic metal halide perovskites (MHPs), but they are more dominant in the HOIPs with organic molecules [71, 105, 123, 124], ii) excitonic features are more dominant in HOIPs with reduced dimensionality such as 2-dimensional (2D) HOIPs [52], and iii) both polaronic and excitonic characteristics can co-exist [108, 125-127].

The concept of the bound charge carriers, i.e., excitons or polarons, was briefly introduced in Section 2.3.1. In this section, we will give a more detailed discussion of the excitons and polarons in the HOIP systems.

4.1.1 Excitons in HOIPs

Exciton is a quasiparticle formed by two oppositely free charged carriers, i.e., an electron and a hole [128]. The attractive Coulomb interactions between the bound electron-hole pair contribute a negative electronic energy to the system, making the exciton a metastable state. The exciton binding energy, E_x, is the energy difference between the separated free electron-hole pair and the bound exciton. When the binding energy is large enough, so that the exciton formation time, which is proportional to $\frac{1}{E_x}$, becomes smaller than the charge carrier recombination time or dissociation time in the system, the excitons tend to survive for a long period in the system.

Depending on their dimensional and electronic properties, the excitons can be categorized into two limiting cases, i.e., i) Frenkel exciton with a small radius and large binding energy, ii) Wannier exciton with a large radius and small binding energy [129]. Frenkel exciton usually exists in materials with a small dielectric constant, e.g., alkali halide crystals or organic molecular crystals. A small dielectric constant means that electric field screening from the material is weak, therefore, the Coulomb attraction between an electron and a hole tends to be strong. Since the Coulomb potential is inversely proportional to the electron-hole distance, the size of exciton should be small. The typical binding energy of a Frenkel exciton is 0.1 ~ 1 eV, with an effective exciton radius similar to the unit cell size [129]. Wannier exciton, on the contrary, generally exists in semiconductors with a large dielectric constant, where a stronger electric field screening can effectively reduce the Coulomb attraction between the electron and hole. For a typical Wannier exciton, the binding energy is 0.01 ~ 0.1 eV, with an effective radius several times larger than the unit cell size [129].

For 3D HOIPs, the dielectric constants are large. For instance, the high-frequency dielectric constants were reported to be $\epsilon_\infty = 23.3$ and 28.7 [130] for $MAPbI_3$ and $MAPbBr_3$, respectively, twice larger than $\epsilon_\infty \approx 12$ for silicon [131]. And the exciton binding energy of $MAPbI_3$ was reported to be 16 meV, with an effective Bohr radius of 46 Å [132], much larger than the lattice dimension. Therefore, the binding energy and effective radius indicate the existence of weak Wannier excitons in 3D HOIPs. On the other hand, in the 2D HOIPs, due to the quantum confinement effect and the smaller dielectric constants, the excitons tend to be more Frenkel-like. Studies on $(BA)_2PbI_4$ showed a high-frequency dielectric constant of $2.1 \sim 4.0$ [52, 133]. Therefore, the exciton binding energy is significantly enhanced to ~ 400 meV, two orders of magnitude larger than those in the 3D HOIPs, with an exciton radius of ~ 10 Å, which is comparable to the unit cell size [51, 52, 134]s.

4.1.2 Polarons in HOIPs

Polaron is referred to as a quasiparticle which is formed by the Coulomb interaction between an excess charge (an electron or a hole) and the ionic lattice [135-139]. Similarly, the polaron binding energy, E_p, is defined as the energy difference between the separated free excess charge-lattice system and the bound polaron. Polarons with large binding energy will have shorter polaron formation time. And the polaronic states can be stable in the system when the polaron formation time is smaller than the charge carrier recombination or dissociation time.

Depending on the relation of the polaron radius and the lattice constants, the polarons can also be classified into the small polarons or large polarons [140]. A small polaron forms by the self-trapping of an excess charge into the polarized local ionic lattice. For a small polaron, the effective polaron radius, i.e., the size of the polarized lattice region, is at the same order of the lattice constants of the system, and with a formation energy of 0.1 ~ 1 eV [140]. The large polaron, also known as the Fröhlich polaron, is generated by the Fröhlich coupling, i.e., the electronic interaction between an excess charge and the polarization due to the longitudinal optical (LO) phonons. The typical formation energy for a large polaron is 0.01 ~ 0.1 eV, and the polarization region can at least extend to several unit cells [140].

In HOIPs, experimental and theoretical studies show that electrons are strongly coupled to some LO phonon modes, which mainly involve the motions of inorganic atoms, e.g., Pb-I-Pb bending and Pb-I stretching modes [111, 117, 122, 141], indicating the existence of large Fröhlich polarons. A theoretical study based on tight binding model and DFT calculations reported a polaron formation energy of 55 meV, with an effective radius of 28 Å for the 3D HOIP, $MAPbI_3$ [107]. For the 2D HOIPs, e.g., $(BA)_2PbI_4$, due to the large exciton binding energy, most of the free carriers will form small Frenkel excitons, which are electrically neutral quasi-particles. Therefore, in the absence of excess charges, the polaron formations are rare in 2D HOIPs.

The formation of large Fröhlich polarons in 3D HOIPs can protect the charge carriers from recombination or trapping to the charged impurities, defects, by efficiently screening the Coulomb interactions between the charge carriers and the other charged particles [69]. There also exist other types of screening mechanics to account for the superior optoelectronic performance, especially the prolong charge carrier lifetime, in HOIPs. X. Y. Zhu et al. argued that the anharmonic and dynamically disordered phonons in the HOIPs facilitated the formation of ferroelectric nanodomains surrounding the excess charge carriers, which can effectively screen on the charge carriers and may also result in potential barriers for the charge recombination [106]. On the other hand, the rotational dynamics of organic cations were shown to be intricately related to the charge carrier lifetime, which can be explained by the charge carrier screening from reorientation of the polarized molecules [14].

4.2 Bandgap of $(BA)_2PbI_4$

In order to study the electronic properties of the 2D HOIP, the optical bandgap of $(BA)_2PbI_4$ was determined using the photoluminescence (PL) measurements. A crystal $(BA)_2PbI_4$ sample, instead of the powder samples for neutron measurements, was used in the PL measurements to reduce the impurity PL signals caused by the defects and the surface, edge states (see Section 2.3.2 for the experiment details).

The temperature-dependent photoluminescence data of $(BA)_2PbI_4$ are shown in Figure 21. The PL peak centered at 2.55 eV gradually decreased to 2.50 eV, when the crystal sample was heated up from 80 K to 260 K. In the meanwhile, the PL peak width showed a slow broadening effect, which is caused by the electron-phonon couplings [111, 117-122]. And the $(BA)_2PbI_4$ sample exhibited a phase transition between 260 K and 270 K upon further heating, where the PL peak shifted from 2.50 eV to 2.38 eV. It should be noted that the transition temperature from PL measurements has a 10 K discrepancy with the one (279(1) K) obtained from elastic neutron diffraction measurements on a powder $(BA)_2PbI_4$ sample at SPINS (see Section 3.1), which may be related to the different sample forms of these two measurements and the precisions of different temperature control systems.

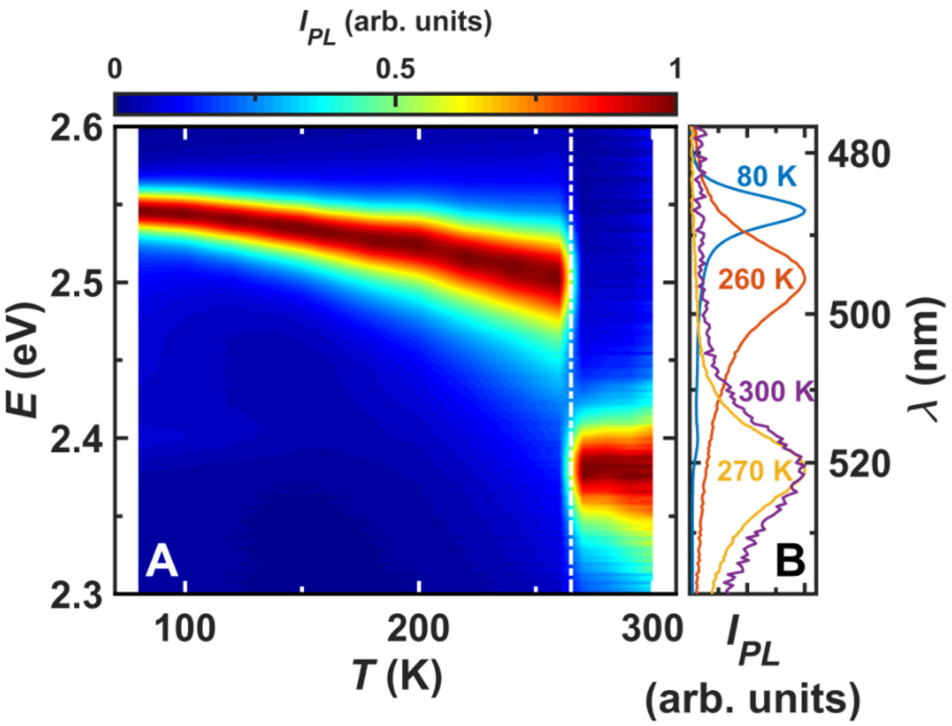

Figure 21.Temperature-Dependent Photoluminescence Spectra of $(BA)_2PbI_4$.

(A) shows the color contour map of the normalized photoluminescence intensity, $I_{PL}(T, E)$*, as a function of the temperature* T *and photon energy* E*. (B) shows the 1D plot of* $I_{PL}(E)$ *at four different temperatures: 80 K and 260 K in the* $Pbca$ *LT phase, and 270 and 300 K in the* $Pbca$ *HT phase. The vertical dash-dotted line in (A) represents the structural transition temperature upon heating.*

Compared to the 3D HOIP, $MAPbI_3$, which has an optical bandgap of ~ 1.60 eV at 300 K [14], the optical bandgap of $(BA)_2PbI_4$ is much higher, ~ 2.38 eV at 300 K. The larger optical bandgap in the 2D HOIP can be explained by the quantum confinement effect, i.e., the energies will increase when the system dimension is reduced [39].

4.3 Charge Carrier Lifetime

To probe charge carrier lifetime in 2D HOIPs, we performed time-resolved photoluminescence (TRPL) measurements on the crystal $(BA)_2PbI_4$ sample. The data we collected in the TRPL measurements are shown in Figure 22 and Figure 38 at Appendix 2. Figure 22A shows the PL intensity normalized to the initial maximum value as a function of the delay time, t, obtained for $(BA)_2PbI_4$ upon heating, and it is compared with the TRPL data obtained from a polycrystalline sample the 3D HOIP, $MAPbI_3$ (Figure 22D) that s taken from Ref. [14]. It is clear that the PL intensity of $(BA)_2PbI_4$ decays much more rapidly than that of $MAPbI_3$. For instance, at 80 K, for $(BA)_2PbI_4$ the normalized PL intensity drops to 17 % at $t = 1$ ns and to 0.12 % at $t = 10$ ns. This means that the majority of the photo-induced charge carriers recombined within 1 ns. On the other hand, for $MAPbI_3$, the PL intensity is reduced to 75 % at $t = 1$ ns and to 24 % at $t = 10$ ns. These starkly contrasting behaviors tell us that once the *majority* charge carriers are induced by the light injection they behave very differently in the two systems.

To quantify the charge carrier dynamics, we fit the normalized PL intensity with a phenomenological model in which three and two exponential functions were needed to reproduce the TRPL data for $(BA)_2PbI_4$ and $MAPbI_3$, respectively. The TRPL fittings were performed with a commercial software, FluoFit (PicoQuant) [142]. And here, we take the 3-exponent re-convolution model for $(BA)_2PbI_4$ as an example, which has the function form of

$$I_{PL}(t) = \int_{-\infty}^{t} [I_{IRF}(t' - Shift_{IRF}) - Bkgr._{IRF}] \left[A_1 e^{-\frac{t-t'}{\tau_1}} + A_2 e^{-\frac{t-t'}{\tau_2}} + A_3 e^{-\frac{t-t'}{\tau_3}}\right] dt' + Bkgr._{Dec},$$

(Eq. 15)

where $I_{PL}(t)$ is the PL intensity at a delayed time t after the laser pulse, $I_{IRF}(t)$ is the instrument response function (IRF), A_1, A_2, A_3 and τ_1, τ_2, τ_3 are the amplitude and lifetime of the three exponential components, $Bkgr._{Dec}$ and $Bkgr._{IRF}$ are the decay background and IRF background, $Shift_{IRF}$ is the time shift between IRF and decay.

The fittings were based on the TRPL data up to 150 ns, and $Bkgr._{IRF}$ was fixed to 8.6 cnts. For the 2-exponent re-convolution model of MAPbI$_3$, the function form is similar to (Eq. 15), except that the term $A_3 e^{-\frac{t-t\prime}{\tau_3}}$ is fixed to zero.

The smooth lines in Figure 22A, D are the fitting results for several different temperatures. As shown in Figure 22B, C (also see Table 8 at Appendix 2) for (BA)$_2$PbI$_4$, the dynamics of *majority* charge carriers can be characterized with two different lifetimes at all temperatures, $\tau_1 \sim 0.1 - 0.3$ ns and $\tau_2 \sim 0.4 - 1.1$ ns. The total contribution of the two components, $I_1 + I_2$, is over 90 % (see Fig. 1c), in which I_1 with the shorter lifetime is slightly larger than I_2. In addition, there exists a very weak *minority* carrier component, $I_3 < 10$ %, with a longer lifetime, $\tau_3 \sim 5 - 14$ ns. The short lifetimes of the *majority* charge carriers are consistent with the recent optical spectroscopy and magneto absorption study of the layered HOIPs in which tightly bound excitons (with a binding energy of ~ 470 meV for (BA)$_2$PbI$_4$) were observed in the 2D HOIPs [52]. For MAPbI$_3$, on the other hand, the charge carrier dynamics can be characterized with two lifetimes at all the temperatures, $\tau_1 \sim 0.7 - 5.7$ ns and $\tau_2 \sim 6 - 60$ ns, which are at least an order of magnitude longer than the two *majority* lifetimes of (BA)$_2$PbI$_4$. The contributions of the two components are evenly split with ~ 50 %. The long charge carrier lifetimes of the MAPbI$_3$ are consistent with the reported weak exciton binding energy of ~ 16 meV [143] and the formation of polarons in the 3D HOIP [14, 71, 123, 124].

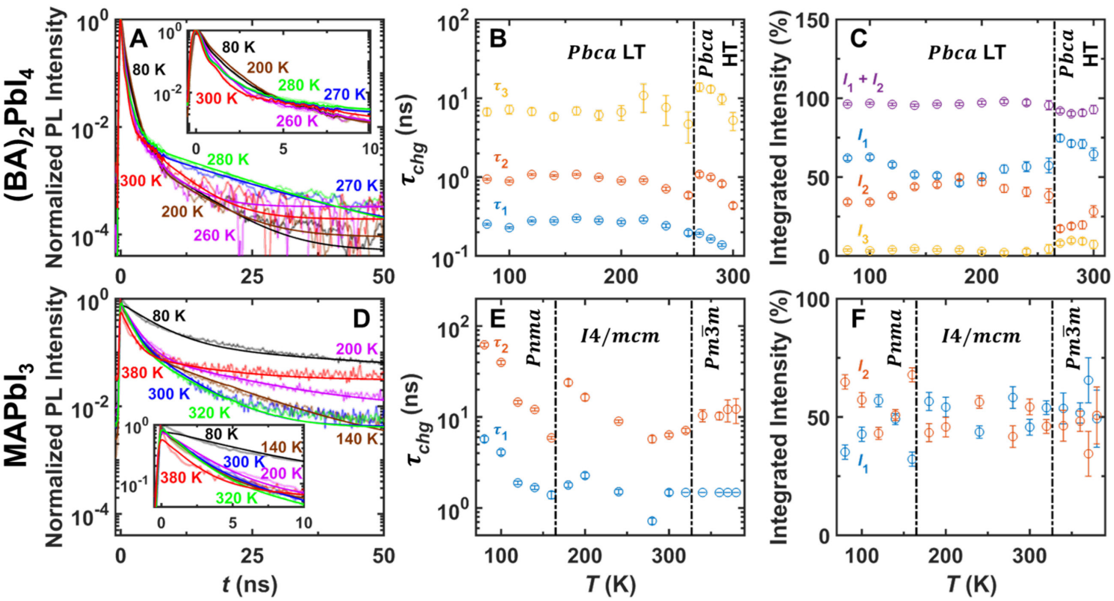

Figure 22.Charge Carrier Dynamics of (BA)$_2$PbI$_4$ and MAPbI$_3$.

(A and D) Normalized time-resolved photoluminescence (TRPL) intensity as a function of the delay time t *(*$0 \le t \le 50$ *ns) for (BA)*$_2$*PbI*$_4$ *and MAPbI*$_3$*, respectively. In (A and D), six different temperatures were plotted, spanning the two different structural phases of (BA)*$_2$*PbI*$_4$*: 80 K, 200 K, 260 K (low* T *orthorhombic phase (*$Pbca$ *LT)) and 270 K, 280 K, 300 K (high* T *orthorhombic phase (*$Pbca$ *HT)), and spanning the three different structural phases of MAPbI*$_3$*: 80 K, 140 K (orthorhombic phase (*$Pnma$*)), 200 K, 300 K (tetragonal phase (*$I4/mcm$*)) and 320 K, 380 K (cubic phase (*$Pm\bar{3}m$*)). The insets in (A and D) highlight the low delay time TRPL data up to 10 ns. (B and E) Temperature-dependent charge carrier lifetimes,* τ_{chg}*, which were extracted from a three-exponent fitting of TRPL spectra in (A) for (BA)*$_2$*PbI*$_4$*, and a two-exponent fitting of TRPL spectra in (D) for MAPbI*$_3$*. (C and F) Temperature-dependent integrated intensities for the three and two charge carrier lifetime components in (B and E), for (BA)*$_2$*PbI*$_4$ *and MAPbI*$_3$*, respectively. The TRPL data and fitting of MAPbI*$_3$ *were extracted from Ref. [14].*

The temperature dependences of τ also exhibit different behaviors in the two HOIPs. For (BA)$_2$PbI$_4$, upon heating the *majority* charge carrier lifetimes, τ_1 and τ_2, do not show any significant change over the entire temperature range including the structural phase transition at 265(5) K from the $Pbca$ LT phase to the $Pbca$ HT phase. The almost constant lifetimes are a stark contrast with the strong temperature dependences of the charge carrier lifetimes of $MAPbI_3$ that exhibit, upon heating, an initial decrease in the orthorhombic $Pnma$ phase, and a sudden jump at the 165 K transition to the tetragonal $I4/mcm$ phase, a decrease within the tetragonal $I4/mcm$ phase, and a small increase or saturation around the tetragonal to cubic $Pm\overline{3}m$ transition at 327 K. The sudden jump coincides with the activation of a rotational mode of MA^+ molecule as the system enters the tetragonal phase, which was interpreted as an evidence for the formation of polarons by screening from molecular rotations [14]. The temperature independent behavior of the charge carriers in $(BA)_2PbI_4$, on the other hand, confirms that the charge dynamics in this 2D HOIP is mainly governed by formation of excitons rather than polarons.

Chapter 5.

Rotational Dynamics

The rotational modes of 3D HOIPs, e.g., $MAPbI_3$, were previously studied in Ref. [58]. And the emergence of a specific mode, C_4 mode of the MA^+ molecule, was found to have an intimate relation to the long-lived charge carrier in $MAPbI_3$ [14]. In this chapter, the temperature dependent rotational dynamics of the 2D HOIP, $(BA)_2PbI_4$, will be discussed in details and compared with the rotational modes of $MAPbI_3$. Quasi-elastic neutron scatterings, group theoretical analysis and density-functional theory calculations were used in the study of the rotational dynamics.

5.1 Quasi-Elastic Neutron Scattering Measurements

Quasi-elastic neutron scattering (QENS) measurements were performed on a non-deuterated $(BA)_2PbI_4$ (H-$(BA)_2PbI_4$=$(C_4H_9NH_3)_2PbI_4$) powder sample at AMATERAS, J-PARC (see Section 2.2.2.3 for details). Figure 23 shows the contour maps of the QENS spectra $S(Q,\hbar\omega)$ of $(BA)_2PbI_4$, as a function of momentum transfer Q and energy transfer $\hbar\omega$, taken at 14 temperatures upon heating. For $T \lesssim 140$ K, $S(Q,\hbar\omega)$ is mostly elastic. Upon heating up to $T \approx 260$ K, $S(Q,\hbar\omega)$ gradually shows a quasi-elastic signal that is broad in Q. Upon further heating to $T \gtrsim 280$ K, the quasi-elastic signal of $S(Q,\hbar\omega)$ exhibits a dramatic enhancement. Note that the enhancement coincides with the structural transition that occurs at 279(1) K. This suggests that the rotational dynamics of $(BA)_2PbI_4$ undergoes a significant change at the phase transition. The quasi-elastic signal extends from 30 μeV to a few meV, which corresponds to a characteristic time scale of several picoseconds (ps) to hundreds of picoseconds.

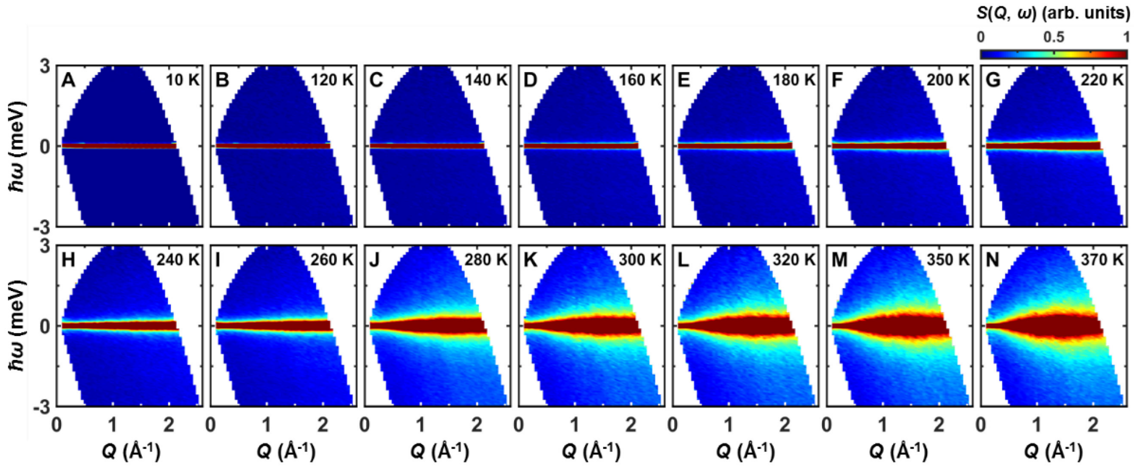

Figure 23.Quasi-Elastic Neutron Scattering (QENS) Spectra of $(BA)_2PbI_4$.

(A - N) show the contour maps of QENS intensity $S(Q,\hbar\omega)$ obtained for $(BA)_2PbI_4$ as a function of momentum transfer Q and energy transfer $\hbar\omega$, measured upon heating at several different temperatures spanning the low T orthorhombic (Pbca LT) phase (A - I) and the high T orthorhombic (Pbca HT) phase (J - N).

5.2 Jump Rotational Models in $(BA)_2PbI_4$

In both structural phases of $(BA)_2PbI_4$, the local crystal field on each BA^+ molecule, which is originated from the surrounding $[PbI_4]^{2-}$ semi-cage, has an approximate 4-fold (C_4) rotation symmetry along the c-axis, i.e., the crystal symmetry $C = C_4$. Shown with the red arrows in Figure 24, the $C = C_4$ symmetry allows for a possible 4-fold gyration motion of the whole BA^+ molecule along the C_4 axis. Possible molecule symmetries of BA^+ molecule are the 3-fold (C_3) rotation of the NH_3 and CH_3 groups located at the two ends of BA^+, and the 2-fold (C_2) rotation symmetry for the three CH_2 groups inside BA^+, i.e., the molecule symmetry $M = C_3$ or C_2 (see the blue and green arrows in Figure 24), and the total molecule symmetry of BA$^+$ can be written as $M = C_3^{NH_3} + C_3^{CH_3} + C_2^{CH_2CH_2CH_2}$.

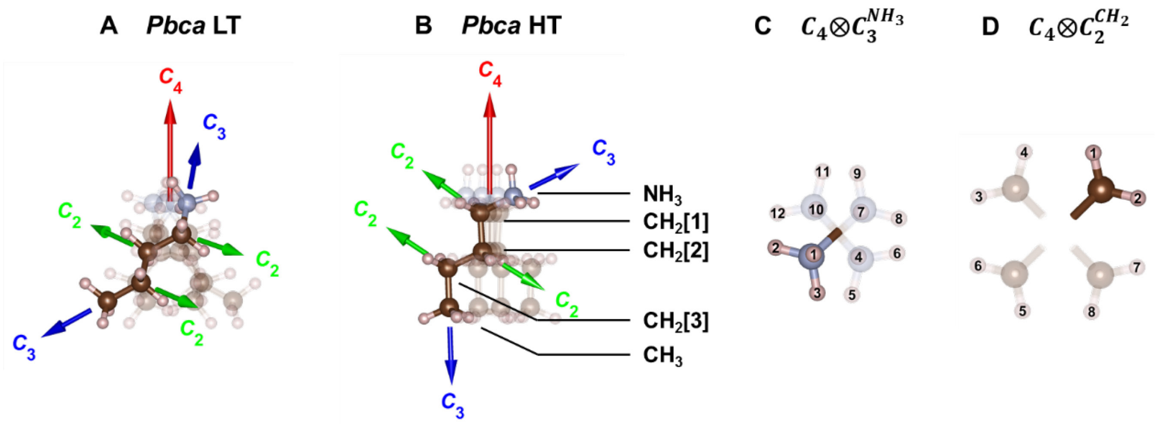

Figure 24.Local Crystal Symmetry, Molecule Symmetry and Possible Rotational Modes of (BA)$_2$PbI$_4$.

(A and B) illustrate the BA$^+$ structure in the low T orthorhombic ($Pbca$ LT) phase and the high T orthorhombic ($Pbca$ HT) phase, respectively. In A and B, the red arrows represent the local crystal symmetry $C = C_4$ about the crystallographic c-axis passing through the center of the 4 neighboring Pb atoms, due to the 4-fold gyration motion of the whole BA$^+$ molecule around the C_4 axis. The blue arrows represent the molecule symmetry $M = C_3$ of the NH$_3$ and CH$_3$ group, due to the 3-fold rotations of the three H atoms in each group. And the green arrows represent the molecule symmetry $M = C_2$ of the three CH$_2$ groups, due to the 2-fold rotations of the two H atoms in each group. (C) illustrates the 12 equivalent H sites for the $C_4 \otimes C_3$ mode of the NH$_3$ group. A similar set of 12 equivalent H sites exist for the $C_4 \otimes C_3$ mode of the CH$_3$ group. (D) illustrates the 8 equivalent H sites for the $C_4 \otimes C_2$ mode of a CH$_2$ group.

The direct product of the local crystal symmetry and molecule symmetry becomes $\Gamma = C \otimes M = C_4 \otimes \left(C_3^{NH_3} + C_3^{CH_3} + C_2^{CH_2CH_2CH_2}\right) = C_4 \otimes C_3^{NH_3} + C_4 \otimes C_3^{CH_3} + C_4 \otimes C_2^{CH_2CH_2CH_2}$, which contains two component groups, $C_4 \otimes C_3$ and $C_4 \otimes C_2$. The irreducible representations and the corresponding structure factors and relaxation times for

$C_4 \otimes C_3$ and $C_4 \otimes C_2$, $A_\gamma(Q)$ and τ_γ, can be derived using (Eq. 13) and (Eq. 14) in Section 2.2.1.3, and the character tables for the point groups C_4, C_3 and C_2 listed in Table 9 at Appendix 3. As a result, $\Gamma = C_4 \otimes C_3$ has 6 irreducible representations: $\Gamma_\gamma = \{A \otimes A, A \otimes E, B \otimes A, B \otimes E, E \otimes A, A \otimes E\}$, whose structure factors and relaxation times are listed in Table 10 at Appendix 3. $\Gamma = C_4 \otimes C_2$ also has 6 irreducible representations: $\Gamma_\gamma = \{A \otimes A, A \otimes B, B \otimes A, B \otimes B, E \otimes A, A \otimes B\}$, with the structure factors and relaxation times listed in Table 11 at Appendix 3.

5.3 Rotational Relaxation Time

Now, we can fit the data shown in Figure 23 with (Eq. 21) and all the possible modes in $\Gamma = C_4 \otimes C_3^{NH_3} + C_4 \otimes C_3^{CH_3} + C_4 \otimes C_2^{CH_2CH_2CH_2}$. Therefore, the $S_\Gamma(Q, \hbar\omega)$ in (Eq. 21) can be written as

$$S_\Gamma(Q, \hbar\omega) = S_{C_4 \otimes C_3}^{NH_3}(Q, \hbar\omega) + S_{C_4 \otimes C_3}^{CH_3}(Q, \hbar\omega) + S_{C_4 \otimes C_2}^{CH_2CH_2CH_2}(Q, \hbar\omega), \tag{Eq. 20}$$

where $S_{C_4 \otimes C_3}^{NH_3}(Q, \hbar\omega)$, $S_{C_4 \otimes C_3}^{CH_3}(Q, \hbar\omega)$, $S_{C_4 \otimes C_2}^{CH_2CH_2CH_2}(Q, \hbar\omega)$ are the scattering functions from the $C_4 \otimes C_3^{NH_3}$, $C_4 \otimes C_3^{CH_3}$ and $C_4 \otimes C_2^{CH_2CH_2CH_2}$ rotation components (details shown in Table 10 and Table 11 at Appendix 3).

To fit the rotational intensity to the QENS spectra, $S_\Gamma(Q, \hbar\omega)$ must be convoluted with the instrument resolution. The vibrational contributions are also ineligible, especially for high temperatures. The resulting fitting function for the QENS spectra, $S_{fit}(Q, \hbar\omega)$, becomes

$$S_{fit}(Q,\hbar\omega) = A_{rot}e^{-U_{iso}Q^2}\int_{-\infty}^{+\infty} S_{res}(\sigma,\gamma;\ \hbar\omega')S_{\Gamma}(Q,\hbar\omega-\hbar\omega')d(\hbar\omega') +$$

$$A_{vib}Q^2e^{-U_{iso}Q^2},$$

(Eq. 21)

where the first term is the rotational contribution and the second term is the vibrational contribution, with the scaling factors A_{rot} and A_{vib}, respectively. $S_{res}(\sigma,\gamma;\ \hbar\omega)$ is the instrument resolution, which is a Voigt function with the Gaussian and Lorentzian widths σ and γ. $e^{-U_{iso}Q^2}$ is the Debye Weller factor with an isotropic atomic displacement parameter U_{iso} of all the H atoms in the BA$^+$ molecule.

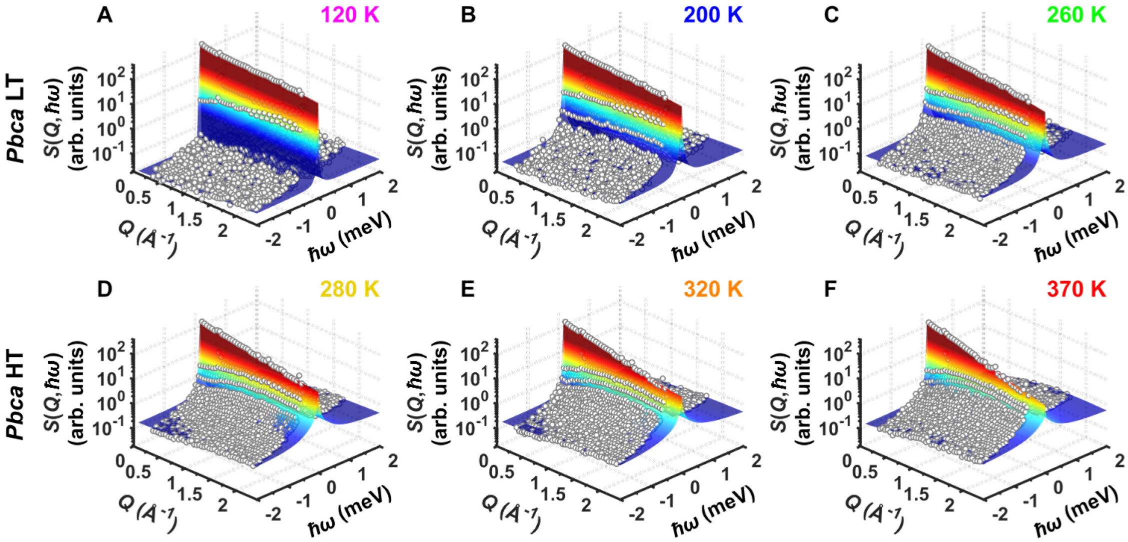

Figure 25.2D Contour Maps of QENS Spectra for (BA)$_2$PbI$_4$.

In (A - F), the experimental QENS data, $S(Q,\hbar\omega)$*, obtained at six different temperatures are shown by white circles. The color surfaces are the model calculation QENS spectra,* $S_{fit}(Q,\hbar\omega)$*, which were fitted to the experimental* $S(Q,\hbar\omega)$*. In the fitting, for the low T orthorhombic (*$Pbca$ *LT) phase (120 K (A), 200 K (B), 260 K (C)), the relaxation times for the* C_4 *and the* C_2 *modes were fixed to be infinite,* $\tau_{C_4}, \tau_{C_2} \rightarrow \infty$ *while the relaxation time for the* C_3*,* τ_{C_3}*, was fitted. For the high T orthorhombic (*$Pbca$ *HT) phase (280 K (D), 320 K (E), 370 K (F)), the relaxation time for* τ_{C_2} *was fixed to be infinite,* $\tau_{C_2} \rightarrow \infty$*, while* τ_{C_4} *and* τ_{C_3} *were fitted.*

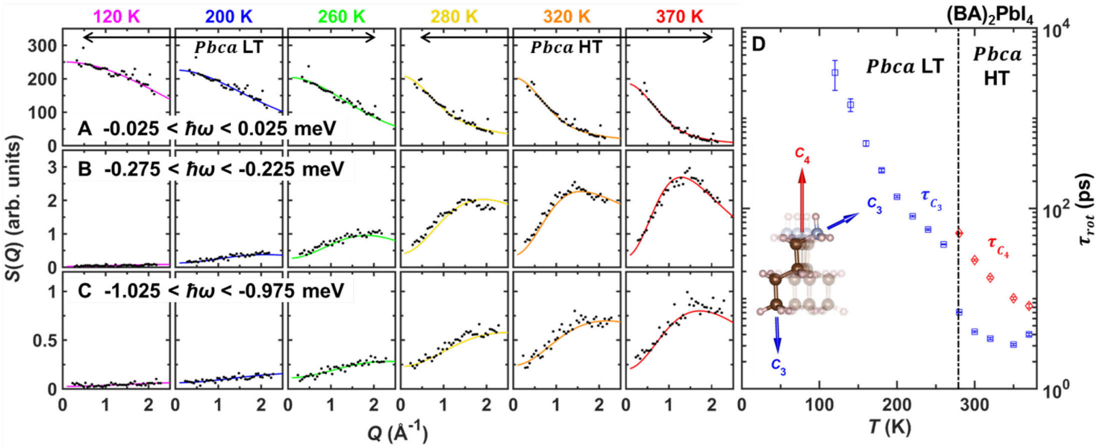

Figure 26.1D Constant-Energy Slices of QENS Spectra and Rotational Relaxation Times for (BA)$_2$PbI$_4$.

(A - C) the Q-dependences of the $\hbar\omega$-integrated QENS data, $S(Q)$, at three different energy slices, $-0.025 < \hbar\omega < 0.025\, meV$ (A), $-0.275 < \hbar\omega < -0.225\, meV$ (B), and $-1.025 < \hbar\omega < -0.975\, meV$ (C), for six selected temperatures, 120 K, 200 K, 260 K (low T orthorhombic phase ($Pbca$ LT)) and 280 K, 320 K, 370 K (high T orthorhombic phase ($Pbca$ HT)). The black dots are the experimental $S(Q)$, and the colored lines are the model calculation QENS spectra, $S_{fit}(Q)$, also shown as the contour maps in Figure 25. (D) Rotational relaxation times for the C_3 and C_4 modes, τ_{C_3} (blue squares) and τ_{C_4} (red diomands), which are extracted from the QENS fittings in A - C (the numerical data are listed in Table 2). The inset in D shows the C_3 (for NH$_3$ and CH$_3$ groups) modes and the C_4 mode (for the whole molecule) for a BA$^+$ molecule, with the blue and red arrows representing the C_3 and C_4 rotational axes, respectively.

It should be noted that, during the fitting, due to the similarity of the C_3 rotations for the NH$_3$ and CH$_3$ groups, we assumed that the relaxation times of the C_3 modes were identical: $\tau_{C_3}^{NH_3} = \tau_{C_3}^{CH_3} = \tau_{C_3}$. We applied the same assumption to the C_2 rotations for three CH$_2$ groups (CH$_2$[1], CH$_2$[2] and CH$_2$[3]): $\tau_{C_2}^{CH_2[1]} = \tau_{C_2}^{CH_2[2]} = \tau_{C_2}^{CH_2[3]} = \tau_{C_2}$. Furthermore, we also set $\frac{1}{\tau_{C_2}} = 0$ ($\tau_{C_2} \to \infty$) for both the $Pbca$ LT and $Pbca$ HT phases, and $\frac{1}{\tau_{C_4}} = 0$ ($\tau_{C_4} \to \infty$) for the *Pbca* LT phase, the justification for which will be explained later. Note that when $\frac{1}{\tau_\gamma} = 0$, the term $\frac{1}{\pi}\frac{\tau_\gamma}{1+\omega^2\tau_\gamma^2}$ in (Eq. 12)) becomes a delta function $\delta(\omega)$, i.e., it contributes to the elastic channel. The resulting fits are shown in Figure 25 and Figure 26A – C, and the fitted relaxation times, τ_{C_4}, τ_{C_3} and τ_{C_2}, are listed in Figure 26D and Table 2.

Table 2. Relaxation Times for BA^+ Jump Rotation Mode C_4, C_3 and C_2.

Phase	T (K)	τ_{C_4} (ps)	τ_{C_3} (ps)	τ_{C_2} (ps)	$\sqrt{\langle u^2 \rangle}$ (Å)
Pbca LT	120	∞	3000 (1000)	∞	0.313 (4)
	140	∞	1400 (200)	∞	0.332 (4)
	160	∞	520 (40)	∞	0.334 (4)
	180	∞	260 (10)	∞	0.320 (4)
	200	∞	135 (3)	∞	0.314 (3)
	220	∞	82 (2)	∞	0.318 (3)
	240	∞	58 (1)	∞	0.350 (3)
	260	∞	39.9 (4)	∞	0.392 (2)
Pbca HT	280	53.0 (7)	7.1 (1)	∞	0.294 (2)
	300	26.7 (7)	4.3 (1)	∞	0.269 (3)
	320	17.1 (6)	3.6 (1)	∞	0.316 (2)
	350	10.1 (4)	3.1 (1)	∞	0.405 (2)
	370	8.3 (4)	4.0 (2)	∞	0.454 (2)

The C_4 mode is activated only in the $Pbca$ HT phase ($280\ K \leq T \leq 370\ K$ upon heating) while it is frozen ($\tau_{C_4} \to \infty$) in the $Pbca$ LT phase ($120\ K \leq T \leq 260\ K$ upon heating). The C_3 modes are activated in both $Pbca$ HT and LT phases. The C_2 modes are frozen in both phases, i.e., $\tau_{C_2} \to \infty$. In (Eq. 21), $\sqrt{\langle u^2 \rangle} = \sqrt{U_{iso}}$ is the isotropic atomic displacement parameter of all the H atoms in BA^+. The number in the parenthesis is the standard error for the corresponding fitting parameters.

In the low temperature orthorhombic phase ($Pbca$ LT, at 120, 200, 260 K), the elastic signal shows a gradual decrease with increasing Q (Figure 26A) while low energy quasi-elastic signals, on the other hand, show a weak peak centered at Q larger than 2 Å^{-1} (Figure 26B, C), which can be explained by the C_3 rotational modes of NH_3 and CH_3 groups with small rotational radii. In the high temperature orthorhombic phase ($Pbca$ HT, at 280, 320, 370 K), on the other hand, the elastic signal decays faster with increasing Q while the inelastic signal shows a peak at ~ 1.5 Å^{-1}. These features can be explained by $C_4 \otimes C_3$ rotational modes, in which the C_3 modes have smaller rotational radii and shorter relaxation time and the C_4 mode has larger rotational radii and longer relaxation time. The different Q dependences of the QENS signal demonstrate the prominent difference in the rotational radius, and hence the rotational mode for the two phases.

5.4 Energy Barrier of Rotational Modes

In order to justify the constraints we applied on τ_{C_4} and τ_{C_2}, we estimated the energy barriers for the C_4, C_3 and C_2 modes using the density-functional theory (DFT) calculations (see Section 2.4.1 for details). For each mode, a possible rotational path was considered, and a series of intermediate lattice structures were generated along this path. Then for the intermediate lattice structures of a specific rotational model, the total electronic energy was estimated after relaxing the positions of the inorganic atoms (Pb and I), to obtain the rotational energy barrier for the rotation mode.

As shown in Table 3, the energy barrier of the C_3 modes (3-fold rotation) of H atoms in both NH_3 and CH_3 groups located at the two ends of the BA^+ molecule is nearly the same at 0.3(1) eV for both the $Pbca$ LT and $Pbca$ HT phases. On the other hand, the energy barrier of the C_2 modes (2-fold rotation) of H atoms in each of the three CH_2 groups is estimated to be 8.1(7) eV, and also show phase independence. The large energy barrier of the C_2 modes is due to the fact that the 2-fold rotation changes the bond angle between the particular CH_2 and its neighboring C or N atoms. Therefore, the C_2 modes should be forbidden at both phases. The energy barrier of the C_4 mode (4-fold gyration motion) of the whole BA^+ molecule along the crystallographic *c*-axis is estimated to be ~ 0.5 eV for the $Pbca$ HT structure, while it is much larger than 6.5 eV for the $Pbca$ LT structure. This huge energy barrier of the C_4 mode in the $Pbca$ LT phase is due to the larger tilting angle between the BA^+ molecule and the C_4 rotation axis (see Figure 24A), which may cause collisions between the neighboring BA^+ molecules during the rotation. From the above discussions, we assumed for simplicity that the C_3 modes survive in both the $Pbca$ LT and $Pbca$ HT phases, while the C_4 mode only exists in the $Pbca$ HT phase, and the C_2 modes are absent in both phases.

Table 3. Energy Barriers for BA^+ Jump Rotation Mode C_4, C_3 and C_2.

Mode	Energy Barrier (eV)		
	Isolated BA^+	*Pbca* LT	*Pbca* HT
C_4	0	> 6.5	0.50
$C_3^{NH_3}$	0.10	0.22	0.35
$C_3^{CH_3}$	0.13	0.16	0.12
$C_2^{CH_2[1]}$	8.8	8.8	8.8
$C_2^{CH_2[2]}$	7.9	7.9	7.9
$C_2^{CH_2[3]}$	7.6	7.6	7.6

The energy barriers for the C_4, C_3 and C_2 modes, were calculated using DFT calculations. For C_4 mode, the energy barrier is defined as the average of jump barrier from site $i \rightarrow j$, where i, j are the adjacent 4-fold sites. For C_2 mode, only the barrier for isolated BA^+ molecule is calculated, the barriers for the $Pbca$ HT and $Pbca$ LT phase are taken as the values from isolated BA^+ molecule, considering that the influence of the $[PbI_4]^{2-}$ crystal field is small on the $-CH_2-$ groups. The calculation details are shown in Figure 39 - Figure 41 at Appendix 3.

5.5 Comparison with $MAPbI_3$

To sum up, there are two types of jump rotation modes in $(BA)_2PbI_4$, i.e., the C_3 modes of NH_3, CH_3 groups which exist for both structural phases, and the C_4 mode of the entire BA^+ molecule, which is only activated at the $Pbca$ HT phase. And the C_4 mode appears right after the phase transition at 280 K, showing a characteristic relaxation time of 53(7) ps. Similar C_3 and C_4 rotational modes were also found in $MAPbI_3$ [58]. In $MAPbI_3$, the C_3 mode is active in all the three structural phases, while the C_4 mode only emerges in the intermediate-temperature tetragonal phase ($I4/mcm$) and the high-temperature cubic phase ($Pm\bar{3}m$).

However, differences still exist between the rotational modes of $(BA)_2PbI_4$ and $MAPbI_3$. For the C_3 mode of $MAPbI_3$, the connected NH_3 and CH_3 rotate together and simultaneously, while in $(BA)_2PbI_4$, the rotations of NH_3 and CH_3, which are separated by the $CH_2CH_2CH_2$ chain, are independent. And for the C_4 rotation, in $MAPbI_3$, the C_4 rotation axis is perpendicular to the molecule axis, which is passing through the terminal C and N atoms, therefore, the MA^+ molecule can flip entirely during the C_4 rotation. On the other hand, in $(BA)_2PbI_4$, due to the larger size of BA^+ molecule and the interaction between the NH_3 group and the nearby $[PbI_4]^{2-}$ layer, the molecule cannot rotate as freely as MA^+. The BA^+ molecule axis is slightly tilted (with a ~ 28 ° tilting angle at the $Pbca$ HT phase) away from the C_4 rotation axis, which is along the out-of-perovskite-layer c-direction, thus the C_4 rotation of BA^+ molecules is merely a “gyration”.

Furthermore, our results show that the appearance of the C_4 mode of BA^+ molecule does not affect the PL lifetimes. Comparing Figure 22B and Figure 26D, it shows no significant change of the charge carrier lifetimes, especially for the *majority* carriers, when the C_4 mode gets activated at the phase transition. This feature of $(BA)_2PbI_4$ is in contrast to that in $MAPbI_3$, which shows a sudden jump in the charge carrier lifetimes and the dielectric response upon heating, coupled with the activation of the C_4 rotational mode of MA^+ molecule [14, 58, 130]. This provides another evidence of exciton-dominant picture in $(BA)_2PbI_4$ since the excitons are charge neutral and are expected to be minimally affected by rotation of the surrounding polarized molecules, which is especially true for the tightly bound excitons in the 2D HOIPs.

Chapter 6.

Vibrational Dynamics

Identification of phonon modes for the experimentally measured peaks using the density-functional theory (DFT) calculations and molecular dynamics (MD) simulations has been challenging [144, 145]. In this chapter, we use the inelastic neutron scatterings and DFT calculations to study the vibrational modes of $(BA)_2PbI_4$ and $MAPbI_3$. We have found that significant van der Waals (vdW) interactions (London dispersion forces) with an advanced non-local vdW correction functional, vdW-DF2 [95-98], need to be included to reproduce the phonon spectra. Furthermore, other phonon features, e.g., phonon melting, in HOIPs will also be discussed.

6.1 Inelastic Neutron Scattering Measurements

The inelastic neutron scattering (INS) spectra of $(BA)_2PbI_4$ and $MAPbI_3$ were measured at 4SEASONS, MLF, J-PARC and ARCS, SNS, ORNL, respectively (see Section 2.2.2.3 for the experiment details). Figure 27 shows the contour maps of INS intensities $S(Q,\hbar\omega)$ obtained at two different temperatures, 10 K and 300 K, for $(BA)_2PbI_4$ and $MAPbI_3$. For each sample, three different E_i settings were plotted to show the data over the entire vibrational energy region up to ~ 600 meV with optimized energy resolutions. At 10 K, the contour maps exhibit many nearly dispersionless peaks from a few meV to ~ 400 meV. These peaks are well defined in energy, which means that at 10 K the collective vibrational motions are coherent over the lattice and in time, and they can be described by quasi-particles called phonons. At 300 K, however, $S(Q, \hbar\omega)$ becomes featureless at low energies for both systems, which indicates that the low energy vibrational motions lose coherence in time, i.e., the phonons are melted.

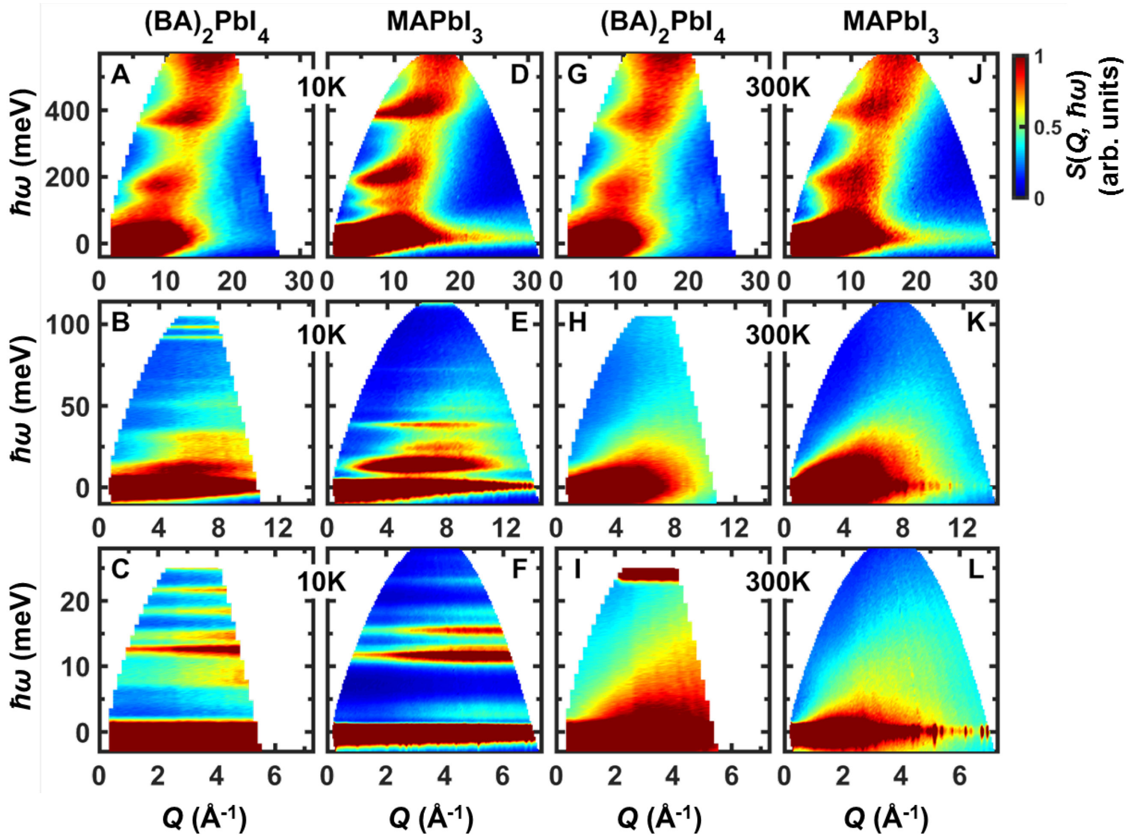

Figure 27.Inelastic Neutron Scattering Spectra of $(BA)_2PbI_4$ and $MAPbI_3$.

(A - C) and (G - I) are the inelastic neutron scattering (INS) intensity $S(Q, \hbar\omega)$ *of* $(BA)_2PbI_4$ *as a function of momentum transfer* Q *and energy transfer* $\hbar\omega$*, obtained with incident neutron energies* $E_i = 712$ *meV (A and G), 115 meV (B and H), and 30 meV (C and I). The data shown in A - C are taken at 10 K and the data shown in G - I are taken at 300 K. (D - F) and (J - L) show the INS intensity* $S(Q, \hbar\omega)$ *of* $MAPbI_3$ *obtained with* $E_i =$ *600 meV (D and J), 120 meV (E and K), and 30 meV (F and L). The data shown in D - F are taken at 10 K and the data shown in J - L are taken at 300 K.*

6.2 Phonon Modes

In order to identify all the INS peaks shown in Figure 27 and reproduce the phonon spectra theoretically, we have computed the phonon density of states (PDOS) through DFT calculations (see Section 2.4.2 for the calculation details). The PDOSs of $(BA)_2PbI_4$ and $MAPbI_3$ are shown in Figure 28 and Figure 29. For comparison purpose, the $\mathit{\Gamma}$-point phonon modes for isolated BA^+ and MA^+ molecule are also plotted with the dark green marks in Figure 28 and Figure 29. The details of several selected phonon modes are shown in Figure 28 *1 – 8* and Figure 29 *1 – 8*, Table 12 and Table 13 at Appendix 4, for $(BA)_2PbI_4$ and $MAPbI_3$, respectively.

Our results in Figure 28 and Figure 29, Table 12 and Table 13 at Appendix 4 clearly demonstrate that van der Waals (vdW) correction is critical to reproduce the peaks in the experimental Q-integrated INS intensity, $S(\hbar\omega) = \int S(Q, \hbar\omega)\, dQ$. For instance, without vdW correction, the INS peak at 29.7(1) meV of $(BA)_2PbI_4$ cannot be reproduced by the calculated PDOS. When the vdW interaction is included, the twisting modes $T_{NH_3-CH_2CH_2}$ (mode 4 in Figure 28) becomes much softer than the $T_{CH_2CH_2-CH_3}$ (mode 5), and our calculation matches well with the experimental peak. As shown in Table 12 at Appendix 4, the percentage difference between the calculated and experimental phonon energy for the $T_{NH_3-CH_2CH_2}$ mode is 28.5% without vdW correction, while it is 3.0% with the vdW correction. The differences for other phonon modes of $(BA)_2PbI_4$ located from 10 meV to 100 meV are less than ~ 5% even without vdW correction, and the vdW-DF2 correction only yields small improvements for such modes. It is to be noted that the prominent vdW-induced redshift occurs for the $T_{NH_3-CH_2CH_2}$ mode that involves significant atomic displacement of three H atoms in the NH_3 group that is closed to the $[PbI_4]^{2-}$ layer.

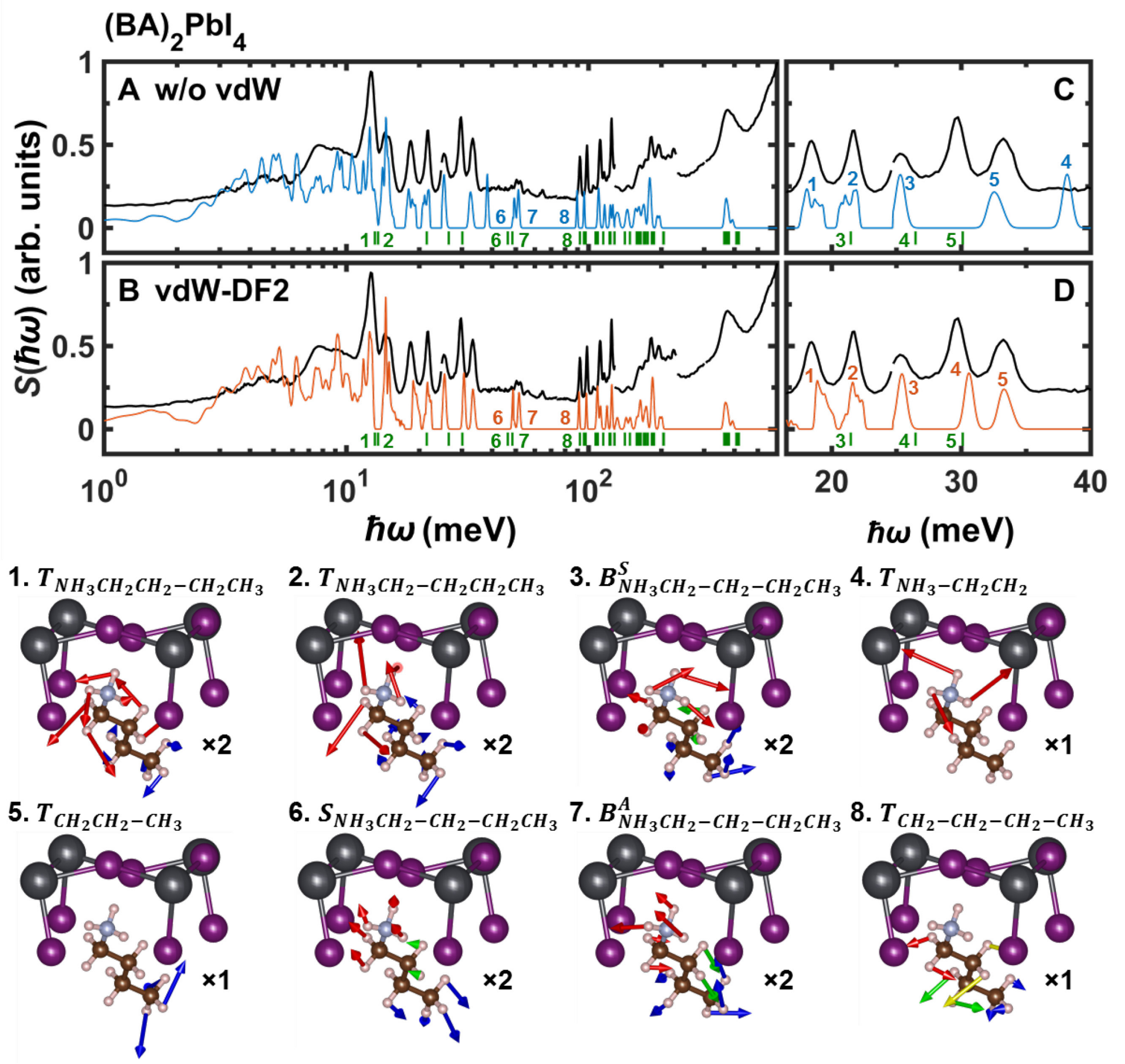

Figure 28.Phonon Density of States and Eigenmodes of $(BA)_2PbI_4$.

In (A and B), the black lines are the Q*-integrated INS intensity* $S(\hbar\omega) = \int S(Q, \hbar\omega)\, dQ$ *of* $(BA)_2PbI_4$ *measured at 10 K. (C and D) show the data from ħω = 16.5 to 40 meV. The blue lines in A and C are the calculated PDOS without van der Waals (vdW) corrections while the red lines in B and D are the calculated PDOS with vdW corrections. Dark green marks in A - D represent the calculated phonon energies for an isolated* BA^+ *molecule. (1 - 8) illustrate phonon modes for peaks labeled by 1 - 8 in A - D. The number on the right bottom in each mode represents a multiplication factor multiplied to the phonon amplitude for visualization. Here, the gray, violet, cyan, brown and pink spheres represent the Pb, I, N, C and H atoms, respectively.*

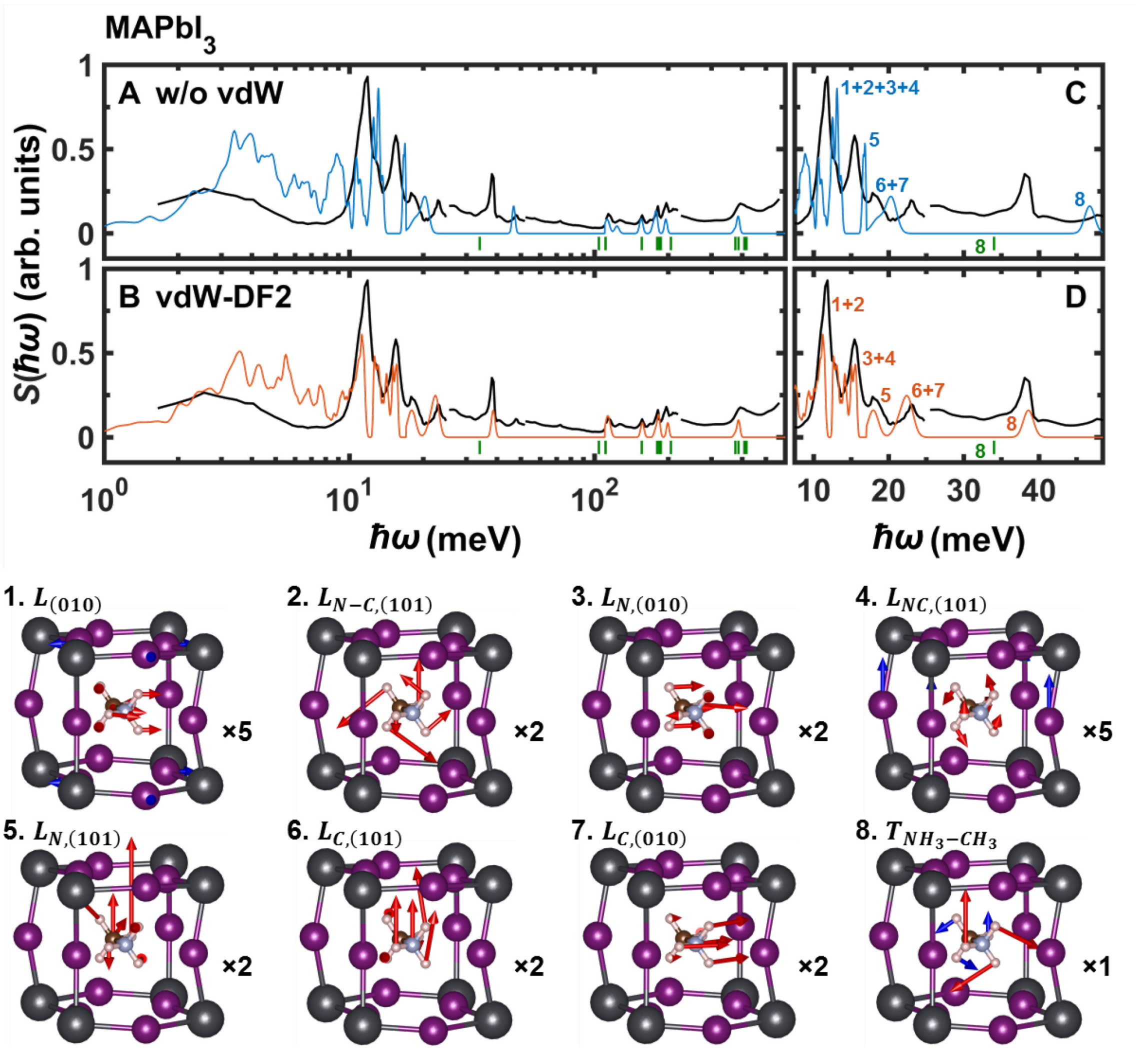

Figure 29.Phonon Density of States and Eigenmodes of MAPbI$_3$.

In (A and B), the black lines are the Q-integrated INS intensity $S(\hbar\omega) = \int S(Q,\hbar\omega)\,dQ$ *of MAPbI$_3$ measured at 10 K. (C and D) show the data from ħω = 7.5 to 48.5 meV. The blue lines in A and C are the calculated PDOS without van der Waals (vdW) corrections while the red lines in B and D are the calculated PDOS with vdW corrections. Dark green marks in A - D represent the calculated phonon energies for an isolated MA$^+$ molecule. (1 - 8) illustrate phonon modes for peaks labeled by 1 - 8 in A - D. The number on the right bottom in each mode represents a multiplication factor multiplied to the phonon amplitude for visualization. Here, the gray, violet, cyan, brown and pink spheres represent the Pb, I, N, C and H atoms, respectively.*

The role of the vdW corrections becomes more pronounced for $MAPbI_3$, where the organic molecules are confined in the inorganic $[PbI_3]^-$ cage consisting of Pb and I of high C_6 coefficients [146]. The twisting modes $T_{NH_3-CH_3}$ (mode 8 in Figure 29) shifted from 46.7(2) meV to 38.6(2) meV with vdW correction, well reproducing the INS peak at 38.2(1) meV. The percentage difference between the calculated and experimental phonon energy was 22.4% without vdW correction, and it was reduced to 1.0% with the vdW-DF2 correction (see Table 13 at Appendix 4 for details). For other phonon modes that exist between 11 meV and 24 meV, the vdW-DF2 correction also significantly reduced the percentage differences from ~ 10% (without vdW correction) to less than ~ 5%. In conclusion, we demonstrated that DFT calculations with vdW-DF2 correction are a proper method to reproduce the low T phonon spectra of $(BA)_2PbI_4$ ($Pbca$ LT phase) and $MAPbI_3$ ($Pnma$ phase).

In the discussion above, we mainly focus on the phonon modes within the energy range of $10 \leq \hbar\omega \leq 100$ meV, which are significantly affected by the inclusion of vdW corrections. However, some of the lower energy modes, which largely involve the motion of inorganic atoms, are very crucial to the optoelectronic properties of the HOIPs. The Pb-I-Pb bending and Pb-I stretching modes were claimed to be responsible for polaron formation and hence the high photovoltaic efficiencies in HOIPs [69, 125, 147, 148]. The detailed information of the Pb-I-Pb bending and Pb-I stretching modes within the energy range $2.6 \leq \hbar\omega \leq 16$ meV are shown in Table 14 and Table 15 at Appendix 4 for $(BA)_2PbI_4$ and $MAPbI_3$, respectively.

6.2.1 Influence of van der Waals Correction

In order to further verify our phonon mode identification, especially for the $T_{NH_3-CH_2CH_2}$ mode of $(BA)_2PbI_4$ and $T_{NH_3-CH_3}$ mode of $MAPbI_3$, we study the temperature dependence of their energies. Here, shown in Figure 30, we use $(BA)_2PbI_4$ as an example. We extracted the temperature-dependent energies of peak 4 and its neighboring peak 3 and 5 (shown in Figure 28) from the INS spectra of $(BA)_2PbI_4$ and plotted them as the blue circles, red squares and yellow diamonds in Figure 30. The experimental INS peak energies clearly show different T dependences: peak 4 is "hardening", i.e., the phonon energy increases for an increasing T; while peak 3 and 5 are "softening", i.e., the phonon energies decrease when T increases.

To confirm the correspondence between the INS peak 4 and the $T_{NH_3-CH_2CH_2}$, what we need to do is to verify whether the calculated phonon energy of $T_{NH_3-CH_2CH_2}$ shows a "hardening" feature. The temperature-dependent phonon energies of the $T_{NH_3-CH_2CH_2}$ and $B^S_{NH_3CH_2-CH_2-CH_2CH_3}$, $T_{CH_2CH_2-CH_3}$ modes are simulated by DFT calculations, shown as the blue, red and yellow lines in Figure 30. In order to simulate the temperature's effect on the DFT calculations, we manually increase the size of the unit cell by a temperature-dependent scaling factor extracted from the SPINS structure data shown in Figure 19. Our results show that, for the calculation both without vdW correction (Figure 30A) and with vdW-DF2 correction (Figure 30B), the $T_{NH_3-CH_2CH_2}$ mode is always "hardening", while $B^S_{NH_3CH_2-CH_2-CH_2CH_3}$ and $T_{CH_2CH_2-CH_3}$ are "softening" when T increases.

Therefore, our DFT calculations demonstrate that the INS peak at 38.2(1) meV should indeed be assigned to the $T_{NH_3-CH_2CH_2}$ twisting mode. And by applying the vdW-

DF2 correction, the energy of $T_{NH_3-CH_2CH_2}$ mode, along with other phonon modes, can be well reproduced.

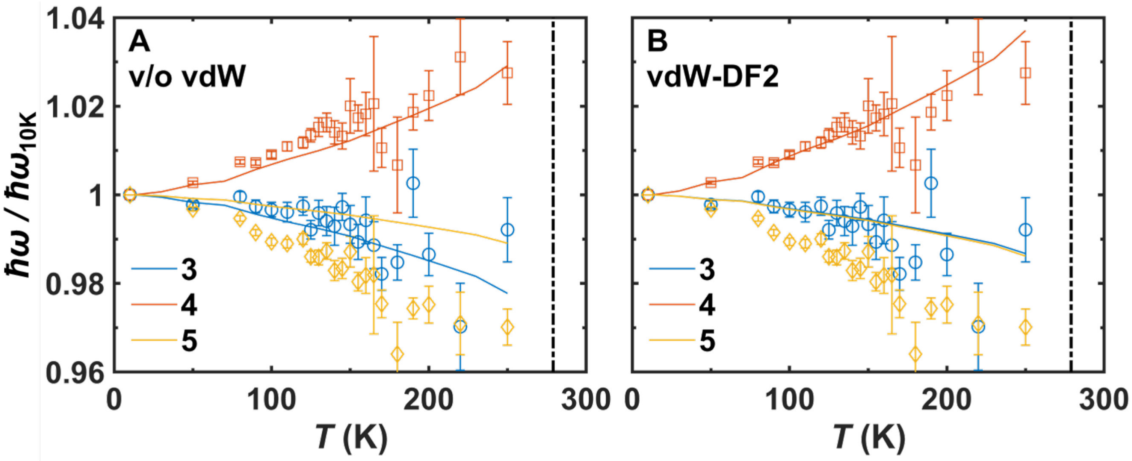

Figure 30.Temperature Dependence of Phonon Energies for $(BA)_2PbI_4$.

In (A and B), the blue, red and yellow solid lines show the calculated phonon energies, $\hbar\omega$*, of mode 3 (*$B^S_{NH_3CH_2-CH_2-CH_2CH_3}$*), 4 (*$T_{NH_3-CH_2CH_2}$*) and 5 (* $T_{CH_2CH_2-CH_3}$*) for* $(BA)_2PbI_4$ *orthorhombic low T (*$Pbca$ *LT) phase without vdW correction (A) and with vdW-DF2 correction (B). The blue circles, red squares and yellow diamonds represent the phonon energies of mode 3, 4 and 5 fitted from the* Q*-integrated INS intensity. The phonon energies for each mode were normalized with the value at 10 K,* $\hbar\omega_{10K}$*.*

It should be noted that we also tried other types of vdW correction functionals, e.g., optB88-vdW and optB86b-vdW. The results from different vdW corrections are shown in Figure 43 and Figure 44 at Appendix 4 for $(BA)_2PbI_4$ and $MAPbI_3$, respectively. Among all these correction functionals, vdW-DF2 can reproduce the experimental phonon spectra with the best quality, so here we mainly focus on the discussion of the vdW-DF2 correction in the main text.

6.2.2 Estimation of Electronic Interactions

In this part, the van der Waals (vdW) interactions are further studied by directly extracting the magnitudes of calculated electronic interaction energies between different components in $(BA)_2PbI_4$ and $MAPbI_3$, e.g., between adjacent molecules, and between a molecule and its nearby inorganic perovskite atoms.

The total electronic energy, E_{elec}, of a system can be read from the DFT output files. However, in order to obtain the inter-molecule electronic energy, the intra-molecule component and some constant terms must be eliminated. Generally, the electronic interaction between two subsystems A and B, i.e., E_{elec}^{A-B}, can be expressed as

$$E_{elec}^{A-B} = E_{elec}(A+B) - E_{elec}(A) - E_{elec}(B), \tag{Eq. 22}$$

where $E_{elec}(A+B)$ is the total electronic energy when both subsystem A and B exist, $E_{elec}(A)$ and $E_{elec}(B)$ are the electronic energies of isolated subsystem A and B.

The DFT calculations were performed with the electronic relaxation and the vdW-DF2 correction with a single electron wavevector, $\boldsymbol{k} = (0, 0, 0)$. The ionic structures of subsystem A and B and their relative positions were extracted from relaxed structures of $(BA)_2PbI_4$ and $MAPbI_3$ with vdW-DF2 correction. For isolated molecule and molecule pair systems (A, B contains BA^+ and MA^+ only), a 40×40×40 Å cell was used. And a 3×3×2 or 3×2×3 supercell was used when $[PbI_4]^{2-}$ or $[PbI_3]^-$ were included, for $(BA)_2PbI_4$ and $MAPbI_3$, respectively. By performing DFT calculations on isolated subsystem A, B, and with both subsystems included, we were able to extract $E_{elec}(A)$, $E_{elec}(B)$ and $E_{elec}(A+B)$, and hence to calculate the value of E_{elec}^{A-B}. With the same DFT calculations, the vdW dispersion energy can also be extracted as the energy contribution from the vdW-

DF2 correction. Similarly, the vdW dispersion interaction between two subsystem A and B can be written as

$$E_{vdW}^{A-B} = E_{vdW}(A+B) - E_{vdW}(A) - E_{vdW}(B),$$

(Eq. 23)

where $E_{vdW}(A)$, $E_{vdW}(B)$ and $E_{vdW}(A+B)$ are the dispersion energy for isolated subsystem A, B and for when both A and B are included.

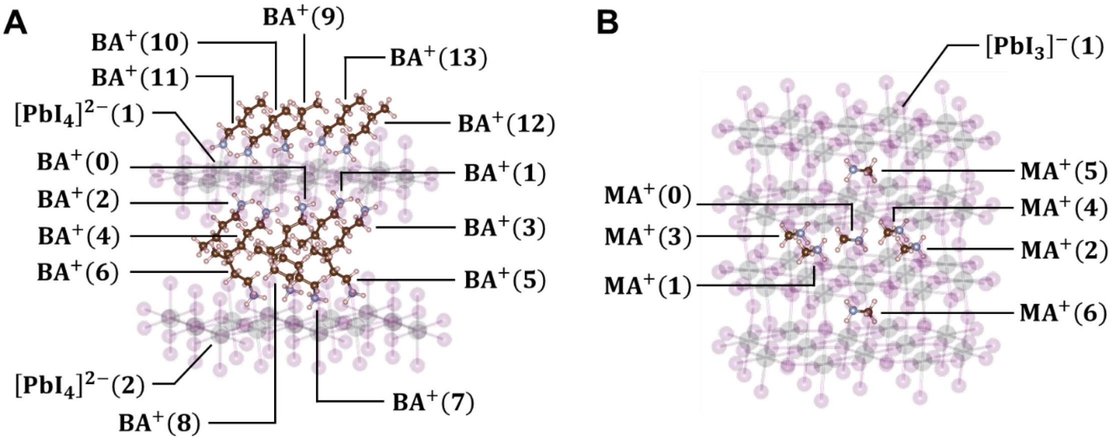

Figure 31.Molecule Configurations for Electronic Interaction Estimation in $(BA)_2PbI_4$ and $MAPbI_3$.

(A and B) show the BA^+ and MA^+ molecules, along with the surrounding $[PbI_4]^{2-}$ and $[PbI_3]^-$ inorganic structures used for the electronic interaction estimations in $(BA)_2PbI_4$ and $MAPbI_3$, respectively.

Note that in $(BA)_2PbI_4$ ($Pbca$ LT phase) and $MAPbI_3$ ($Pnma$ phase), the space group symmetry guarantees that all the BA^+ or MA^+ molecule are identical. Thus, we chose the subsystem A to be one specific BA^+ or MA^+ molecule in the unit cell, denoted as $A = BA^+(0)$ or $A = MA^+(0)$. For $(BA)_2PbI_4$, 13 different BA^+ molecules close to the $BA^+(0)$, labeled as $\mathrm{BA}^{+}(1)$ – $\mathrm{BA}^{+}(13)$ and 2 nearby $[\mathrm{PbI}_4]^{2-}$ layers $[\mathrm{PbI}_4]^{2-}(1)$ and $[\mathrm{PbI}_4]^{2-}(2)$, were set to be the subsystem B, shown in Figure 31A. And for MAPbI_3, 6 closest MA^{+} molecules, $\mathrm{MA}^{+}(1)$ – $\mathrm{MA}^{+}(6)$ and the whole 3D inorganic perovskite, $[\mathrm{PbI}_3]^{-}(1)$, were used for the subsystem B, shown in Figure 31B.

The values of total electronic interactions, E_{elec}^{A-B}, and the vdW interactions, E_{vdW}^{A-B}, between different subsystems are listed in Table 16 and Table 17 at Appendix 4 for $(\mathrm{BA})_2\mathrm{PbI}_4$ and MAPbI_3, respectively. For both HOIPs, the largest E_{elec}^{A-B} component comes from the interactions between the organic molecule and its nearest neighboring inorganic perovskite structures, for instance, $E_{elec}^{\mathrm{BA}^{+}(0)-[\mathrm{PbI}_4]^{2-}(1)} \approx -6.164\ \mathrm{eV}$, and $E_{elec}^{\mathrm{MA}^{+}(0)-[\mathrm{PbI}_3]^{-}(1)} \approx -6.784\ \mathrm{eV}$, which is due to the short distance between them. For the closest atoms in $\mathrm{BA}^{+}(0)$ and $[\mathrm{PbI}_4]^{2-}(1)$, the distance $d_{min}^{\mathrm{BA}^{+}(0)-[\mathrm{PbI}_4]^{2-}(1)} \approx 2.60\ \text{Å}$, which is smaller than most BA^{+}-BA^{+} distances. For MAPbI_3, $d_{min}^{\mathrm{MA}^{+}(0)-[\mathrm{PbI}_3]^{-}(1)} \approx 2.54\ \text{Å}$, nearly half of the inter-molecule distances. The inter-molecule electronic interactions have smaller values, ~ 1.1 eV and 1.3 eV for the nearest neighboring BA^{+} and MA^{+} molecules. The positive sign of the inter-molecule electronic interaction reveals the repulsive Coulomb forces between the molecules with the same net charge.

For the vdW dispersion energy, the maximum values also exist between the molecule and the inorganic structures. $E_{vdW}^{\mathrm{BA}^{+}(0)-[\mathrm{PbI}_4]^{2-}(1)} \approx -0.814\ \mathrm{eV}$, which contributes ~ 13.2% of the total electronic energy between the two components, and $E_{vdW}^{\mathrm{MA}^{+}(0)-[\mathrm{PbI}_3]^{-}(1)} \approx -0.912\ \mathrm{eV}$, with an energy contribution of ~ 13.4%. The magnitudes of inter-molecule E_{vdW}^{A-B} are relatively smaller. The largest values of E_{vdW}^{A-B} for $(\mathrm{BA})_2\mathrm{PbI}_4$

and MAPbI$_3$ are $E_{vdW}^{\mathrm{BA^+(0)-BA^+(3)}} \approx -0.125\ \mathrm{eV}$ and $E_{vdW}^{\mathrm{MA^+(0)-MA^+(3)}} \approx -0.007\ \mathrm{eV}$, and their contributions to the total electronic energies are ~ -11.3% and ~ -0.5%, respectively.

In conclusion, through the estimated electronic interactions, we discovered that the electronic and vdW interactions have large values between the BA$^+$ (or MA$^+$) cations and the adjacent [PbI$_4$]$^{2-}$ (or [PbI$_3$]$^-$) perovskite structures. In particular, the large vdW interactions between BA$^+$ and [PbI$_4$]$^{2-}$ or MA$^+$ and [PbI$_3$]$^-$ explain the significant influence on the restoring force, as well as the phonon energy, of the twisting mode of the NH$_3$ group in the BA$^+$ or MA$^+$ molecule.

6.2.3 Phonon Amplitude and Energy Fractions

To understand the phonon modes and to categorize them in the full energy range, we have calculated the vibrational amplitude and energy fractions, i.e., the contributions of different types of atoms to the amplitude and energy of each phonon mode, for both HOIPs. The vibrational amplitude fraction (VAF) and vibrational energy fraction (VEF) of each type of atoms (t = Pb, I, N, C, H) are defined as

$$\mathrm{VAF}_t(s,\boldsymbol{q}) = \frac{\sum_{d\in t}\sqrt{\langle \boldsymbol{u}_{ds}^2\rangle}}{\sum_{d\in all}\sqrt{\langle \boldsymbol{u}_{ds}^2\rangle}},$$

$$\mathrm{VEF}_t(s,\boldsymbol{q}) = \frac{\sum_{d\in t} M_d\omega_s^2\langle \boldsymbol{u}_{ds}^2\rangle}{\sum_{d\in all} M_d\omega_s^2\langle \boldsymbol{u}_{ds}^2\rangle},$$

(Eq. 24)

where $\sqrt{\langle \boldsymbol{u}_{ds}^2\rangle}$ is mean square root displacement of the d-th nucleus due to the activation of phonon mode s (associated with a wavevector $\boldsymbol{q}$ and a polarization index j). According (Eq. 19) in Section 2.2.1.4, $\sqrt{\langle \boldsymbol{u}_{ds}^2\rangle} = \sqrt{\frac{\hbar}{2NM_d\omega_s}\langle 2n_s+1\rangle}\boldsymbol{e}_{ds}$, where $\hbar$ is the reduced

Planck constant, N is the number of the unit cells, M_d mass of d-th nucleus, ω_s, n_s are the angular frequency, quantum number of phonon mode s, and $\boldsymbol{e}_{ds}$ is the polarization vector of nucleus d with phonon mode s.

By limiting the calculations to $N = 1$ and $T \rightarrow 0$, then based on (Eq. 5) in Section 2.2.1.1, we have $\sqrt{\langle \boldsymbol{u}_{ds}^2 \rangle} = \sqrt{\frac{\hbar}{2M_d\omega_s}}\boldsymbol{e}_{ds}$. Therefore, (Eq. 24) can be rewritten as

$$\mathrm{VAF}_t(s, \boldsymbol{q}) = \frac{\sum_{d\in t}\frac{|\boldsymbol{e}_{ds}|}{\sqrt{M_d}}}{\sum_{d\in all}\frac{|\boldsymbol{e}_{ds}|}{\sqrt{M_d}}},$$

$$\mathrm{VEF}_t(s, \boldsymbol{q}) = \frac{\sum_{d\in t} M_d\omega_s^2\langle \boldsymbol{u}_{ds}^2\rangle}{\sum_{d\in all} M_d\omega_s^2\langle \boldsymbol{u}_{ds}^2\rangle} = \frac{\sum_{i\in t}|\boldsymbol{e}_{ds}|^2}{\sum_{i\in all}|\boldsymbol{e}_{ds}|^2}.$$

(Eq. 25)

Using (Eq. 25), the vibrational amplitude and energy fractions of $(BA)_2PbI_4$ and $MAPbI_3$ were calculated at the phonon Γ point ($\boldsymbol{q} = (0, 0, 0)$). According to the vibrational amplitude and energy fraction results shown in Figure 32, we can assign the phonon modes of $(BA)_2PbI_4$ and $MAPbI_3$ into three categories: i) the low energy mostly-inorganic modes within the energy range of 0 ~ 10 meV, in which inorganic atoms, Pb and I, contributes a large portion of the vibrational amplitudes and most of the vibrational energies; ii) the intermediate energy hybrid modes within the energy range of 10 ~ 30 (or 40) meV, in which both inorganic and organic atoms have significant contributions in the phonon vibrations; iii) the high energy purely-organic modes within the energy range of 30 (or 40) ~ 400 meV, in which the organic atoms, N, C and H contribute nearly the entire vibrational amplitudes and vibrational energies.

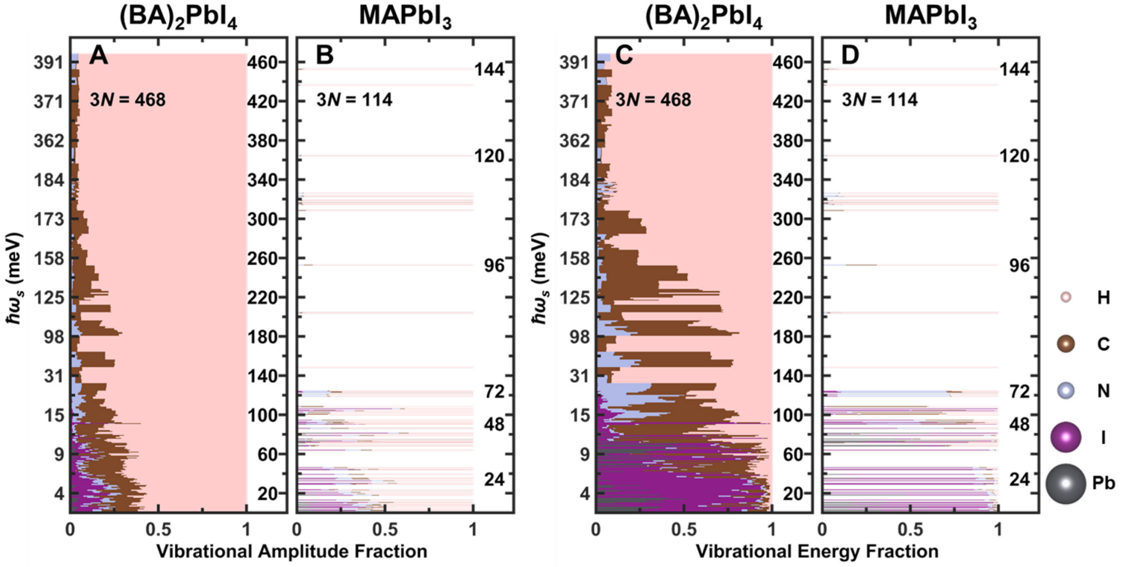

Figure 32.Vibrational Amplitude and Energy Fractions for (BA)$_2$PbI$_4$ and MAPbI$_3$.

(A and B) the vibrational amplitude fractions calculated for (BA)$_2$PbI$_4$ (A) and MAPbI$_3$ (B). (C and D) the vibrational energy fractions calculated for (BA)$_2$PbI$_4$ (C) and MAPbI$_3$ (D). The integer numbers on the right side of A, C and B, D denote the phonon mode index of the $3N = 462$ *modes for (BA)$_2$PbI$_4$ and* $3N = 144$ *modes for MAPbI$_3$. The energies of the modes,* $\hbar\omega_s$*, are indicated on the left, which are unequally distributed. The vibrational amplitude and energy fractions for each type of atom are represented by the bar width with the same color as the corresponding atom shown on the right side of D.*

6.2.4 Electron-Phonon Interaction

As was discussed in Section 4.1, the electron-phonon coupling is very crucial to the large polaron formation in HOIPs [111, 117-122]. In this section, we utilize DFT calculations to estimate the strengths of electron-phonon interactions in (BA)$_2$PbI$_4$ and MAPbI$_3$. In our calculations, the electron-phonon interaction is represented by the electronic band structure perturbation caused by the phonon mode displacement, which reveals how the electrons are affected by the specific phonon modes. In particular, the change of electronic bandgap (E_g) can be computed as

$$\Delta E_g = E_g\left(\boldsymbol{r}_d = \sqrt{2\langle \boldsymbol{u}_{ds}^2 \rangle}\right) - E_g(\boldsymbol{r}_d = 0),$$

(Eq. 26)

where $\boldsymbol{r}_d$ is the applied displacement of the d-th atom from its equilibrium position, $\sqrt{2\langle \boldsymbol{u}_{ds}^2 \rangle}$ is the maximum displacement due to the activation of phonon mode s, which is $\sqrt{2}$ times the mean square root displacement $\sqrt{\langle \boldsymbol{u}_{ds}^2 \rangle} = \sqrt{\frac{\hbar}{2M_d\omega_s}}\boldsymbol{e}_{ds}$ at $T \to 0$, as discussed in Section 6.2.3.

Considering the lattice symmetry, the electronic band structures were calculated at $\boldsymbol{q} = (0,0,0)$ (phonon wavevector) along the high-symmetry $\boldsymbol{k}$ (electron wavevector) path, that is $\Gamma(0,0,0) \to X(1/2,0,0) \to S(1/2,1/2,0) \to Y(0,1/2,0) \to \Gamma(0,0,0) \to Z(0,0,1/2)$ for $(BA)_2PbI_4$ $Pbca$ LT phase, and $\Gamma(0,0,0) \to X(1/2,0,0) \to U(1/2,0,1/2) \to Z(0,0,1/2) \to \Gamma(0,0,0) \to Y(0,1/2,0)$ for $MAPbI_3$ $Pnma$ phase.

The calculated phonon-induced electronic bandgap perturbation, ΔE_g, are shown in Figure 33A and C, for $(BA)_2PbI_4$ and $MAPbI_3$, respectively. Besides the mostly-inorganic modes at low energies, we also identified some modes with significant organic contributions (mainly the hybrid modes) that have large $|\Delta E_g|$ values, which means these hybrid modes are also strongly coupled to charge carriers. For instance, labeled by black arrows and shown in the insets in Figure 33A and C, the twisting mode $T_{NH_3CH_2-CH_2CH_2CH_3}$ for $(BA)_2PbI_4$ and the libration mode $L_{C,(101)}$ for $MAPbI_3$, both exhibit large electron-phonon interactions. The detailed electronic band structure perturbations caused by these two phonon modes are shown in Figure 33B and D, where the original electronic band structures at $\boldsymbol{r}_i = 0$ and perturbed electronic band structures at $\boldsymbol{r}_i = \sqrt{2\langle \boldsymbol{u}_{ds}^2 \rangle}$ are shown as black and red lines, respectively. It should be noted that the similar strong couplings between the charge carriers and the hybrid phonon modes were also reported in Ref. [149].

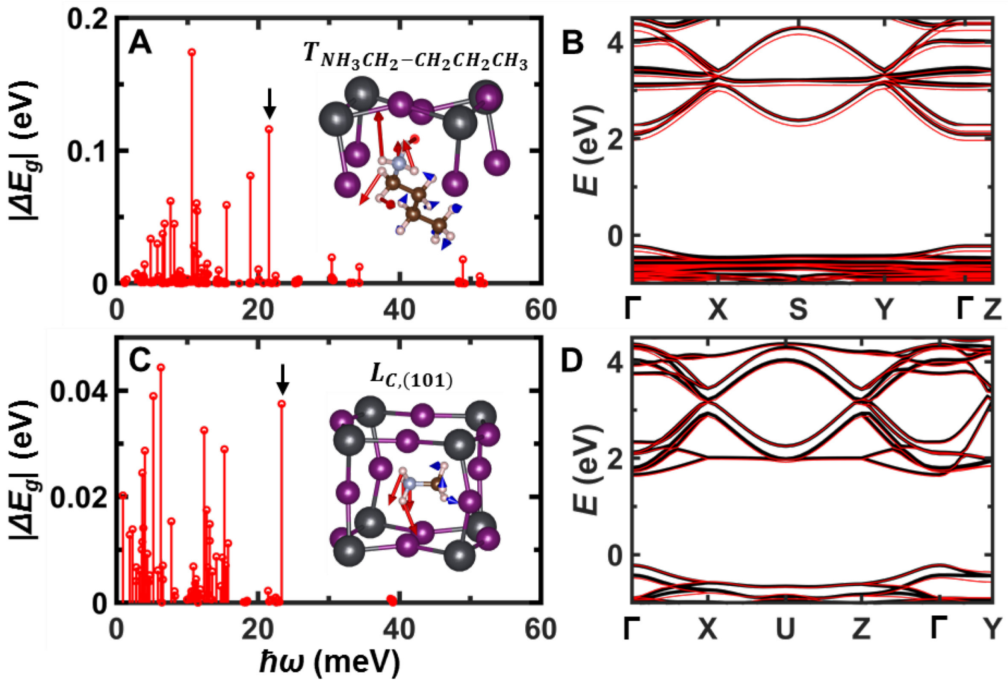

Figure 33.Phonon-Induced Electronic Band Perturbations for (BA)$_2$PbI$_4$ and MAPbI$_3$.

(A and C) show the phonon-induced electronic bandgap perturbation, ΔE_g*, for (BA)*$_2$*PbI*$_4$ *and MAPbI*$_3$*, respectively. The insets in A and C illustrate the vibrational motions of a specific phonon mode (marked by black arrow) with relatively large* $|\Delta E_g|$*, which is the twisting mode* $T_{NH_3CH_2-CH_2CH_2CH_3}$ *for (BA)*$_2$*PbI*$_4$*, and libration mode* $L_{C,(101)}$ *for MAPbI*$_3$*. (B and D) show the details of the electronic band structure perturbation for (BA)*$_2$*PbI*$_4$ *and MAPbI*$_3$*. The black lines in B and D represent the original electronic band structures without phonon motions, when all the atoms are in their equilibrium positions; the red lines show the electronic band structures with the activation of the phonon mode* $T_{NH_3CH_2-CH_2CH_2CH_3}$ *or* $L_{C,(101)}$*, when atoms deviate from their equilibrium positions.*

6.3 Phonon Melting

“Phonon melting” refers to a phenomenon that the phonon mode with well-defined sharp peak at low temperature broadens, and eventually becomes a featureless continuum, when the temperature increases. Phonon melting often occurs for a class of materials named Phonon Glass Electron Crystal (PGEC). In this section, we will discuss the phonon glass electron crystal duality and the phonon melting behavior in both $(BA)_2PbI_4$ and $MAPbI_3$.

6.3.1 Phonon Glass Electron Crystal Duality

Phonon glass electron crystal (PGEC) refers to a class of materials which exhibits the phonon glass electron crystal duality, i.e., simultaneously showing the high electric conductivity and low thermal conductivity [150, 151]. This means in PGEC, the charge transport is ballistic, while the phonon transport is diffusive [69]. The PGEC materials were initially studied for efficient thermoelectric materials in the 1990s.

The PGEC duality on HOIP materials was first studied in 2017, when O. Yaffe, et al., reported the “phonon melting” feature for the 3D HOIP, $MAPbBr_3$ and the all-inorganic MHP, $CsPbBr_3$ [68]. The well-resolved Raman spectra at orthorhombic phase for both materials became diffusive at the tetragonal phase and cubic phase, which indicates the rising of local polar thermal fluctuations, regardless of the existence of organic molecules in the materials. Therefore, the authors claimed that the origin of local polar fluctuations was related to the inorganic framework but not organic cations. Based on the “melted” phonon modes [68] and the liquid-like time-resolved optical Kerr effect (TR-OKE) responses [71] on 3D HOIPs, K. Miyata, et al., argued that the HOIPs can be categorized into PGEC [69]. In HOIPs, the large polaron formation, which can reduce the scatterings between charge carriers and charged defects, as well as the disordered phonon modes, which can block the hot carrier cooling processes through the electron-phonon scatterings, is claimed to be responsible for the excellent optoelectronic properties [71, 104, 152].

6.3.2 Melting of Inorganic, Hybrid and Organic Modes

In this section, we studied the phonon melting behaviors with temperature-dependent inelastic neutron scattering measurements on $(BA)_2PbI_4$ and $MAPbI_3$. The phonon spectra, $S(T, \hbar\omega)$, as functions of temperature, T, and energy transfer, $\hbar\omega$, are shown in Figure 34A – F and Figure 35A – F for the mostly-inorganic (C and F), hybrid (B and E) and purely-organic (A and D) modes of $(BA)_2PbI_4$ and $MAPbI_3$, respectively.

As shown in one-dimensional plots in Figure 34D – F, at 10 K (see the black curves) there are well-defined vibrational modes over the entire energy range. This means that at 10 K the collective vibrational motions are coherent over the lattice and in time, and they can be described by phonons. At 300 K (see the red curves), however, the peaks below ~ 100 meV become featureless in energy (see Figure 34E, F) while the peaks above ~ 100 meV remain sharp (see Figure 34D). This indicates that the mostly-inorganic and hybrid vibrational motions lose coherence in time, i.e., those phonons are melted. On the other hand, the purely organic vibrational modes at high energies remain coherent. To investigate how the phonon modes evolve with T, we have plotted the peak intensities of the three types, mostly-inorganic A_4 (Pb-I-Pb bending) and A_2 (Pb-I stretching), hybrid inorganic-organic A_3, and all-organic A_1, of the phonon modes as magenta circles in Figure 34I and Figure 34H, yellow triangles in Figure 34H, and magenta circles in Figure 34G, respectively. (see Table 12 and Table 14 at Appendix 4 for the mode details)

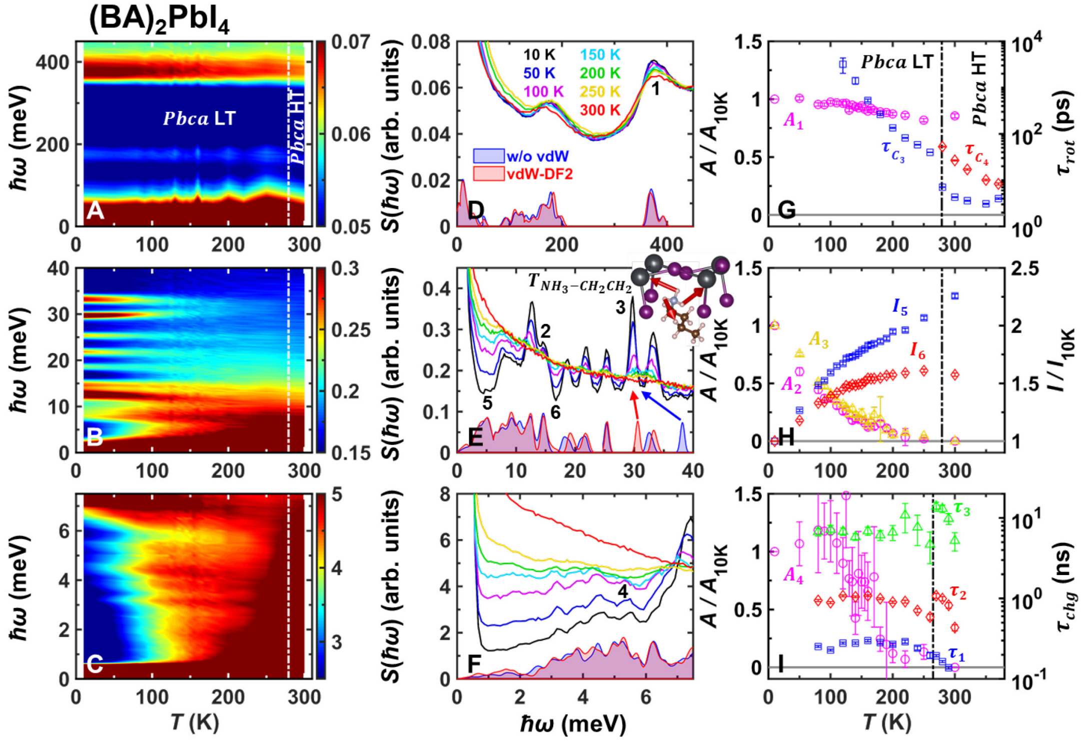

Figure 34.Temperature-Dependent Phonon Spectra of (BA)$_2$PbI$_4$.

(A - C) Color contour maps of Q*-integrated neutron scattering intensity,* $S(\hbar\omega)$*, as a function of temperature T and energy transfer ħω, taken 23 different temperatures while heating from 10 K to 300 K, with the incident neutron energy* E_i *of 712 meV (A), 62 meV (B) and 10 meV (C). (D - F) Plotted are the* $S(\hbar\omega)$ *for seven selected temperatures, 10 K, 50 K, 100 K, 150 K, 200 K, 250 K (low T orthorhombic phase (*$Pbca$ *LT)) and 300 K (high T orthorhombic phase (*$Pbca$ *HT)), taken with* $E_i = 712$ *meV (D),* $E_i = 62$ *meV (E) and* $E_i = 10$ *meV (F). The blue and red shaded area in D - F show the calculated phonon densities of states (PDOSs) without van der Waals (vdW) correction and with the vdW-DF2 correction, respectively. The inset in E shows the* $T_{NH_3-CH_2CH_2}$ *twisting mode, which corresponds to the phonon peak 3 and the calculated peaks labeled by the blue and red arrows. The magenta circles in (G - I) and yellow triangles in H represent the fitted Gaussian peak area A of the phonon peak 1 - 4, which are labeled in D - F, respectively. The fitted area A is normalized by the peak area of 10 K,* A_{10K}*. In G, the blue squares and red diamonds represent the T-dependent relaxation time* τ_{rot} *of the* C_3 *and* C_4 *rotational modes of BA*$^+$ *molecules,* τ_{C_3} *and* τ_{C_4}*, respectively, that were obtained from Figure 26 and Table 2. In H, the blue squares and red diamonds show the integrated intensity I of the phonon valley 5 (*$5 \leq \hbar\omega \leq 6$ *meV) and 6 (*$16 \leq \hbar\omega \leq 17$ *meV) labeled in E, which are normalized by the values at 10 K,* I_{10K}*. The blue squares, red diamonds and green triangles*

in I are the T-dependent charge carrier lifetimes, τ_1, τ_2 and τ_3, that were extracted from the TRPL data shown in Figure 22B and Table 8 (Appendix 2).

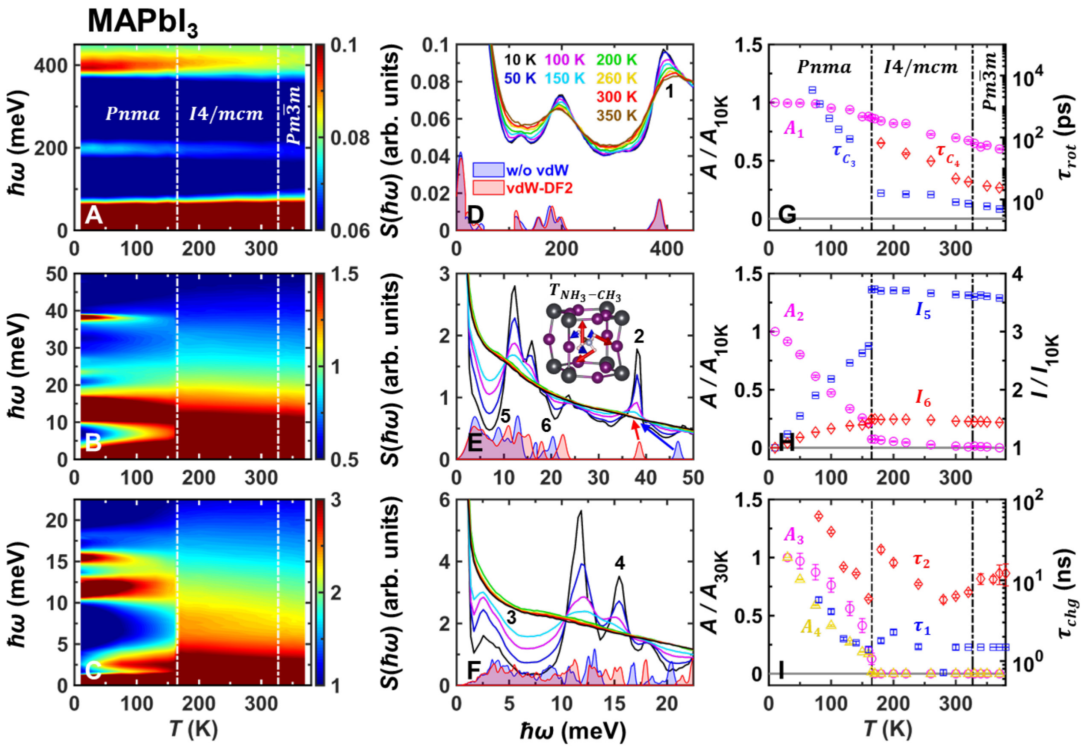

Figure 35.Temperature-Dependent Phonon Spectra of $MAPbI_3$.

(A - C) Color contour maps of Q-integrated neutron scattering intensity, $S(\hbar\omega)$, as a function of temperature T and energy transfer $\hbar\omega$, taken at 20 different temperatures while heating from 10 K to 370 K, with the incident neutron energy E_i of 600 meV (A), 60 meV (B) and 30 meV (C). (D - F) Plotted are the $S(\hbar\omega)$ for eight selected temperatures, 10 K, 50 K, 100 K, 150 K (orthorhombic phase ($Pnma$)), 200 K, 250 K, 300 K (tetragonal phase ($I4/mcm$)) and 350 K (cubic phase ($Pm\bar{3}m$)), taken with $E_i = 600$ meV (D), $E_i = 60$ meV (E) and $E_i = 30$ meV (F). The blue and red shaded area in D - F show the calculated PDOSs without vdW correction and with the vdW-DF2 correction, respectively. The inset in E shows the $T_{NH_3-CH_3}$ twisting mode, which corresponds to the phonon peak 2 and the calculated peaks marked by the blue and red arrows. The magenta circles in (G - I) and yellow triangles in I represent the fitted Gaussian peak area A of the phonon peak 1 - 4, which are labeled in D - F, respectively. The fitted area A is normalized by the peak area of 10 K, A_{10K} for G, H and 30 K, A_{30K} for I. In G, the blue squares and red diamonds represent the T-dependent relaxation time τ_{rot} of the C_3 and C_4 rotational modes of MA^+ molecules [58]. In H, the blue squares and red diamonds show the integrated intensity I of

the phonon valley 5 ($6 \leq \hbar\omega \leq 8\, meV$*) and 6 (*$20 \leq \hbar\omega \leq 22\, meV$*) labeled in E, which are normalized by the values at 10 K,* I_{10K}*. The blue squares and red diamonds in I are the* T*-dependent charge carrier lifetimes,* τ_1 *and* τ_2*, of MAPbI₃ [14], which were also shown in Figure 22E.*

Interestingly, the hybrid inorganic-organic phonon modes and the mostly-inorganic phonon modes weaken, i.e., phonons melt, gradually upon warming in the low temperature $Pbca$ LT phase (see A_3 (Figure 34H) and A_2 (Figure 34H), A_4 (Figure 34I), respectively). The melting becomes almost complete near the phase transition and completed as the system enters the $Pbca$ HT phase. As those phonons melt, a broad quasi-elastic peak appears up to ~ 40 meV and becomes stronger upon warming, most apparently at 300 K (see the red line in Figure 34E). This quasi-elastic signal is an indication of emergence of liquid-like vibrations upon heating. To study the T-dependence of the liquid-like vibrations, we have chosen the valley regions at $5 \leq \hbar\omega \leq 6$ meV (I_5) and $16 \leq \hbar\omega \leq 17$ meV (I_6) where coherent phonons are negligible at 10 K (see Figure 34E). As shown in Figure 34H, I_5 (blue squares) and I_6 (red diamonds) show a gradual increase as T increases and as coherent phonons melt.

As shown in Figure 35E, F and Figure 35H, I, similarly to $(BA)_2PbI_4$, $MAPbI_3$ also exhibits gradual phonon melting of all inorganic including the Pb-I-Pb bending and Pb-I stretching modes (2 meV $\lesssim \hbar\omega \lesssim$ 16 meV, for instance, A_3 and A_4 in Figure 35I) and hybrid phonon (A_2 in Figure 35H) modes in the low temperature orthorhombic phase (see Table 13 and Table 15 at Appendix 4 for the mode details). In the intermediate temperature tetragonal phase, those phonon modes are almost melted. To study the T-dependent liquid-like vibrations in $MAPbI_3$, we have again chosen the valley regions at $6 \leq \hbar\omega \leq 8$ meV (I_5) and $20 \leq \hbar\omega \leq 22$ meV (I_6) where coherent phonons are negligible at 10 K (see

Figure 35E). As shown in Figure 35H, I_5 (blue squares) and I_6 (red diamonds) show a gradual increase as T increases within the low-T orthorhombic phase. It should be noted that the low energy valley, I_5, shows a sudden increase at the orthorhombic-to-tetragonal phase transition at ~165 K, which can be explained by the huge changes in both rotational signal and liquid-like phonon signal. When $MAPbI_3$ enters the tetragonal phase from the orthorhombic phase, the relaxation time of the MA^+ C_3 rotation is significantly reduced from 70 ps (0.06 meV) to 1.59 ps (2.6 meV) [58], which will cause the increase of valley intensity, I_5, at $6 \leq \hbar\omega \leq 8$ meV. On the other hand, the change of the crystal structure at the phase transition may also lead to a prominent change of the liquid-like phonons at the valley I_5. The PL lifetimes (τ_1 and τ_2 in Figure 35I) of $MAPbI_3$ show a sudden jump at the orthorhombic-to-tetragonal phase transition, which coincides with the activation of MA^+ molecules' C_4 rotational mode (τ_{C_4} in Figure 35G) and the complete melting of coherent phonons.

6.3.3 Spatial Correlation in Phonon Melting

A question that naturally arises is what happens to the spatial coherence of the collective vibrations when the inorganic and hybrid phonons lose their coherence in time. To address this issue, we have plotted in Figure 36 the Q-dependences of $S(Q, \hbar\omega)$ for $(BA)_2PbI_4$ and $MAPbI_3$ at various temperatures, that are integrated over three different $\hbar\omega$ regions to cover Pb-I-Pb bending, Pb-I stretching, and organic-inorganic hybrid modes, up to $\hbar\omega \sim 20$ meV. Upon heating, all the resulting $S_{exp}(Q)$ exhibit a gradual shift to lower Q, which is due to the increasing vibrational amplitudes, i.e., increasing atomic displacement parameters.

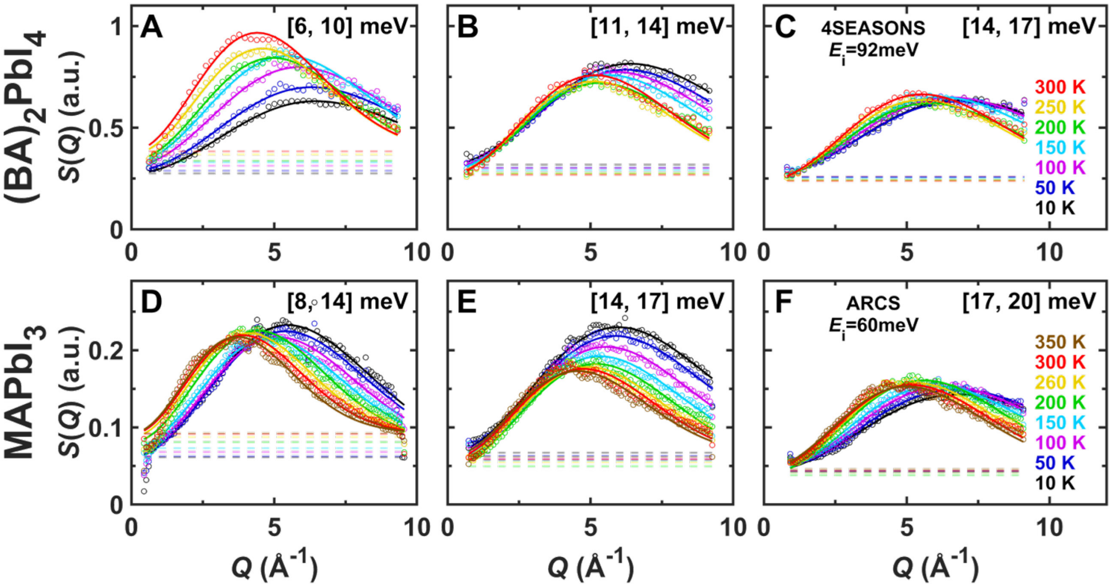

Figure 36. Q-Dependence of the Phonon Spectra for (BA)$_2$PbI$_4$ and MAPbI$_3$.

In (A - C), the colored circles show the $\hbar\omega$*-integrated neutron scattering intensity,* $S(Q)$*, as a function of temperature* T *and momentum transfer* Q*, taken on (BA)*$_2$*PbI*$_4$ *at 4SEASONS, at 7 different temperatures while heating from 10 K to 300 K, with the incident neutron energy* E_i *of 92 meV and the* $\hbar\omega$ *integration region of* $6 \leq \hbar\omega \leq 10$ *meV (A),* $11 \leq \hbar\omega \leq 14$ *meV (B) and* $14 \leq \hbar\omega \leq 17$ *meV (C) respectively. In (D - F), the colored circles show the* $S(Q)$ *of MAPbI*$_3$ *taken at ARCS, at 8 different temperatures while heating from 10 K to 350 K, with the incident neutron energy* E_i *of 60 meV and the* $\hbar\omega$ *integration region of* $8 \leq \hbar\omega \leq 14$ *meV (D) and* $14 \leq \hbar\omega \leq 17$ *meV (E) and* $17 \leq \hbar\omega \leq 20$ *meV (F), respectively. The experimental* $S(Q)$ *data in A - F were then fitted to* $S_{model}(Q) = aQ^2e^{-U_{iso}Q^2} + b$*, in which the total fitted* $S_{model}(Q)$*s and the background terms are shown as opaque solid lines and transparent dashed lines, respectively, with the same color as the corresponding experimental data.*

We have fitted the $S_{exp}(Q)$ to a phenomenological function for the collective phonons, $S_{model}(Q) = A \cdot Q^2e^{-U_{iso}Q^2} + B$, with an intensity factor, A, a constant background term, B, and an isotropic Debye-Waller factor, $e^{-U_{iso}Q^2}$. Shown as the solid lines in Figure 36, $S_{model}(Q)$ can reproduce the experimental $S_{exp}(Q)$ for all the three energy regions and all the temperatures, for both $(BA)_2PbI_4$ and $MAPbI_3$. Note that at low temperatures the vibrations are coherent in space and time. The fact that $S_{model}(Q)$ for coherent phonons at low temperatures can account for the Q-dependence of vibrations at high temperatures as well means that the vibrations at high temperatures are coherent in space even though the vibrational amplitude is much larger than at low temperatures. It is surprising that upon heating vibrational motions in these HOIPs lose coherence in time but maintain spatial coherence.

6.3.4 Phonon Spectrum Simulations

To investigate the origin of the phonon melting behaviors in both $(BA)_2PbI_4$ and $MAPbI_3$, we calculated the temperature dependent phonon spectrum for these two HOIP systems, using the third-party package, OCLIMAX [99] (see Section 2.4.2 for details). For comparison, the same simulations were also performed on a typical ionic crystal, NaCl, and a covalent crystal, SiO_2.

As shown in Figure 37, for the HOIPs and NaCl, upon heating, phonon peaks weaken rapidly and are eventually replaced by the quasi-elastic liquid-like vibrations over the entire energy spectrum. On the other hand, for SiO_2, the coherent phonons can survive at least up to 500 K. This different phonon melting behavior is probably related to the difference in the binding energies between these materials. Our DFT calculations show that the binding energy between nearest-neighboring atoms is ~ 3 eV for HOIPs (Pb-I and I-H bonds) and NaCl (Na-Cl bonds), indicating the weak ionic bonds in these two systems (see Table 18 at Appendix for details). On the other hand, for SiO_2, the Si-O bonds are covalent bonds, with a much stronger binding energy at ~ 10 eV.

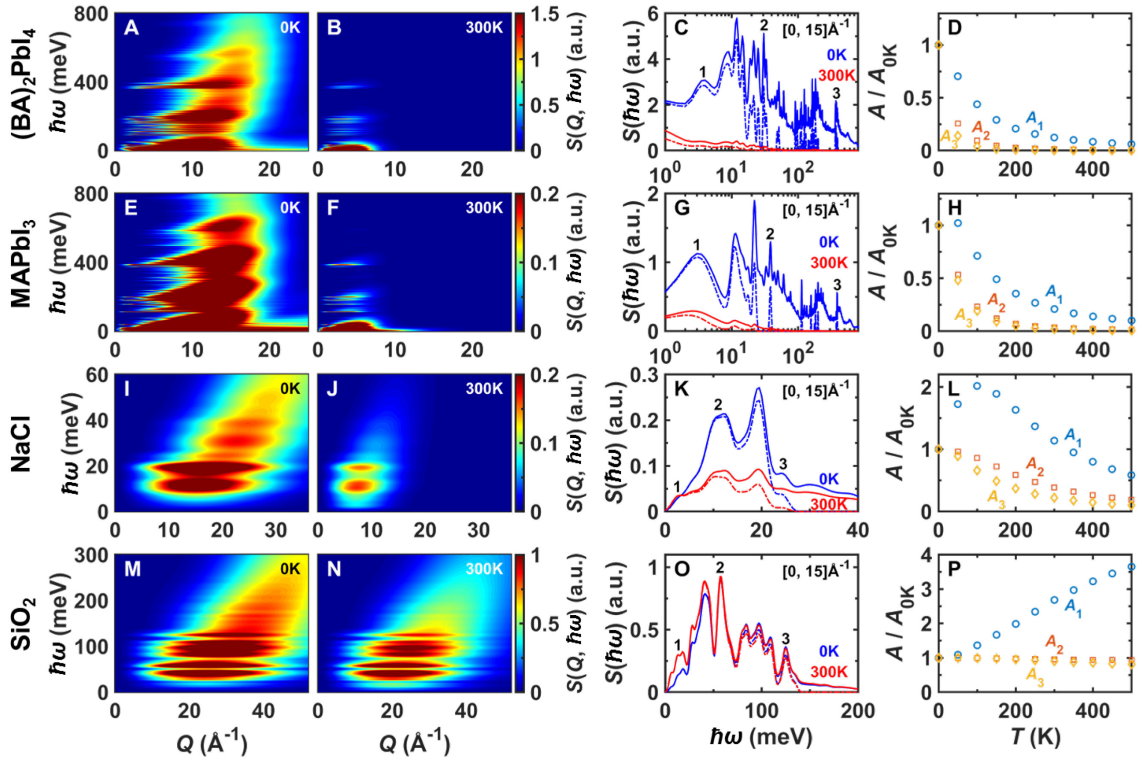

Figure 37.Simulated Phonon Spectra for (BA)$_2$PbI$_4$, MAPbI$_3$, NaCl and SiO$_2$.

(A, E, I, M) and (B, F, J, N) Contour maps of the simulated inelastic neutron spectra, $S(Q, \hbar\omega)$*, for (BA)*$_2$*PbI*$_4$*, MAPbI*$_3$*, NaCl, SiO*$_2$ *at 0 K and 300 K, respectively. The inelastic neutron spectra are calculated with a third-party package, OCLIMAX [99], considering phonon scatterings up to 10 phonon excitations. (C, G, K, O) The momentum transfer* Q*-integrated phonon spectra,* $S(\hbar\omega) = \int_0^{15\,\text{Å}^{-1}} S(Q, \hbar\omega)dQ$*, for (BA)*$_2$*PbI*$_4$*, MAPbI*$_3$*, NaCl, SiO*$_2$*. The blue and red solid lines in C, G, K, O represent total phonon spectra,* $S(\hbar\omega)$*, at 0 K and 300 K, while the dash-dotted lines are the corresponding single phonon contributions. (D, H, L, P) The fitted Gaussian peak areas, As, of the phonon peaks 1 - 3, which are labeled in C, G, K, O for (BA)*$_2$*PbI*$_4$*, MAPbI*$_3$*, NaCl, SiO*$_2$*, respectively. The fitted As are normalized by the peak area at 0 K,* A_{0K}*.*

The comparison between two HOIPs and NaCl, SiO$_2$ suggests that the gradual melting of coherent phonons observed in the two HOIPs is mainly due to the weak ionic bonds in the system. Upon heating, the vibrational amplitudes in weak ionic lattice should increase much faster than those in the covalent lattice, leading to a prominent phonon melting phenomenon. It should be noted that our simulations don't account for the phonon anharmonicity, which may further assist the phonon melting process [68, 69, 153].

6.4 Influence on Charge Carrier Dynamics

When the light is injected into the hybrid organic-inorganic perovskite (HOIP) materials, the charge carriers, i.e., electrons and holes, can be generated by absorbing the photon energy. The electrons and holes may travel freely as free carriers or form bound states as excitons. On the other hand, the free carriers can be shielded by the lattice polarization to form polarons.

Which state is dominant depends on several factors, e.g., the degree of quantum confinement and electrical polarizability. The stronger quantum confinement will lead to the formation of excitons, while more deformable lattice and the stronger electrical polarizability will lead to formation of polarons. This qualitatively explains the dominant excitonic features in 2D HOIPs evidenced by their extremely high exciton binding energy [51, 52, 134] and excellent light-emitting properties [154, 155], and the dominant polaronic features in 3D HOIPs evidenced by their long charge carrier lifetime, large diffusion length and modest carrier mobility [64, 147, 156, 157].

The polaronic properties of $MAPbI_3$ and excitonic properties of $(BA)_2PbI_4$ are also evidenced in the dielectric measurements. The 3D HOIPs have large high-frequency dielectric constants, e.g., $\epsilon_\infty = 23.3$ and 28.7 for $MAPbI_3$ and $MAPbBr_3$, respectively [130, 131]. In the case of 3D HOIPs, when the organic molecule is replaced by the inorganic atom, such as Cs, the dielectric constant will be reduced, e.g., $\epsilon_\infty \approx 5.26$ for

$CsPbBr_3$. This implies the important role of the molecular rotations in the electronic properties of the 3D HOIPs, which is also consistent with the previous study that reported the intimate coupling between the dielectric response and a particular rotational mode of $MAPbI_3$ as a function of temperature [58, 130]. On the other hand, the 2D HOIPs have much smaller dielectric constants, e.g., $\epsilon_\infty \approx 2.1 \sim 4.0$ for $(BA)_2PbI_4$ [52, 133], which is consistent with the excitonic nature of $(BA)_2PbI_4$.

The all-inorganic 3D metal halide perovskites (MHPs), e.g., $CsPbBr_3$, have been shown to exhibit polaronic features as well [69, 105, 107]. However, the differences in polaronic strength and properties in all-inorganic 3D MHPs and 3D HOIPs are still not well understood. The appearance of polarons in all-inorganic 3D MHPs suggests an important role of inorganic vibrational modes in polaron formation [69, 105, 107]. The fact that the 3D HOIPs have higher dielectric constants than the all-inorganic 3D MHPs indicates that the rotational dynamics of the organic molecules can further enhance the polaronic features in these systems. This is consistent with a recent theoretical study based on the tight-binding model and DFT calculations, which reported the polaron binding energy increases to 55 meV when molecular dynamic disorder is added into the calculation, compared to a much smaller value of 12 meV when only the electron-phonon coupling is considered [107].

In this thesis, what we find is that the charge carrier lifetimes of the 3D HOIP, $MAPbI_3$, τ_1 (0.7 ~ 5.7 ns) and τ_2 (6 ~ 60 ns) exhibit significant increase when the liquid-like vibrations of inorganic atoms become prevalent and a particular C_4 rotational mode of the MA^+ molecule gets activated. On the other hand, for the 2D HOIP, $(BA)_2PbI_4$, which is dominated by excitons, does not show prominent correlations between phonon melting, molecular rotation and the lifetime of *majority* charge carriers.

Chapter 7.

Summary

In summary, this thesis thoroughly studied the temperature-dependent crystal structures, rotational, vibrational dynamics, and optoelectronic properties of a two-dimensional (2D) hybrid organic-inorganic perovskite (HOIP), $(BA)_2PbI_4$, i.e., $(C_4H_9NH_3)_2PbI_4$.

Firstly, in the neutron diffraction study, we obtained the refined crystal structures, especially for the organic BA^+ cations, in both the orthorhombic low-temperature ($Pbca$ LT) phase and orthorhombic high-temperature ($Pbca$ HT) phase of $(BA)_2PbI_4$. The changes in the lattice constants, internal atomic and molecular structures, especially for the orientation of BA^+ molecules, were observed during the structural phase transition, at 279(1) K upon heating and 257(1) K upon cooling.

Secondly, in the photoluminescence measurements for $(BA)_2PbI_4$, we observed two short and nearly temperature-independent charge carrier lifetimes, $\tau_1 \sim 0.1 - 0.3$ ns and $\tau_2 \sim 0.4 - 1.1$ ns, for the *majority* charge carriers, which is in contrast with the three-dimensional (3D) HOIP, $MAPbI_3$. In $MAPbI_3$, the *majority* charge carriers' lifetimes are approximately an order of magnitude longer than the those in $(BA)_2PbI_4$, i.e., $\tau_1 \sim 0.7 - 5.7$ ns and $\tau_2 \sim 6 - 60$ ns in $MAPbI_3$, which shows a gradual decrease within each structural phase, while exhibits a significant increase at the orthorhombic-to-tetragonal phase transition. The short, temperature-independent and long, temperature-dependent charge carrier lifetimes are consistent with the *majority* excitons and *majority* polarons in 2D and 3D HOIPs, respectively.

Thirdly, with the quasi-elastic neutron scattering measurements and group theoretical analysis, we have identified the rotational modes of BA^+ cations in $(BA)_2PbI_4$. Two different types of jump rotational modes were found: the C_3 modes of the terminal NH_3, CH_3 groups with a smaller rotational radius and shorter relaxation time, which exist in both the $Pbca$ LT and $Pbca$ HT phases; and the C_4 mode of the whole BA^+ molecule with a larger rotational radius and longer relaxation time, which is only activated in the $Pbca$ HT phase. The C_4 mode appears right after the phase transition at ~ 280 K, showing a characteristic relaxation time of 53(7) ps. The rotational modes of $(BA)_2PbI_4$ show similarities to those of the 3D HOIP, $MAPbI_3$, especially for the appearance of the C_4 rotational mode in the high-temperature phases.

Moreover, we studied the vibrational dynamics of $(BA)_2PbI_4$ and $MAPbI_3$ using the inelastic neutron scatterings and density-functional theory (DFT) calculations. We discovered the importance of van der Waals (vdW) interactions in both systems, especially the vdW interactions between the organic molecule BA^+, MA^+ and the nearby inorganic framework $[PbI_4]^{2-}$, $[PbI_3]^-$. With a specific vdW correction functional, vdW-DF2, applied to the DFT calculations, we were able to reproduce the phonon spectra of $(BA)_2PbI_4$ and $MAPbI_3$ for the first time. In particular, the vdW correction has significant influence (inducing ~ 20% phonon energy changes) on the phonon mode involving the NH_3 twisting, i.e., $T_{NH_3-CH_2CH_2}$ for $(BA)_2PbI_4$ and $T_{NH_3-CH_3}$ for $MAPbI_3$. And we observed the phonon melting features on both 2D and 3D HOIPs, when the phonon modes gradually lose their time coherences as the temperature increases, while the spatial correlations are still conserved. Most prominently, the mostly-inorganic and hybrid modes become featureless continuums within the low-temperature phases, i.e., the $Pbca$ LT phase for $(BA)_2PbI_4$ and the orthorhombic $Pnma$ phase for $MAPbI_3$.

Comparing the charge carrier dynamics with the rotational and vibrational dynamics, we conclude that the 2D HOIP, $(BA)_2PbI_4$, which is dominated by excitons, does not show correlations between PL lifetime and rotational dynamics, phonon melting. On the other hand, in the 3D HOIP where polaronic feature is prominent, the major factors which enhance the charge carrier lifetime are both the rotations of the MA^+ molecules and the liquid-like vibrations of the inorganic atoms.

Appendix 1.

Crystal Structural Parameters

The crystal structural parameters listed in this appendix are for $(BA)_2PbI_4$ high T orthorhombic ($Pbca$ HT) phase at 350 K (Table 4), low T orthorhombic ($Pbca$ LT) phase at 200 K (Table 5) and 13 K (Table 6).

Table 4. Crystal Structural Parameters of $(BA)_2PbI_4$ $Pbca$ HT Phase at 350 K.

Label	Atom	x	y	z	Occ.	U_{iso} (Å^2)	Site
Pb	Pb	0.00000	0.00000	0.00000	1	0.065	4a
I1	I	0.03900	0.03958	0.89381	1	0.153	8c
I2	I	0.70943	0.24860	0.00359	1	0.153	8c
N	N	0.10681	0.54630	0.91191	1	0.223	8c
HA	H	0.08294	0.57525	0.94160	1	0.112	8c
HB	H	0.15523	0.62219	0.89723	1	0.112	8c
HC	H	0.16530	0.46369	0.91316	1	0.112	8c
C1	C	0.97202	0.51026	0.88554	1	0.429	8c
D1A	D	0.90299	0.59570	0.88774	1	0.477	8c
D1B	D	0.92455	0.42105	0.89982	1	0.477	8c
C2	C	0.00620	0.47840	0.83407	1	0.429	8c
D2A	D	0.07350	0.39116	0.83163	1	0.477	8c
D2B	D	0.05521	0.56662	0.81981	1	0.477	8c
C3	C	0.86155	0.44346	0.80701	1	0.429	8c
D3A	D	0.80711	0.36344	0.82361	1	0.477	8c
D3B	D	0.79919	0.53491	0.80658	1	0.477	8c
C4	C	0.89136	0.39435	0.75726	1	0.501	8c
D4A	D	0.79783	0.37432	0.74123	1	0.800	8c
D4B	D	0.95080	0.30307	0.75748	1	0.800	8c
D4C	D	0.94359	0.47453	0.74048	1	0.800	8c

Lattice constants, atomic positions and occupancies per unit cell of $(BA)_2PbI_4$ were determined at 350 K (high T orthorhombic ($Pbca$ HT) phase) using Rietveld refinement of the neutron diffraction data shown in Figure 20A. The lattice constants are $a = 8.9348(5)$ Å, $b = 8.7098(5)$ Å, $c = 27.8420(16)$ Å. *The goodness of the refinement is* $\chi^2 = 1.310$.

Table 5. Crystal Structural Parameters of $(BA)_2PbI_4$ $Pbca$ LT Phase at 200 K.

Label	Atom	x	y	z	Occ.	U_{iso} (Å^2)	Site
Pb	Pb	0.00000	0.00000	0.00000	1	0.003	4a
I1	I	0.07337	0.01502	0.88604	1	0.031	8c
I2	I	0.69031	0.20307	0.97549	1	0.031	8c
N	N	0.02158	0.42516	0.90389	1	0.006	8c
HA	H	0.02474	0.33098	0.91524	1	0.067	8c
HB	H	0.01126	0.49284	0.92883	1	0.067	8c
HC	H	0.12329	0.44470	0.89638	1	0.067	8c
C1	C	0.92329	0.44253	0.86050	1	0.049	8c
D1A	D	0.81197	0.45446	0.86998	1	0.045	8c
D1B	D	0.92099	0.36262	0.83522	1	0.045	8c
C2	C	0.96075	0.58862	0.83283	1	0.049	8c
D2A	D	0.06036	0.58718	0.81381	1	0.045	8c
D2B	D	0.93565	0.66886	0.85667	1	0.045	8c
C3	C	0.85049	0.62345	0.78700	1	0.049	8c
D3A	D	0.85053	0.53890	0.76352	1	0.045	8c
D3B	D	0.74093	0.61355	0.79863	1	0.045	8c
C4	C	0.89443	0.76099	0.75821	1	0.100	8c
D4A	D	0.83452	0.77459	0.72708	1	0.068	8c
D4B	D	0.99467	0.75486	0.74038	1	0.068	8c
D4C	D	0.89296	0.84143	0.78273	1	0.068	8c

Lattice constants, atomic positions and occupancies per unit cell of $(BA)_2PbI_4$ were determined at 200 K (low T orthorhombic ($Pbca$ LT) phase) using Rietveld analysis of the neutron diffraction data shown in Figure 20B. The lattice constants are $a = 8.4625(4)$ Å, $b = 9.0181(4)$ Å, $c = 26.2996(10)$ Å. *The goodness of the refinement is* $\chi^2 = 1.658$.

Table 6. Crystal Structural Parameters of $(BA)_2PbI_4$ $Pbca$ LT Phase at 13 K.

Label	Atom	x	y	z	Occ.	U_{iso} (Å^2)	Site
Pb	Pb	0.00000	0.00000	0.00000	1	0.000	4a
I1	I	0.07138	0.02532	0.88426	1	0.000	8c
I2	I	0.69359	0.20496	0.97315	1	0.000	8c
N	N	0.00916	0.42302	0.90231	1	0.001	8c
HA	H	0.00418	0.30728	0.91635	1	0.007	8c
HB	H	0.97864	0.49166	0.93157	1	0.007	8c
HC	H	0.15696	0.44181	0.89204	1	0.007	8c
C1	C	0.90950	0.44326	0.85889	1	0.000	8c
D1A	D	0.78977	0.45815	0.87306	1	0.010	8c
D1B	D	0.92236	0.36106	0.83203	1	0.010	8c
C2	C	0.95277	0.59524	0.82994	1	0.000	8c
D2A	D	0.07274	0.58826	0.81554	1	0.010	8c
D2B	D	0.94516	0.67739	0.85947	1	0.010	8c
C3	C	0.84791	0.61900	0.78566	1	0.000	8c
D3A	D	0.85532	0.53403	0.75647	1	0.010	8c
D3B	D	0.73513	0.61965	0.79751	1	0.010	8c
C4	C	0.88714	0.77316	0.75451	1	0.019	8c
D4A	D	0.81803	0.78672	0.72390	1	0.014	8c
D4B	D	0.00651	0.76189	0.74086	1	0.014	8c
D4C	D	0.87271	0.85134	0.78572	1	0.014	8c

Lattice constants, atomic positions and occupancies per unit cell of $(BA)_2PbI_4$ *were determined at 13 K (low* T *orthorhombic (*$Pbca$ *LT) phase) using Rietveld analysis of the neutron diffraction data shown in Figure 20C. The lattice constants are* $a = 8.4141(3)$ Å, $b = 8.9779(2)$ Å, $c = 25.9452(8)$ Å. *The goodness of the refinement is* $\chi^2 = 1.620$.

Appendix 2.

Details of Time-Resolved Photoluminescence Measurements

This appendix shows the details of the time-resolved photoluminescence (TRPL) measurements on $(BA)_2PbI_4$, including the experimental setting table (Table 7), the contour map of the temperature-dependent TRPL spectra (Figure 38), and the fitted TRPL parameters (Table 8).

Table 7. Experimental Settings for Time-Resolved Photoluminescence (TRPL) Measurements on $(BA)_2PbI_4$.

T (K)	λ (nm)	Integration Time (s)
80	487	22
100	487	22
120	488	23
140	489	27
160	490	30
180	491	30
200	491	30
220	493	30
240	494	30
260	495	30
270	521	30
280	521	60
290	521	60
300	521	60

The central wavelength (λ) of the detection window and detector integration time for the TRPL measurements at 14 different temperatures from 80 to 300 K during heating.

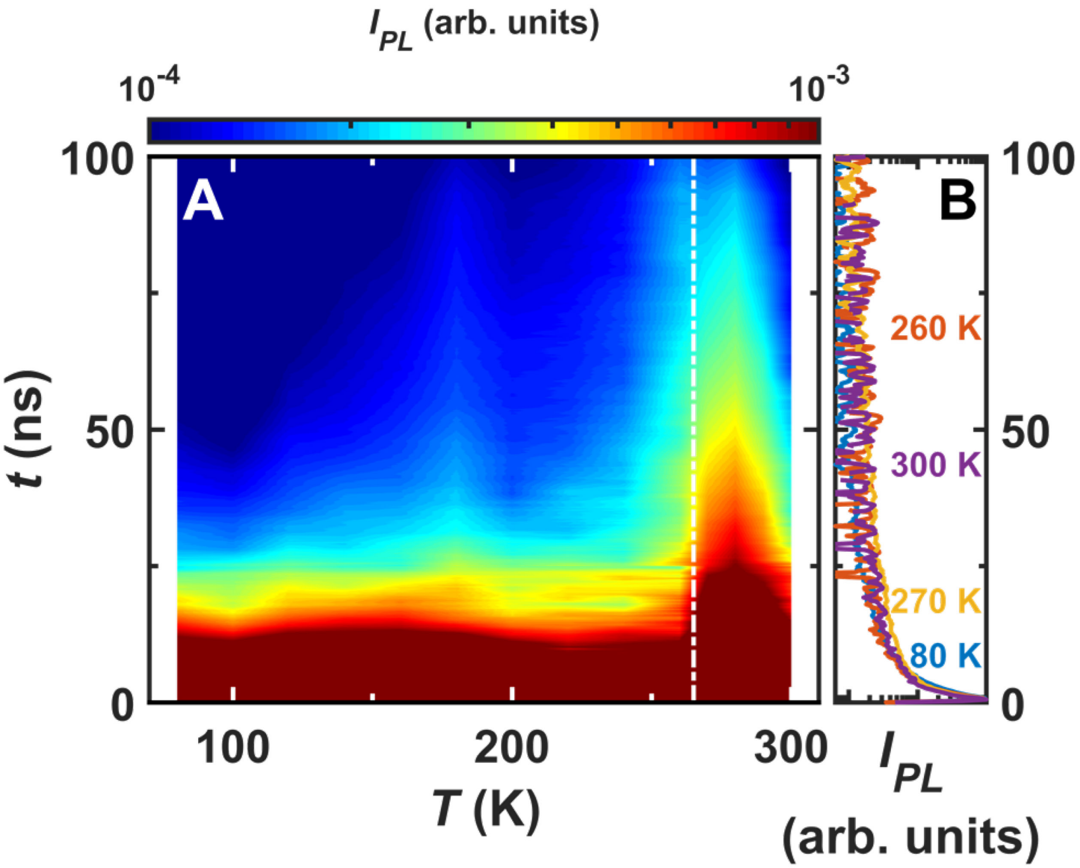

Figure 38.Time-Resolved Photoluminescence Spectra of $(BA)_2PbI_4$.

(A) shows the color contour map of the normalized time-resolved photoluminescence intensity, $I_{PL}(T,t)$, as a function of the temperature T and delay time t. (B) shows the 1D plot of $I_{PL}(t)$ at four different temperatures: 80 K and 260 K in the low T orthorhombic ($Pbca$ LT) phase, and 270 and 300 K in the high T orthorhombic ($Pbca$ HT) phase. The vertical dash-dotted line in A represents the structural transition temperature.

Table 8. Fitted TRPL Parameters for $(BA)_2PbI_4$.

T (K)	A_1 (cnts)	τ_1 (ns)	A_2 (cnts)	τ_2 (ns)	A_3 (cnts)	τ_3 (ns)	$Bkgr._{Dec}$ (cnts)	$Bkgr._{IRF}$ (cnts)	$Shift_{IRF}$ (ns)
80	220 (40)	6.7 (7)	14300 (700)	0.94 (3)	96000 (3000)	0.253 (7)	2.7 (3)	8.6	2.385 (5)
100	170 (30)	7.2 (9)	14500 (700)	0.89 (3)	104000 (3000)	0.228 (6)	2.6 (3)	8.6	2.390 (5)
120	240 (40)	6.8 (7)	15000 (600)	1.08 (3)	88000 (3000)	0.278 (8)	2.9 (3)	8.6	2.389 (6)
140	340 (50)	5.8 (6)	18500 (700)	1.05 (3)	81000 (3000)	0.279 (9)	3.5 (4)	8.6	2.390 (6)
160	230 (40)	6.9 (8)	17300 (700)	1.08 (3)	70000 (2000)	0.30 (1)	4.0 (4)	8.6	2.387 (6)
180	200 (40)	6.1 (9)	15800 (600)	0.99 (3)	51000 (2000)	0.28 (1)	3.9 (4)	8.6	2.388 (7)
200	100 (30)	7 (1)	12200 (600)	0.90 (3)	44000 (2000)	0.27 (1)	3.7 (4)	8.6	2.396 (7)
220	30 (20)	11 (4)	7700 (500)	0.91 (4)	31000 (2000)	0.29 (1)	3.6 (3)	8.6	2.385 (9)
240	40 (20)	8 (3)	6000 (500)	0.71 (4)	25000 (1000)	0.24 (1)	3.5 (3)	8.6	2.39 (1)
260	50 (30)	5 (2)	3400 (400)	0.59 (5)	15000 (1000)	0.20 (2)	3.5 (3)	8.6	2.39 (1)
270	120 (20)	14 (2)	3200 (400)	1.08 (8)	77000 (3000)	0.194 (6)	3.7 (4)	8.6	2.355 (7)
280	190 (20)	13 (1)	4800 (500)	0.99 (6)	108000 (4000)	0.165 (5)	8.1 (5)	8.6	2.363 (6)
290	140 (20)	10 (2)	3600 (400)	0.82 (7)	78000 (4000)	0.138 (5)	7.8 (5)	8.6	2.354 (8)
300	110 (30)	5 (1)	5300 (700)	0.43 (4)	60000 (4000)	0.087 (5)	7.7 (5)	8.6	2.364 (9)

Results of the fitting of the TRPL data of $(BA)_2PbI_4$ to the (Eq. 21). The numbers in the parenthesis represent the standard error for the corresponding fitting parameters.

Appendix 3.

Details of Rotational Modes

This appendix shows the details of the rotational model calculations of $(BA)_2PbI_4$, which contains the character tables for point group C_4, C_3, C_2 (Table 9), and τ_γ, $A_\gamma(Q)$ for $\Gamma = C_4 \otimes C_3$ (Table 10), $\Gamma = C_4 \otimes C_2$ (Table 11). The rotational energy landscapes are also shown for the C_4 (Figure 39), C_3 (Figure 40), and C_2 modes (Figure 41).

Table 9. Character Tables for Point Group C_4, C_3 and C_2.

$C = C_4$	E	$2C_4$	C_2
A	1	1	1
B	1	-1	1
E	2	0	-2

$M = C_3$	E	$2C_3$
A	1	1
E	2	-1

$M = C_2$	E	C_2
A	1	1
B	1	-1

The point group C_4 has three irreducible representations and three classes: two one-dimensional representations, A and B, and one two-dimensional representation, E. The point group C_3 has two irreducible representations and two classes: one one-dimensional representation, A, and one two-dimensional representation E. The point group C_2 has two one-dimensional irreducible representations and two classes, A and B.

Table 10. Model Details for Jump Mode $\Gamma = C_4 \otimes C_3$.

Γ_γ	$\frac{1}{\tau_\gamma}$	$36 \cdot A_\gamma(Q)$
$A \otimes A$	0	$3 + 6j_1 + 2j_2 + 2j_3 + 2j_4 + 1j_5 + 2j_6 + 2j_7 + 2j_8 + 2j_9$ $+2j_{10} + 2j_{11} + 1j_{12} + 2j_{13} + 2j_{14} + 2j_{15} + 1j_{16}$
$A \otimes E$	$\frac{3}{\tau_{C_3}}$	$6 - 6j_1 + 4j_2 - 2j_3 - 2j_4 + 2j_5 - 2j_6 - 2j_7 - 2j_8 - 2j_9$ $+4j_{10} - 2j_{11} + 2j_{12} - 2j_{13} - 2j_{14} + 4j_{15} + 2j_{16}$
$B \otimes A$	$\frac{4}{\tau_{C_4}}$	$3 + 6j_1 - 2j_2 - 2j_3 - 2j_4 + 1j_5 + 2j_6 + 2j_7 - 2j_8 - 2j_9$ $-2j_{10} - 2j_{11} + 1j_{12} + 2j_{13} - 2j_{14} - 2j_{15} + 1j_{16}$
$B \otimes E$	$\frac{4}{\tau_{C_4}} + \frac{3}{\tau_{C_3}}$	$6 - 6j_1 - 4j_2 + 2j_3 + 2j_4 + 2j_5 - 2j_6 - 2j_7 + 2j_8 + 2j_9$ $-4j_{10} + 2j_{11} + 2j_{12} - 2j_{13} + 2j_{14} - 4j_{15} + 2j_{16}$
$E \otimes A$	$\frac{2}{\tau_{C_4}}$	$6 + 12j_1 - 2j_5 - 4j_6 - 4j_7 - 2j_{12} - 4j_{13} - 2j_{16}$
$E \otimes E$	$\frac{2}{\tau_{C_4}} + \frac{3}{\tau_{C_3}}$	$12 - 12j_1 - 4j_5 + 4j_6 + 4j_7 - 4j_{12} + 4j_{13} - 4j_{16}$

This model applies to the rotational modes of NH_3 *and* CH_3 *in (BA)*$_2$*PbI*$_4$*:* $S^{NH_3}_{C_4\otimes C_3}(Q,\hbar\omega) = 3\sum_\gamma A^{NH_3}_\gamma(Q)\frac{1}{\pi}\frac{\tau_\gamma}{1+\omega^2{\tau_\gamma}^2}$*, and* $S^{CH_3}_{C_4\otimes C_3}(Q,\hbar\omega) = 3\sum_\gamma A^{CH_3}_\gamma(Q)\frac{1}{\pi}\frac{\tau_\gamma}{1+\omega^2{\tau_\gamma}^2}$*, where the factor 3 comes from the three H atoms in the NH*$_3$ *or the CH*$_3$ *group. As shown in (Eq. 13),* $A^{NH_3}_\gamma(Q)$ *and* $A^{CH_3}_\gamma(Q)$ *can be written in terms of* j_i *that is the zeroth spherical Bessel function* $j_0(Qr_i)$*.* r_i *are the jump distances,* $r_1 = R_{1,2}$*,* $r_2 = R_{1,4}$*,* $r_3 = R_{1,5}$*,* $r_4 = R_{1,6}$*,* $r_5 = R_{1,7}$*,* $r_6 = R_{1,8}$*,* $r_7 = R_{1,9}$*,* $r_8 = R_{1,11}$*,* $r_9 = R_{1,12}$*,* $r_{10} = R_{2,5}$*,* $r_{11} = R_{2,6}$*,* $r_{12} = R_{2,8}$*,* $r_{13} = R_{2,9}$*,* $r_{14} = R_{2,12}$*,* $r_{15} = R_{3,6}$*,* $r_{16} = R_{3,9}$*. Here* $R_{i,j} = |R_i - R_j|$*, where* R_i *is the position of the* i*-th H site. The 12 H sites (*$i = 1{\sim}12$*) of the NH*$_3$ *group are labeled in Figure 24C.* τ_γ *is the relaxation time for the rotational mode of the irreducible representation* Γ_γ*.*

Table 11. Model Details for Jump Mode $\Gamma = C_4 \otimes C_2$.

Γ_γ	$\frac{1}{\tau_\gamma}$	$16 \cdot A_\gamma(Q)$
$A \otimes A$	0	$2 + 2j_1 + 2j_2 + 2j_3 + 1j_4 + 2j_5 + 2j_6 + 2j_7 + 1j_8$
$A \otimes B$	$\frac{2}{\tau_{C_2}}$	$2 - 2j_1 + 2j_2 - 2j_3 + 1j_4 - 2j_5 - 2j_6 + 2j_7 + 1j_8$
$B \otimes A$	$\frac{4}{\tau_{C_4}}$	$2 + 2j_1 - 2j_2 - 2j_3 + 1j_4 + 2j_5 - 2j_6 - 2j_7 + 1j_8$
$B \otimes B$	$\frac{4}{\tau_{C_4}} + \frac{2}{\tau_{C_2}}$	$2 - 2j_1 - 2j_2 + 2j_3 + 1j_4 - 2j_5 + 2j_6 - 2j_7 + 1j_8$
$E \otimes A$	$\frac{2}{\tau_{C_4}}$	$4 + 4j_1 - 2j_4 - 4j_5 - 2j_8$
$E \otimes B$	$\frac{2}{\tau_{C_4}} + \frac{2}{\tau_{C_2}}$	$4 - 4j_1 - 2j_4 + 4j_5 - 2j_8$

This model applies to the rotational modes of CH_2 *in (BA)*$_2$*PbI*$_4$*:* $S_{C_4 \otimes C_2}^{CH_2CH_2CH_2}(Q, \hbar\omega) = 2\sum_\gamma \sum_n A_\gamma^{CH_2[n]}(Q) \frac{1}{\pi} \frac{\tau_\gamma}{1+\omega^2 {\tau_\gamma}^2}$*, where the factor 2 comes from the two H atoms in each* CH_2 *group.* $A_\gamma^{CH_2[n]}(Q)$ *can be written in terms of* j_i *that is the zeroth spherical Bessel function* $j_0(Qr_i)$ *with the jump distances,* $r_1 = R_{1,2}$, $r_2 = R_{1,3}$, $r_3 = R_{1,4}$, $r_4 = R_{1,5}$, $r_5 = R_{1,6}$, $r_6 = R_{1,8}$, $r_7 = R_{2,4}$, $r_8 = R_{2,6}$*. Here* $R_{i,j} = |R_i - R_j|$*, where* R_i *is the position of the* i*-th H site. The 8 H sites (*$i = 1 \sim 8$*) of the* $CH_2[3]$ *group are labeled in Figure 24D.* τ_γ *is the relaxation time for the rotational mode of the irreducible representation* Γ_γ*.*

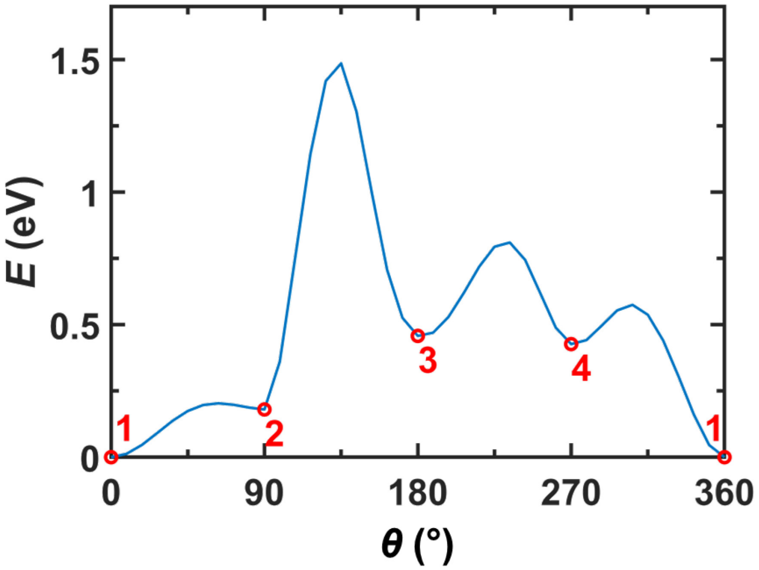

Figure 39.Rotational Energy Landscape for C_4 Mode.

The rotational energy landscape for C_4 *mode was simulated by DFT calculations on the BA*$^+$ *molecule in the orthorhombic high* T *(Pbca HT) phase. The blue line shows the total electronic energy,* E*, as a function of the rotation angle,* θ*; the red circles labeled as number 1, 2, 3, 4 represent four local minima located at the* C_4 *symmetry points, i.e.,* $\theta = 0, \frac{\pi}{2}, \pi, \frac{3\pi}{2}$*. The rotational energy barrier of* C_4 *mode is defined as the average barrier for all the possible jumps:* $1 \rightarrow 2, 2 \rightarrow 1, 2 \rightarrow 3, 3 \rightarrow 2, 3 \rightarrow 4, 4 \rightarrow 3, 4 \rightarrow 1, 1 \rightarrow 4$ *, i.e.,* $\frac{1}{4}\sum_{i=0}^{3}\left[\max_{i\frac{\pi}{2} \leq \theta \leq (i+1)\frac{\pi}{2}} E(\theta) - E\left(\theta = i\frac{\pi}{2}\right)\right]$.

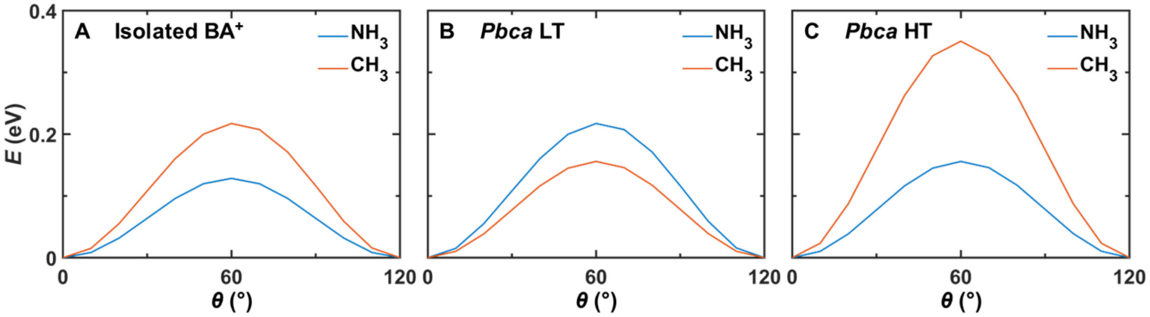

Figure 40.Rotational Energy Landscape for C_3 Mode.

The rotational energy landscapes for C_3 *mode were simulated by DFT calculations. (A - C) shows the rotational energy landscapes for isolated BA*$^+$ *molecule (A), BA*$^+$ *molecule in the orthorhombic low* T *(Pbca LT) phase (B) and BA*$^+$ *molecule in the orthorhombic high* T *(Pbca HT) phase (C). The blue and red lines show the total electronic energy,* E*, as a function of the rotation angle,* θ *for* $C_3^{NH_3}$ *and* $C_3^{CH_3}$ *mode, respectively. The rotational energy barrier of each mode is defined as* $\max\limits_{0\le\theta\le\frac{2\pi}{3}} E(\theta) - E(\theta = 0)$.

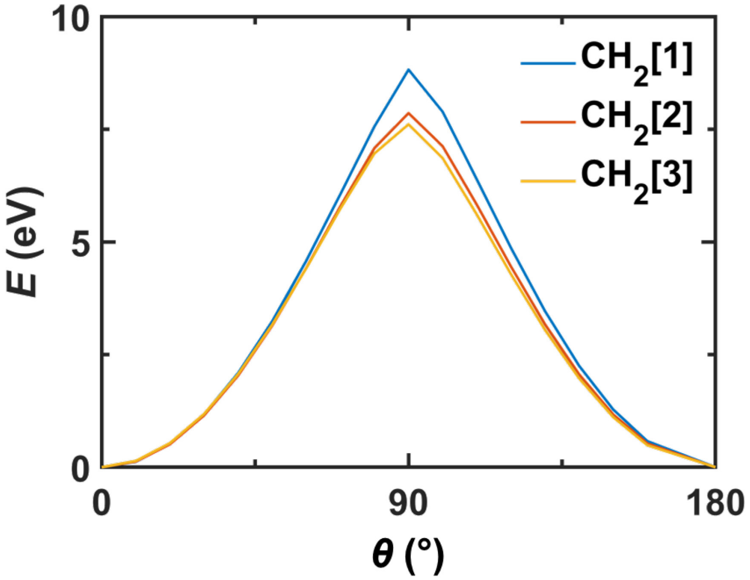

Figure 41.Rotational Energy Landscape for C_2 Mode.

The rotational energy landscapes for C_2 mode were simulated by DFT calculations on the isolated BA^+ molecule. The blue, red and yellow lines show the total electronic energy, E, as a function of the rotation angle, θ for $C_3^{CH_2[1]}$, $C_3^{CH_2[2]}$ and $C_3^{CH_2[3]}$ mode, respectively. The rotational energy barrier of each mode is defined as $\max_{0\leq\theta\leq\pi} E(\theta) - E(\theta = 0)$.

Appendix 4.

Details of Vibrational Modes

This appendix shows the phonon energies for selected vibrational modes of $(BA)_2PbI_4$ (Table 12) and $MAPbI_3$ (Table 13), the Pb-I-Pb bending and Pb-I stretching modes of $(BA)_2PbI_4$ (Table 14) and $MAPbI_3$ (Table 15), electronic interactions estimated for $(BA)_2PbI_4$ (Table 16) and $MAPbI_3$ (Table 17), phonon band structures of $(BA)_2PbI_4$ and $MAPbI_3$ (Figure 42), comparison between vdW correction functionals for $(BA)_2PbI_4$ (Figure 43) and $MAPbI_3$ (Figure 44), and the chemical bonds in both hybrid organic-inorganic perovskites (HOIPs), compared to NaCl and SiO_2 (Table 18).

Table 12. Selected Vibrational Mode Energies of $(BA)_2PbI_4$.

Phonon Mode	Calculated Phonon Energy (meV)						Experimental Peak Position (meV)
	Isolated BA^+		$(BA)_2PbI_4$				
	vdW-DF2		w/o vdW		vdW-DF2		
	$\hbar\omega_{avg}^{calc}$	$\Delta\hbar\omega$	$\hbar\omega_{avg}^{calc}$	$\Delta\hbar\omega$	$\hbar\omega_{avg}^{calc}$	$\Delta\hbar\omega$	$\hbar\omega_{exp}$
$8T_{NH_3CH_2CH_2-CH_2CH_3}$	13.1	5.4	18.5(6)	0.0	19.3(6)	0.8	18.5(1)
$8T_{NH_3CH_2-CH_2CH_2CH_3}$	13.5	8.1	21.2(5)	0.4	21.7(7)	0.1	21.6(1)
$8B_{NH_3CH_2-CH_2-CH_2CH_3}^{S}$	21.5	3.9	25.3(3)	0.1	25.4(2)	0.0	25.4(1)
$8T_{NH_3-CH_2CH_2}$	26.5	3.2	38.2(1)	8.5	30.6(2)	0.9	29.7(1)
$8T_{CH_2CH_2-CH_3}$	30.1	3.1	32.7(6)	0.5	33.4(5)	0.2	33.2(1)
$8S_{NH_3CH_2-CH_2-CH_2CH_3}$	46.4	4.0	49.2(4)	1.2	48.8(3)	1.6	50.4(1)
$8B_{NH_3CH_2-CH_2-CH_2CH_3}^{A}$	48.4	3.9	51.3(2)	1.0	51.6(3)	0.7	52.3(1)
$8T_{CH_2-CH_2-CH_2-CH_3}$	92.0	0.1	89.6(2)	2.5	91.3(2)	0.8	92.1(1)

Eigen energies of the vibrational modes of $(BA)_2PbI_4$ *in the* $Pbca$ *LT phase that are labelled as 1 - 8 in Figure 28 were calculated using two settings: PBE functional without vdW correction and with vdW-DF2 correction. Corresponding phonon energies for the isolated* BA^+ *molecule were also calculated for comparison. All calculations were performed at the* Γ *point* ($\boldsymbol{q} = (0, 0, 0)$)*. The eight phonon modes are the following: (1)* $T_{NH_3CH_2CH_2-CH_2CH_3}$ *that is an antisymmetric twisting mode of the two parts,* $NH_3CH_2CH_2$ *and* CH_2CH_3*, (2)* $T_{NH_3CH_2-CH_2CH_2CH_3}$ *that is a twisting mode of* NH_3CH_2 *and* $CH_2CH_2CH_3$*, (3)* $B_{NH_3CH_2-CH_2-CH_2CH_3}^{S}$ *that is a symmetric bending mode in which* NH_3CH_2 *and* CH_2CH_3 *at the two ends of the molecule bend symmetrically, pushing the* CH_2 *at the center in and out, (4)* $T_{NH_3-CH_2CH_2}$ *that is an antisymmetric twisting mode of mainly* NH_3 *and its neighboring* CH_2CH_2*, (5)* $T_{CH_2CH_2-CH_3}$ *that is a twisting mode that mainly involves* CH_3 *and its neighboring* CH_2CH_2*, (6)* $S_{NH_3CH_2-CH_2-CH_2CH_3}$ *that is a symmetric stretching mode in which* NH_3CH_2 *and* CH_2CH_3 *move in the opposite directions along the longitudinal axis of the molecule, (7)* $B_{NH_3CH_2-CH_2-CH_2CH_3}^{A}$ *that is an antisymmetric bending mode in which* NH_3CH_2 *and* CH_2CH_3 *bend asymmetrically, pushing the* CH_2 *at the center in and out, and (8)* $T_{CH_2-CH_2-CH_2-CH_3}$ *that is an antisymmetric twisting mode of four parts,* CH_2*,* CH_2*,* CH_2 *and* CH_3*, with the motion of* NH_3 *negligible. Each experimental peak corresponds to eight nearly degenerate modes in* $(BA)_2PbI_4$*, which corresponds to the eight* BA^+ *molecules in a unit cell.* $\hbar\omega_{exp}$ *is the experimentally determined phonon energy of some selected phonon peaks. The calculated energy for each phonon peak listed is the averaged value of each set of its corresponding eight nearly degenerate modes,* $\hbar\omega_{avg}^{calc}$*, and their standard deviation in the parenthesis.* $\Delta\hbar\omega$ *is the difference between the calculated and experimental phonon energies,* $\Delta\hbar\omega = \left|\hbar\omega_{avg}^{calc} - \hbar\omega_{exp}\right|$.

Table 13. Selected Vibrational Mode Energies of $MAPbI_3$.

Phonon Mode	Calculated Phonon Energy (meV)						Experimental Peak Position (meV)
	Isolated MA^+		$MAPbI_3$				
	vdW-DF2		w/o vdW		vdW-DF2		
	$\hbar\omega_{avg}^{calc}$	$\Delta\hbar\omega$	$\hbar\omega_{avg}^{calc}$	$\Delta\hbar\omega$	$\hbar\omega_{avg}^{calc}$	$\Delta\hbar\omega$	$\hbar\omega_{exp}$
$12L_{(010)}$	N/A	N/A	10(1)	2	12(1)	0	11.7(1)
$11L_{N-C,(101)}$	N/A	N/A	11(2)	1	12(1)	0	
$1L_{NC,(101)}$	N/A	N/A	8(0)	3	11(0)	1	
$5L_{N,(010)}$	N/A	N/A	12.9(5)	2.5	14.9(5)	0.5	15.4(1)
$2L_{NC,(101)}$	N/A	N/A	13.6(5)	1.8	15.6(3)	0.2	
$4L_{N,(101)}$	N/A	N/A	16.7(1)	1.5	17.9(3)	0.3	18.2(1)
$4L_{C,(101)}$	N/A	N/A	19.1(9)	4.0	22.0(8)	1.1	23.1(1)
$4L_{C,(010)}$	N/A	N/A	20.4(3)	2.7	22.6(2)	0.5	
$4T_{NH_3-CH_3}$	34.0	4.2	46.7(2)	8.5	38.6(2)	0.4	38.2(1)

Eigen energies of the vibrational modes of $MAPbI_3$ (orthorhombic $Pnma$ phase) that are labelled as 1 - 8 in Figure 29 were calculated using two settings: PBE functional without vdW correction, and with vdW-DF2 correction. Corresponding phonon energies for the isolated MA^+ molecule were also calculated for comparison. All calculations were performed at the Γ point ($\boldsymbol{q} = (0, 0, 0)$). The eight phonon modes are the following: (1) $L_{(010)}$ that is a libration mode of MA^+ along the (010) axis, (2) $L_{N-C,(101)}$ that is a libration mode of MA^+ along the (101) axis passing through the N-C axis, (3) $L_{N,(010)}$ that is a libration mode of MA^+ along the (010) axis passing through the N atom, (4) $L_{NC,(101)}$ that is a libration mode along the (101) axis passing through the center of N-C bond, (5) $L_{N,(101)}$ that is a libration mode along the (101) axis passing through the N atom, (6) $L_{C,(101)}$ that is a libration mode along the (101) axis passing through the C atom, (7) $L_{C,(010)}$ that is a libration mode along the (010) axis passing through the C atom, and (8) $T_{NH_3-CH_3}$ that is an antisymmetric twisting mode of two parts, NH_3 and CH_3. Only $T_{NH_3-CH_3}$ involves significant intra-molecule motions and has four nearly degenerated modes. The other librational modes, in which the MA^+ molecule moves as a rigid body, have one to twelve nearly degenerated modes. It should be noted that these phonon modes, especially the libration modes, also involve the vibrations from inorganic atoms.

Table 14. Pb-I-Pb Bending and Pb-I Stretching Modes of $(BA)_2PbI_4$.

16: Bend (z, xy) 3.88 meV	19: Bend (xyz, xyz) 4.15 meV	20: Bend (xyz, xz) 4.33 meV	24: Bend (xyz, xy) 4.85 meV
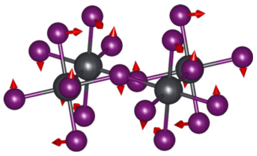	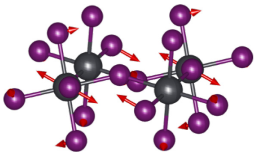	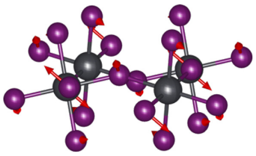	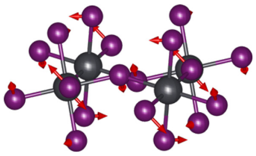
25: Bend (xyz, xy) 4.85 meV	29: Bend (xyz, xz) 5.26 meV	30: Bend (xyz, xyz) 5.48 meV	31: Bend (z, y) 5.64 meV
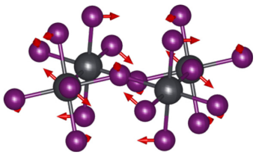	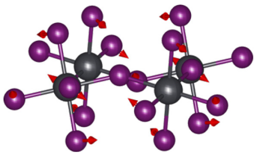	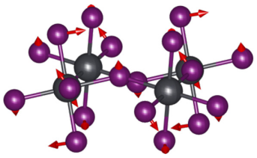	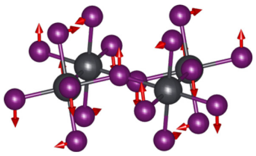
32: Bend (z, y) 5.80 meV	35: Bend (xyz, xy) 6.35 meV	38: Bend (xyz, y) 6.57 meV	52: Bend+Stretch (xy, xyz) 8.82 meV
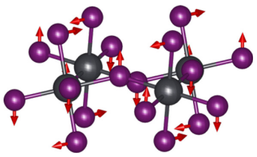	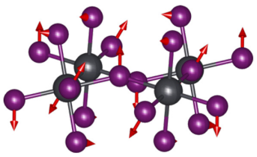	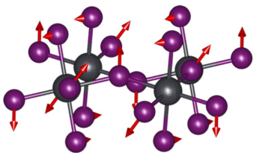	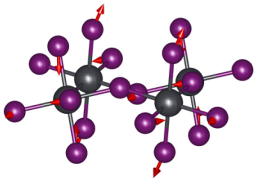
55: Bend+Stretch (xz, yz) 8.91 meV	76: Bend+Stretch (xy, xyz) 11.46 meV	91: Stretch (xy, z) 12.91 meV	92: Stretch (xy, yz) 12.96 meV
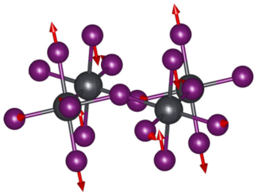	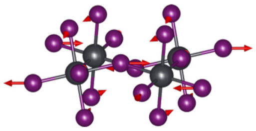	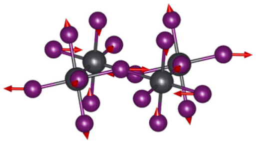	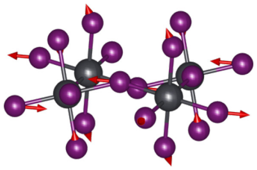

Eigenmodes and eigenenergies of the Pb-I-Pb bending and Pb-I stretching modes of $(BA)_2PbI_4$ ($Pbca$ LT phase), which are obtained from DFT calculations with the vdW-DF2 correction at the phonon $\Gamma(0,0,0)$ point. The phonon mode index, type and energy are listed above each phonon animation figure. The two labels inside parenthesis represent the vibrational direction of the two types of I atoms, i.e., the I atoms (approximately) within the Pb plane and the I atoms out of the Pb plane.

Table 15. Pb-I-Pb Bending and Pb-I Stretching Modes of MAPbI$_3$.

7: Bend (y, x) 2.60 meV	14: Bend (xy, x) 3.69 meV	18: Bend (y, xz) 4.74 meV	19: Bend (y, 0) 4.81 meV
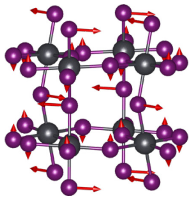	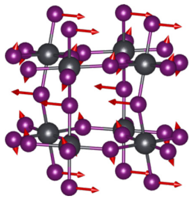	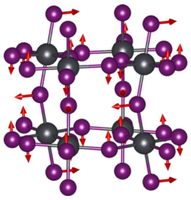	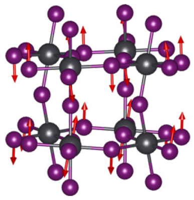
20: Bend (y, 0) 5.30 meV	21: Bend (xzy, z) 5.40 meV	23: Bend (xzy, xz) 5.99 meV	24: Bend (y, z) 6.27 meV
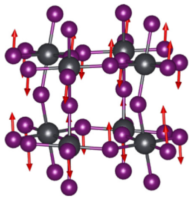	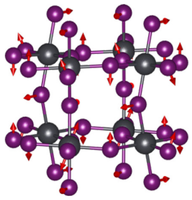	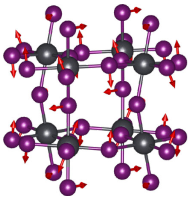	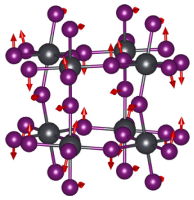
27: Bend (xy, xz) 7.48 meV	28: Bend (xz, 0) 7.59 meV	29: Bend (xz, 0) 7.89 meV	30: Bend (xz, z) 9.57 meV
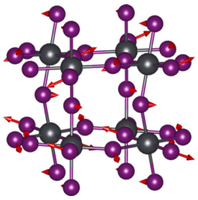	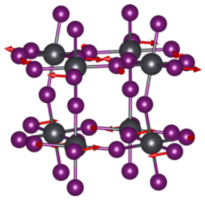	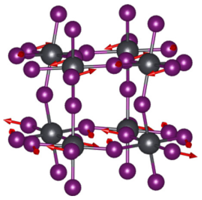	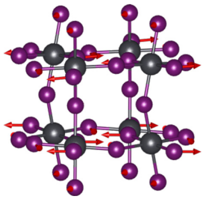
50: Stretch (xz, 0) 13.18 meV	53: Stretch (xz, y) 13.59 meV	58: Stretch (0, y) 15.36 meV	60: Stretch (xz, y) 15.85 meV
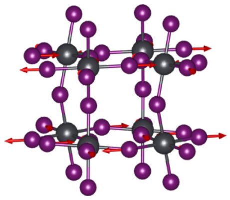	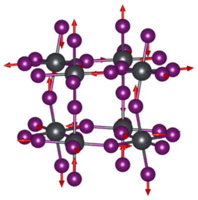	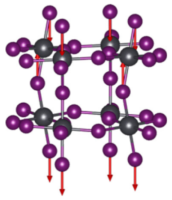	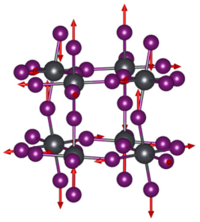

Eigenmodes and eigenenergies of the Pb-I-Pb bending and Pb-I stretching modes of MAPbI$_3$ (orthorhombic $Pnma$ phase), which are obtained from DFT calculations with the vdW-DF2 correction at the phonon $\Gamma(0,0,0)$ point. The phonon mode index, type and energy are listed above each phonon animation figure. The two labels inside parenthesis represent the vibrational direction of the two types of I atoms, i.e., the I atoms (approximately) within the Pb plane and the I atoms out of the Pb plane.

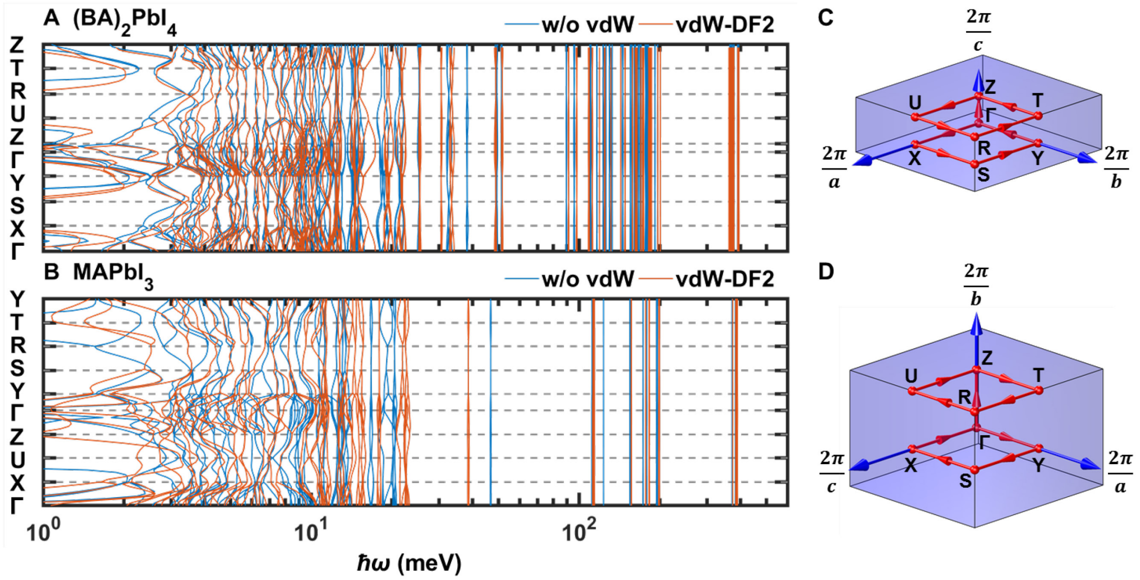

Figure 42.Phonon Band Structures of $(BA)_2PbI_4$ and $MAPbI_3$.

(A and B) the phonon band structures calculated for $(BA)_2PbI_4$ (A) and $MAPbI_3$ (B). (C and D) the high symmetry $\mathbf{q}$*-paths used for phonon band structure calculations for $(BA)_2PbI_4$ (C) and $MAPbI_3$ (D). For $(BA)_2PbI_4$ ($Pbca$ LT phase), the* $\mathbf{q}$*-path is: Γ(0,0,0) → X(1/2,0,0) → S(1/2,1/2,0) → Y(0,1/2,0) → Γ(0,0,0) → Z(0,0,1/2) → U(1/2,0,1/2) → R(1/2,1/2,1/2) → T(0,1/2,1/2) → Z(0,0,1/2). And for $MAPbI_3$ ($Pnma$ phase), the* $\mathbf{q}$*-path is: Γ(0,0,0) → X(1/2,0,0) → U(1/2,0,1/2) → Z(0,0,1/2) → Γ(0,0,0) → Y(0,1/2,0) → S(1/2,1/2,0) → R(1/2,1/2,1/2) → T(0,1/2,1/2) → Y(0,1/2,0).*

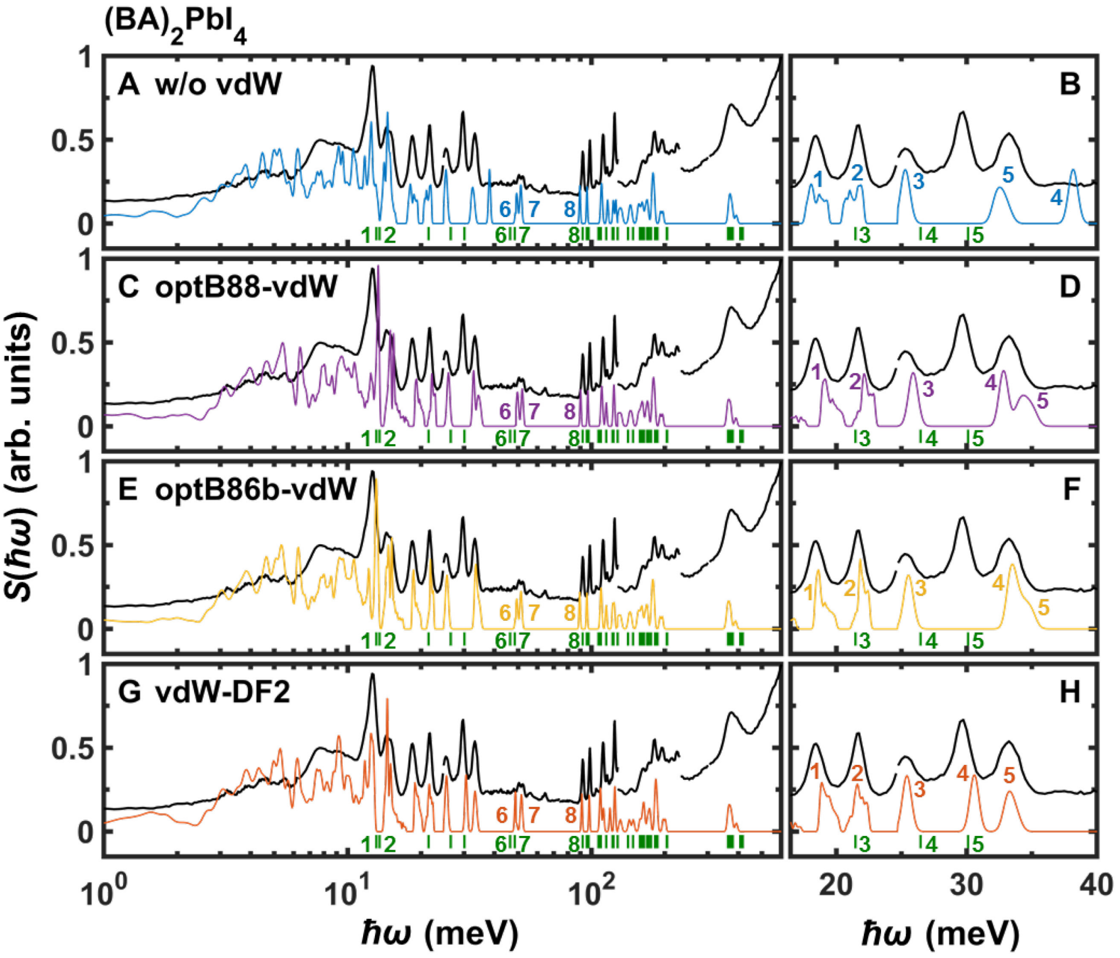

Figure 43.Phonon Density of States with Different vdW Correction Functionals for $(BA)_2PbI_4$.

In (A)(C)(E)(G), the black lines are the Q -integrated INS intensity $S(\hbar\omega) = \int S(Q, \hbar\omega)\, dQ$ *of* $(BA)_2PbI_4$ *measured at 10 K; blue, violet, yellow and red lines show the calculated PDOS without vdW correction, with vdW correction optB88-vdW, optB86b-vdW and vdW-DF2, respectively; dark green marks represent the calculated phonon energies for isolated* BA^+ *molecule at phonon Γ point (*$\boldsymbol{q} = (0,0,0)$*). (B)(D)(F)(H) show the detailed data from 16.5 to 40 meV.*

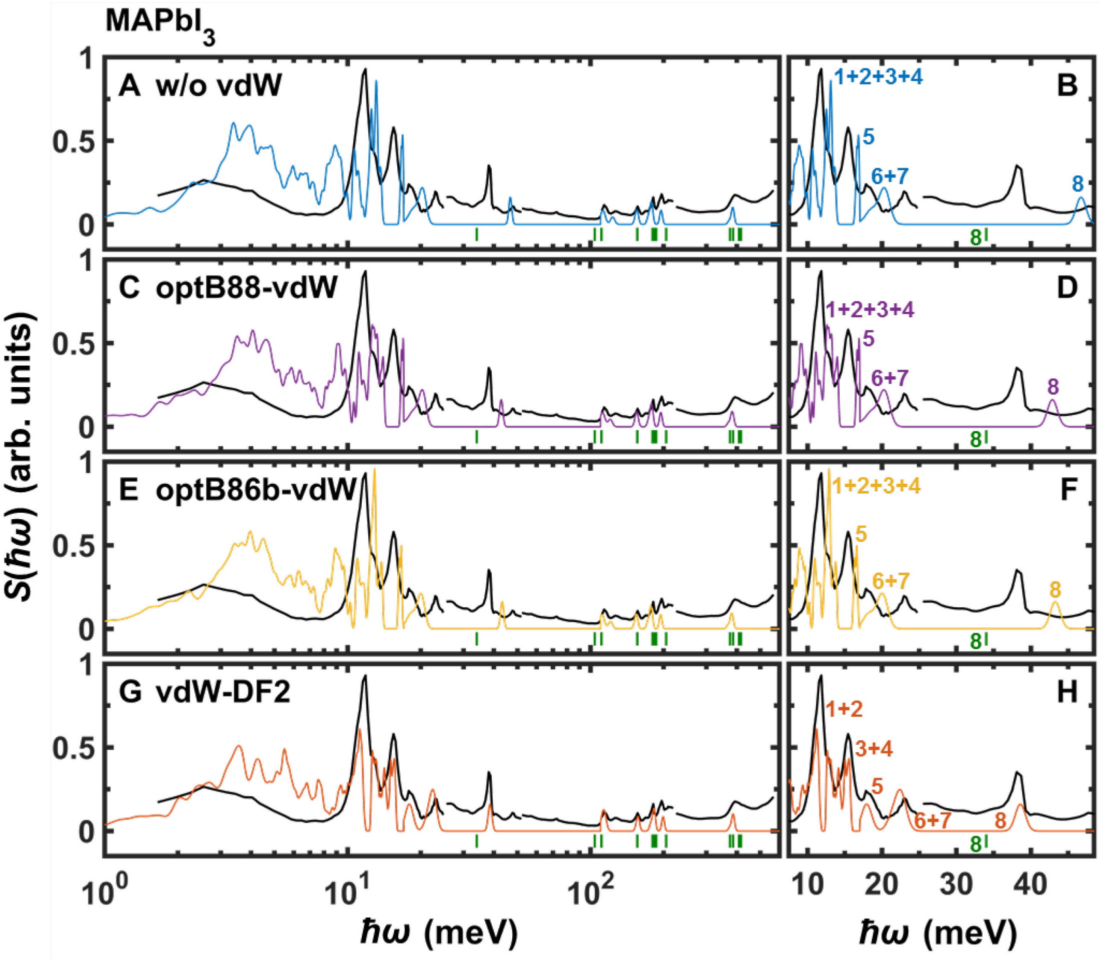

Figure 44.Phonon Density of States with Different vdW Correction Functionals for MAPbI$_3$.

In (A)(C)(E)(G), the black lines are the Q -integrated INS intensity $S(\hbar\omega) = \int S(Q,\hbar\omega)\,dQ$ of MAPbI$_3$ measured at 10 K; blue, violet, yellow and red lines show the calculated PDOS without vdW correction, with vdW correction optB88-vdW, optB86b-vdW and vdW-DF2, respectively; dark green marks represent the calculated phonon energies for isolated MA$^+$ molecule at phonon Γ point ($\boldsymbol{q} = (0,0,0)$). (B)(D)(F)(H) show the detailed data from 7.5 to 48.5 meV.

Table 16. Electronic Interactions Estimated for $(BA)_2PbI_4$.

$A-B$	d_{cm}^{A-B} (Å)	d_{min}^{A-B} (Å)	E_{elec}^{A-B} (eV)	E_{vdW}^{A-B} (eV)
$\mathrm{BA}^{+}(0)-\mathrm{BA}^{+}(1)$ & $\mathrm{BA}^{+}(0)-\mathrm{BA}^{+}(2)$	7.23	4.43	1.119	-0.009
$\mathrm{BA}^{+}(0)-\mathrm{BA}^{+}(3)$ & $\mathrm{BA}^{+}(0)-\mathrm{BA}^{+}(4)$	5.42	2.47	1.108	-0.125
$\mathrm{BA}^{+}(0)-\mathrm{BA}^{+}(5)$ & $\mathrm{BA}^{+}(0)-\mathrm{BA}^{+}(6)$	6.18	2.11	0.665	-0.101
$\mathrm{BA}^{+}(0)-\mathrm{BA}^{+}(7)$ & $\mathrm{BA}^{+}(0)-\mathrm{BA}^{+}(8)$	5.82	2.40	0.676	-0.087
$\mathrm{BA}^{+}(0)-\mathrm{BA}^{+}(9)$	9.38	3.80	1.221	-0.004
$\mathrm{BA}^{+}(0)-\mathrm{BA}^{+}(10)$ & $\mathrm{BA}^{+}(0)-\mathrm{BA}^{+}(11)$	10.73	7.59	0.483	-0.001
$\mathrm{BA}^{+}(0)-\mathrm{BA}^{+}(12)$ & $\mathrm{BA}^{+}(0)-\mathrm{BA}^{+}(13)$	11.64	6.41	0.714	-0.001
$\mathrm{BA}^{+}(0)-[\mathrm{PbI}_4]^{2-}(1)$	4.61	2.60	-6.164	-0.814
$\mathrm{BA}^{+}(0)-[\mathrm{PbI}_4]^{2-}(2)$	8.56	3.49	-2.371	-0.229

The total electronic energy E_{elec}^{A-B} *and the vdW dispersion energy* E_{vdW}^{A-B} *between the subsystem* $A = BA^{+}(0)$ *and* $B = BA^{+}(1)-(13)$, $[PbI_4]^{2-}(1)-(2)$ *were estimated with the vdW-DF2 correction. The distances between the subsystem A and B are also listed, in terms of* d_{cm}^{A-B}*, the distance between the centers of the mass of two subsystems, and* d_{min}^{A-B}*, the distance between the closest atoms in A and B.*

Table 17. Electronic Interactions Estimated for $MAPbI_3$.

$A - B$	d_{cm}^{A-B} (Å)	d_{min}^{A-B} (Å)	E_{elec}^{A-B} (eV)	E_{vdW}^{A-B} (eV)
$MA^+(0) - MA^+(1)$ & $MA^+(0) - MA^+(2)$	6.49	4.75	1.324	-0.002
$MA^+(0) - MA^+(3)$ & $MA^+(0) - MA^+(4)$	5.70	3.92	1.340	-0.007
$MA^+(0) - MA^+(5)$ & $MA^+(0) - MA^+(6)$	6.29	4.60	1.252	-0.002
$MA^+(0) - [PbI_3]^-(1)$	N/A	2.54	-6.784	-0.912

The total electronic energy E_{elec}^{A-B} and the vdW dispersion energy E_{vdW}^{A-B} between the subsystem $A = MA^+(0)$ and $B = MA^+(1) - (6)$, $[PbI_3]^-(1)$ were estimated with the vdW-DF2 correction.

Table 18. Chemical Bonds in HOIPs, NaCl and SiO_2.

System	Chemical Bond			
	Atom Pair	Length (Å)	Energy (eV)	Bond Type
HOIPs	Pb-I	3.25	2.99	Ionic
	I-H	2.63	3.20	
NaCl	Na-Cl	2.85	3.95	
SiO_2	Si-O	1.73	9.95	Covalent

The chemical bond information for HOIPs, NaCl and SiO_2 are listed below. The bond lengths between atom pairs $X - Y$ are extracted from the crystal structures for these three types of systems. And the binding energy of bond $X - Y$ is $E_b(X - Y) = E(X) + E(Y) - E(XY)$, where $E(X)$, $E(Y)$ and $E(XY)$ are the total electronic energy of single X, Y atoms and $X - Y$ pairs, which are obtained from density-functional theory (DFT) calculations. Based on the magnitude of bond energies, we can assign the Pb-I, I-H bonds in HOIPs to be weak ionic bonds, same as the Na-Cl bonds in the NaCl lattice. While the Si-O bonds in the SiO_2 lattice are strong covalent bonds.

References

1. Brenner, T.M., et al., *Hybrid organic—inorganic perovskites: low-cost semiconductors with intriguing charge-transport properties.* Nature Reviews Materials, 2016. **1**: p. 15007.
2. NREL, *Best Research-Cell Efficiencies*. 2019, National Renewable Energy Laboratory.
3. Bi, D., et al., *Polymer-templated nucleation and crystal growth of perovskite films for solar cells with efficiency greater than 21%.* Nature Energy, 2016. **1**(10): p. 16142.
4. Jung, E.H., et al., *Efficient, stable and scalable perovskite solar cells using poly (3-hexylthiophene).* Nature, 2019. **567**(7749): p. 511.
5. Tong, J., et al., *Carrier lifetimes of> 1 μs in Sn-Pb perovskites enable efficient all-perovskite tandem solar cells.* Science, 2019. **364**(6439): p. 475-479.
6. Yang, W.S., et al., *Iodide management in formamidinium-lead-halide–based perovskite layers for efficient solar cells.* Science, 2017. **356**(6345): p. 1376-1379.
7. Park, N.-G., et al., *Towards stable and commercially available perovskite solar cells.* Nature Energy, 2016. **1**(11): p. 16152.
8. Chen, A.Z., et al., *Origin of vertical orientation in two-dimensional metal halide perovskites and its effect on photovoltaic performance.* Nature communications, 2018. **9**(1): p. 1336.

9. Shi, D., et al., *Low trap-state density and long carrier diffusion in organolead trihalide perovskite single crystals.* Science, 2015. **347**(6221): p. 519-522.
10. Yang, Y., et al., *Observation of a hot-phonon bottleneck in lead-iodide perovskites.* Nature Photonics, 2016. **10**(1): p. 53.
11. Yin, W.J., T. Shi, and Y. Yan, *Unique properties of halide perovskites as possible origins of the superior solar cell performance.* Advanced Materials, 2014. **26**(27): p. 4653-4658.
12. Dong, Q., et al., *Electron-hole diffusion lengths> 175 μm in solution-grown CH3NH3PbI3 single crystals.* Science, 2015. **347**(6225): p. 967-970.
13. Xu, W., et al., *Rational molecular passivation for high-performance perovskite light-emitting diodes.* Nature Photonics, 2019. **13**(6): p. 418.
14. Chen, T., et al., *Origin of long lifetime of band-edge charge carriers in organic–inorganic lead iodide perovskites.* Proceedings of the National Academy of Sciences, 2017. **114**: p. 7519-7524.
15. *Optoelectronic devices and components.* Nature Subjects.
16. Dutta, N.K. and X. Zhang, *Optoelectronic Devices*. 2017: WORLD SCIENTIFIC. 588.
17. Becquerel, A.E., *Mémoire sur les effets électriques produits sous l'influence des rayons solaires.* Comptes rendus de l'Académie des Sciences, 1839. **9**: p. 561-567.
18. Chapin, D.M., C.S. Fuller, and G.L. Pearson, *A new silicon p ‐ n junction photocell for converting solar radiation into electrical power.* Journal of Applied Physics, 1954. **25**(5): p. 676-677.

19. Green, M.A., et al., *Solar cell efficiency tables (version 54).* Progress in Photovoltaics: Research and Applications, 2019. **27**(7): p. 565-575.

20. C., V. *The History Of Solar Power*. Available from: https://www.experience.com/advice/careers/ideas/the-history-of-solar-power/.

21. Round, H.J., *A note on carborundum.* Electrical World, 1907. **49**: p. 309.

22. Lossev, O.V., *Luminous carborundum detector and detection effect and oscillations with crystals.* Philosophical Magazine (Series 7), 1928. **5**: p. 1024–1044.

23. Helfrich, W. and W.G. Schneider, *Recombination Radiation in Anthracene Crystals.* Physical Review Letters, 1965. **14**(7): p. 229-231.

24. Tang, C.W. and S.A. VanSlyke, *Organic electroluminescent diodes.* Applied Physics Letters, 1987. **51**(12): p. 913-915.

25. Donohoo, P., et al., *The Future Arrives for Five Clean Energy Technologies - 2016 Update.* U.S. Department of Energy, 2016.

26. Berry, J., et al., *Hybrid Organic–Inorganic Perovskites (HOIPs): Opportunities and Challenges.* Advanced Materials, 2015. **27**(35): p. 5102-5112.

27. Stranks, S.D. and H.J. Snaith, *Metal-halide perovskites for photovoltaic and light-emitting devices.* Nature Nanotechnology, 2015. **10**: p. 391.

28. Huang, J., et al., *Understanding the physical properties of hybrid perovskites for photovoltaic applications.* Nature Reviews Materials, 2017. **2**(7): p. 17042.

29. Li, W., et al., *Chemically diverse and multifunctional hybrid organic–inorganic perovskites.* Nature Reviews Materials, 2017. **2**(3): p. 16099.

30. Wehrenfennig, C., et al., *High Charge Carrier Mobilities and Lifetimes in Organolead Trihalide Perovskites.* Advanced Materials, 2014. **26**(10): p. 1584-1589.

31. Weber, D., *CH3NH3PbX3, ein Pb (II)-system mit kubischer perowskitstruktur/CH3NH3PbX3, a Pb (II)-system with cubic perovskite structure.* Zeitschrift für Naturforschung B, 1978. **33**(12): p. 1443-1445.

32. Era, M., et al., *Organic‐inorganic heterostructure electroluminescent device using a layered perovskite semiconductor (C6H5C2H4NH3)2PbI4.* Applied Physics Letters, 1994. **65**(6): p. 676-678.

33. Kojima, A., et al., *Organometal Halide Perovskites as Visible-Light Sensitizers for Photovoltaic Cells.* Journal of the American Chemical Society, 2009. **131**(17): p. 6050-6051.

34. Lee, M.M., et al., *Efficient hybrid solar cells based on meso-superstructured organometal halide perovskites.* Science, 2012. **338**(6107): p. 643-647.

35. Burschka, J., et al., *Sequential deposition as a route to high-performance perovskite-sensitized solar cells.* Nature, 2013. **499**(7458): p. 316.

36. MØLler, C.K., *Crystal Structure and Photoconductivity of Cæsium Plumbohalides.* Nature, 1958. **182**(4647): p. 1436-1436.

37. Wang, K., et al., *All-inorganic cesium lead iodide perovskite solar cells with stabilized efficiency beyond 15%.* Nature communications, 2018. **9**(1): p. 4544.

38. Wang, K., et al., *Chlorine doping for black γ-CsPbI3 solar cells with stabilized efficiency beyond 16%.* Nano Energy, 2019. **58**: p. 175-182.

39. Stoumpos, C.C., et al., *Ruddlesden–Popper hybrid lead iodide perovskite 2D homologous semiconductors.* Chemistry of Materials, 2016. **28**(8): p. 2852-2867.

40. Billing, D.G. and A. Lemmerer, *Synthesis, characterization and phase transitions in the inorganic–organic layered perovskite-type hybrids [(CnH2n+ 1NH3) 2PbI4], n= 4, 5 and 6.* Acta Crystallographica Section B: Structural Science, 2007. **63**(5): p. 735-747.

41. Billing, D.G. and A. Lemmerer, *Synthesis, characterization and phase transitions of the inorganic–organic layered perovskite-type hybrids [(C n H 2n+ 1 NH 3) 2 PbI 4](n= 12, 14, 16 and 18).* New Journal of Chemistry, 2008. **32**(10): p. 1736-1746.

42. Dolzhenko, Y.I., T. Inabe, and Y. Maruyama, *In situ X-ray observation on the intercalation of weak interaction molecules into perovskite-type layered crystals (C9H19NH3) 2PbI4 and (C10H21NH3) 2CdCl4.* Bulletin of the Chemical Society of Japan, 1986. **59**(2): p. 563-567.

43. Shockley, W. and H.J. Queisser, *Detailed Balance Limit of Efficiency of p ‐ n Junction Solar Cells.* Journal of Applied Physics, 1961. **32**(3): p. 510-519.

44. Rühle, S., *Tabulated values of the Shockley–Queisser limit for single junction solar cells.* Solar Energy, 2016. **130**: p. 139-147.

45. Wikipedia. *Shockley–Queisser limit*. Available from: https://en.wikipedia.org/wiki/Shockley%E2%80%93Queisser_limit.

46. Chen, A.Z., et al., *Understanding the Formation of Vertical Orientation in Two-dimensional Metal Halide Perovskite Thin Films.* Chemistry of Materials, 2019. **31**(4): p. 1336-1343.

47. Smith, I.C., et al., *A layered hybrid perovskite solar ‐cell absorber with enhanced moisture stability.* Angewandte Chemie International Edition, 2014. **53**(42): p. 11232-11235.

48. Zuo, C., et al., *Self-Assembled 2D Perovskite Layers for Efficient Printable Solar Cells.* Advanced Energy Materials, 2019. **9**(4): p. 1803258.

49. Ye, J., et al., *Enhanced Moisture Stability of Perovskite Solar Cells With Mixed-Dimensional and Mixed-Compositional Light-Absorbing Materials.* Solar RRL, 2017. **1**(11): p. 1700125.

50. Lin, Y., et al., *Enhanced thermal stability in perovskite solar cells by assembling 2D/3D stacking structures.* The journal of physical chemistry letters, 2018. **9**(3): p. 654-658.

51. Tsai, H., et al., *High-efficiency two-dimensional Ruddlesden–Popper perovskite solar cells.* Nature, 2016. **536**(7616): p. 312.

52. Blancon, J.C., et al., *Scaling law for excitons in 2D perovskite quantum wells.* Nature communications, 2018. **9**(1): p. 2254.

53. Yang, X., et al., *Efficient green light-emitting diodes based on quasi-two-dimensional composition and phase engineered perovskite with surface passivation.* Nature Communications, 2018. **9**(1): p. 570.

54. Cho, H., et al., *Overcoming the electroluminescence efficiency limitations of perovskite light-emitting diodes.* Science, 2015. **350**(6265): p. 1222.

55. Chen, Z., et al., *Single-Crystal MAPbI3 Perovskite Solar Cells Exceeding 21% Power Conversion Efficiency.* ACS Energy Letters, 2019. **4**(6): p. 1258-1259.

56. Stoumpos, C.C., C.D. Malliakas, and M.G. Kanatzidis, *Semiconducting Tin and Lead Iodide Perovskites with Organic Cations: Phase Transitions, High Mobilities, and Near-Infrared Photoluminescent Properties.* Inorganic Chemistry, 2013. **52**(15): p. 9019-9038.
57. Baikie, T., et al., *Synthesis and crystal chemistry of the hybrid perovskite (CH 3 NH 3) PbI 3 for solid-state sensitised solar cell applications.* Journal of Materials Chemistry A, 2013. **1**(18): p. 5628-5641.
58. Chen, T., et al., *Rotational dynamics of organic cations in the CH 3 NH 3 PbI 3 perovskite.* Physical Chemistry Chemical Physics, 2015. **17**(46): p. 31278-31286.
59. Juarez-Perez, E.J., et al., *Photoinduced giant dielectric constant in lead halide perovskite solar cells.* The journal of physical chemistry letters, 2014. **5**(13): p. 2390-2394.
60. Foley, B.J., et al., *Temperature dependent energy levels of methylammonium lead iodide perovskite.* Applied Physics Letters, 2015. **106**(24): p. 243904.
61. Yamada, Y., et al., *Near-band-edge optical responses of solution-processed organic–inorganic hybrid perovskite CH3NH3PbI3 on mesoporous TiO2 electrodes.* Applied Physics Express, 2014. **7**(3): p. 032302.
62. Snaith, H.J., *Perovskites: the emergence of a new era for low-cost, high-efficiency solar cells.* The journal of physical chemistry letters, 2013. **4**(21): p. 3623-3630.
63. Buin, A., et al., *Materials processing routes to trap-free halide perovskites.* Nano letters, 2014. **14**(11): p. 6281-6286.

64. Stranks, S.D., et al., *Electron-Hole Diffusion Lengths Exceeding 1 Micrometer in an Organometal Trihalide Perovskite Absorber.* Science, 2013. **342**(6156): p. 341-344.

65. Xing, G., et al., *Long-range balanced electron-and hole-transport lengths in organic-inorganic CH3NH3PbI3.* Science, 2013. **342**(6156): p. 344-347.

66. Gottesman, R., et al., *Extremely slow photoconductivity response of CH3NH3PbI3 perovskites suggesting structural changes under working conditions.* The journal of physical chemistry letters, 2014. **5**(15): p. 2662-2669.

67. Kutes, Y., et al., *Direct observation of ferroelectric domains in solution-processed CH3NH3PbI3 perovskite thin films.* The journal of physical chemistry letters, 2014. **5**(19): p. 3335-3339.

68. Yaffe, O., et al., *Local polar fluctuations in lead halide perovskite crystals.* Physical review letters, 2017. **118**(13): p. 136001.

69. Miyata, K., T.L. Atallah, and X.Y. Zhu, *Lead halide perovskites: Crystal-liquid duality, phonon glass electron crystals, and large polaron formation.* Science advances, 2017. **3**(10): p. e1701469.

70. Raghavan, C.M., et al., *Low-Threshold Lasing from 2D Homologous Organic–Inorganic Hybrid Ruddlesden–Popper Perovskite Single Crystals.* Nano letters, 2018. **18**(5): p. 3221-3228.

71. Zhu, H., et al., *Screening in crystalline liquids protects energetic carriers in hybrid perovskites.* Science, 2016. **353**(6306): p. 1409-1413.

72. Squires, G.L., *Introduction to the theory of thermal neutron scattering*. 2012: Cambridge university press.

73. Bée, M., *Quasielastic Neutron Scattering: Principles and Applications in Solid State Chemistry, Biology and Materials Science.* Bristol and Philadelphia: Adam Hilger, 1988.

74. Chen, T., et al., *Entropy-driven structural transition and kinetic trapping in formamidinium lead iodide perovskite.* Science advances, 2016. **2**(10): p. e1601650.

75. Sears, V.F., *Neutron scattering lengths and cross sections.* Neutron news, 1992. **3**(3): p. 26-37.

76. Majkrzak, C.F. and S.-H. Lee. *Spin Polarized Inelastic Neutron Spectrometer*. Available from: https://www.ncnr.nist.gov/spins.html.

77. Brown, C.M. *BT-1 High Resolution Powder Diffractometer Instrument Plan*. Available from: https://www.ncnr.nist.gov/instruments/bt1/bt1_plan.html.

78. Azuah, R.T., et al., *DAVE: a comprehensive software suite for the reduction, visualization, and analysis of low energy neutron spectroscopic data.* Journal of Research of the National Institute of Standards and Technology, 2009. **114**(6): p. 341.

79. Kajimoto, R., et al., *The Fermi chopper spectrometer 4SEASONS at J-PARC.* Journal of the Physical Society of Japan, 2011. **80**(Suppl. B): p. SB025.

80. Nakajima, K., et al., *AMATERAS: a cold-neutron disk chopper spectrometer.* Journal of the Physical Society of Japan, 2011. **80**(Suppl. B): p. SB028.

81. Seto, H., et al., *Inelastic and quasi-elastic neutron scattering spectrometers in J-PARC.* Biochimica et Biophysica Acta (BBA)-General Subjects, 2017. **1861**(1): p. 3651-3660.

82. Nakamura, M., et al., *First demonstration of novel method for inelastic neutron scattering measurement utilizing multiple incident energies.* Journal of the Physical Society of Japan, 2009. **78**(9): p. 093002-093002.

83. Abernathy, D.L., et al., *Design and operation of the wide angular-range chopper spectrometer ARCS at the Spallation Neutron Source.* Review of Scientific Instruments, 2012. **83**(1): p. 015114.

84. Inamura, Y., et al., *Development status of software "Utsusemi" for chopper spectrometers at MLF, J-PARC.* Journal of the Physical Society of Japan, 2013. **82**(Suppl. A): p. SA031.

85. Pelant, I. and J. Valenta, *Luminescence spectroscopy of semiconductors*. 2012: Oxford University Press.

86. Valenta, J., *Photoluminescence Characterization of Selected Semiconductors and Insulators.* 1994.

87. Letzter, S., *ADVANCES IN BOXCAR AVERAGING USING DIGITAL-TECHNIQUES.* LASER FOCUS-ELECTRO-OPTICS, 1983. **19**(12): p. 77.

88. Wikipedia. *Density functional theory*. Available from: https://en.wikipedia.org/wiki/Density_functional_theory.

89. Kresse, G. and J. Furthmüller, *Efficient iterative schemes for ab initio total-energy calculations using a plane-wave basis set.* Physical review B, 1996. **54**(16): p. 11169.

90. Kresse, G. and D. Joubert, *From ultrasoft pseudopotentials to the projector augmented-wave method.* Physical Review B, 1999. **59**(3): p. 1758.

91. Perdew, J.P., K. Burke, and M. Ernzerhof, *Generalized gradient approximation made simple.* Physical review letters, 1996. **77**(18): p. 3865.

92. Kresse, G., J. Furthmüller, and J. Hafner, *Ab initio force constant approach to phonon dispersion relations of diamond and graphite.* EPL (Europhysics Letters), 1995. **32**(9): p. 729.

93. Parlinski, K., Z.Q. Li, and Y. Kawazoe, *First-principles determination of the soft mode in cubic ZrO 2.* Physical Review Letters, 1997. **78**(21): p. 4063.

94. Togo, A. and I. Tanaka, *First principles phonon calculations in materials science.* Scripta Materialia, 2015. **108**: p. 1-5.

95. Dion, M., et al., *Van der Waals density functional for general geometries.* Physical review letters, 2004. **92**(24): p. 246401.

96. Román-Pérez, G. and J.M. Soler, *Efficient implementation of a van der Waals density functional: application to double-wall carbon nanotubes.* Physical review letters, 2009. **103**(9): p. 096102.

97. Klimeš, J., D.R. Bowler, and A. Michaelides, *Van der Waals density functionals applied to solids.* Physical Review B, 2011. **83**(19): p. 195131.

98. Lee, K., et al., *Higher-accuracy van der Waals density functional.* Physical Review B, 2010. **82**(8): p. 081101.

99. Cheng, Y.Q., et al., *Simulation of inelastic neutron scattering spectra using OCLIMAX.* Journal of chemical theory and computation, 2019. **15**(3): p. 1974-1982.

100. Larson, A.C. and R.B. Von Dreele, *Gsas.* Report lAUR, 1994: p. 86-748.

101. Toby, B.H., *EXPGUI, a graphical user interface for GSAS.* Journal of applied crystallography, 2001. **34**(2): p. 210-213.

102. Von Dreele, R.B., *Combined Rietveld and stereochemical restraint refinement of a protein crystal structure.* Journal of applied crystallography, 1999. **32**(6): p. 1084-1089.

103. Rietveld, H., *A profile refinement method for nuclear and magnetic structures.* Journal of applied Crystallography, 1969. **2**(2): p. 65-71.

104. Zhu, X.Y. and V. Podzorov, *Charge carriers in hybrid organic–inorganic lead halide perovskites might be protected as large polarons.* ACS Publications, 2015.

105. Miyata, K., et al., *Large polarons in lead halide perovskites.* Science advances, 2017. **3**(8): p. e1701217.

106. Miyata, K. and X.Y. Zhu, *Ferroelectric large polarons.* Nature materials, 2018. **17**(5): p. 379.

107. Zheng, F. and L.-W. Wang, *Large Polaron Formation and its Effect on Electron Transport in Hybrid Perovskite.* Energy & Environmental Science, 2019.

108. Frost, J.M., L.D. Whalley, and A. Walsh, *Slow cooling of hot polarons in halide perovskite solar cells.* ACS energy letters, 2017. **2**(12): p. 2647-2652.

109. Cortecchia, D., et al., *Polaron self-localization in white-light emitting hybrid perovskites.* Journal of Materials Chemistry C, 2017. **5**(11): p. 2771-2780.

110. Neukirch, A.J., et al., *Polaron stabilization by cooperative lattice distortion and cation rotations in hybrid perovskite materials.* Nano letters, 2016. **16**(6): p. 3809-3816.

111. Ni, L., et al., *Real-Time Observation of Exciton–Phonon Coupling Dynamics in Self-Assembled Hybrid Perovskite Quantum Wells.* ACS nano, 2017. **11**(11): p. 10834-10843.

112. Thouin, F., et al., *Stable biexcitons in two-dimensional metal-halide perovskites with strong dynamic lattice disorder.* Physical Review Materials, 2018. **2**(3): p. 034001.

113. Mao, L., et al., *Tunable White-Light Emission in Single-Cation-Templated Three-Layered 2D Perovskites (CH3CH2NH3) 4Pb3Br10–x Cl x.* Journal of the American Chemical Society, 2017. **139**(34): p. 11956-11963.

114. Hu, T., et al., *Mechanism for broadband white-light emission from two-dimensional (110) hybrid perovskites.* The journal of physical chemistry letters, 2016. **7**(12): p. 2258-2263.

115. Smith, M.D., et al., *Structural origins of broadband emission from layered Pb–Br hybrid perovskites.* Chemical science, 2017. **8**(6): p. 4497-4504.

116. Guo, D., et al., *Photoluminescence from radiative surface states and excitons in methylammonium lead bromide perovskites.* The journal of physical chemistry letters, 2017. **8**(17): p. 4258-4263.

117. Wright, A.D., et al., *Electron–phonon coupling in hybrid lead halide perovskites.* Nature communications, 2016. **7**: p. 11755.

118. Fang, H.H., et al., *Exciton recombination in formamidinium lead triiodide: nanocrystals versus thin films.* small, 2017. **13**(32): p. 1700673.

119. Tombe, S., et al., *Optical and electronic properties of mixed halide (X= I, Cl, Br) methylammonium lead perovskite solar cells.* Journal of Materials Chemistry C, 2017. **5**(7): p. 1714-1723.

120. Wu, K., et al., *Temperature-dependent excitonic photoluminescence of hybrid organometal halide perovskite films.* Physical Chemistry Chemical Physics, 2014. **16**(41): p. 22476-22481.

121. Guo, Z., et al., *Electron–phonon scattering in atomically thin 2D perovskites.* ACS nano, 2016. **10**(11): p. 9992-9998.

122. Gong, X., et al., *Electron–phonon interaction in efficient perovskite blue emitters.* Nature materials, 2018. **17**(6): p. 550.

123. Chen, Y., et al., *Extended carrier lifetimes and diffusion in hybrid perovskites revealed by Hall effect and photoconductivity measurements.* Nature communications, 2016. **7**: p. 12253.

124. Joshi, P.P., S.F. Maehrlein, and X. Zhu, *Dynamic Screening and Slow Cooling of Hot Carriers in Lead Halide Perovskites.* Advanced Materials, 2019: p. 1803054.

125. Thouin, F., et al., *Phonon coherences reveal the polaronic character of excitons in two-dimensional lead halide perovskites.* Nature materials, 2019: p. 1.

126. Yin, J., et al., *Excitonic and polaronic properties of 2D hybrid organic–inorganic perovskites.* ACS Energy Letters, 2017. **2**(2): p. 417-423.

127. Neutzner, S., et al., *Exciton-polaron spectral structures in two-dimensional hybrid lead-halide perovskites.* Physical Review Materials, 2018. **2**(6): p. 064605.

128. Liang, W.Y., *Excitons.* Physics Education, 1970. **5**(4): p. 226.

129. Pope, M. and C.E. Swenberg, *Electronic processes in organic crystals and polymers*. 1999: Oxford University Press on Demand.

130. Onoda-Yamamuro, N., T. Matsuo, and H. Suga, *Dielectric study of CH3NH3PbX3 (X= Cl, Br, I).* Journal of Physics and Chemistry of Solids, 1992. **53**(7): p. 935-939.

131. Collaboration: Authors and editors of the volumes, I.I.I.A.A.A.a., *Silicon (Si) high-frequency dielectric constant.* Group IV Elements, IV-IV and III-V Compounds. Part a-Lattice Properties, 2001: p. 1-7.

132. Yang, Z., et al., *Unraveling the exciton binding energy and the dielectric constant in single-crystal methylammonium lead triiodide perovskite.* The journal of physical chemistry letters, 2017. **8**(8): p. 1851-1855.

133. Stoumpos, C.C., et al., *High members of the 2D Ruddlesden-Popper halide perovskites: synthesis, optical properties, and solar cells of (CH3 (CH2) 3NH3) 2 (CH3NH3) 4Pb5I16.* Chem, 2017. **2**(3): p. 427-440.

134. Saparov, B. and D.B. Mitzi, *Organic–inorganic perovskites: structural versatility for functional materials design.* Chemical reviews, 2016. **116**(7): p. 4558-4596.

135. Landau, L.D., *On the motion of electrons in a crystal lattice.* Phys. Z. Sowjetunion, 1933. **3**: p. 664.

136. Holstein, T., *Studies of polaron motion: Part I. The molecular-crystal model.* Annals of physics, 1959. **8**(3): p. 325-342.

137. Fröhlich, H., *Electrons in lattice fields.* Advances in Physics, 1954. **3**(11): p. 325-361.

138. Feynman, R.P., *Slow electrons in a polar crystal.* Physical Review, 1955. **97**(3): p. 660.

139. Emin, D., *Polarons*. 2012, Cambridge: Cambridge University Press.

140. Devreese, J.T., *Polarons.* Encycl. Appl. Phys., 1996. **14**(cond-mat/0004497): p. 383-409.

141. Kim, H., et al., *Direct observation of mode-specific phonon-band gap coupling in methylammonium lead halide perovskites.* Nature communications, 2017. **8**(1): p. 687.

142. Data, P.F.-G.F.D., *Analysis Software*. 2015, Version.

143. Miyata, A., et al., *Direct measurement of the exciton binding energy and effective masses for charge carriers in organic–inorganic tri-halide perovskites.* Nature Physics, 2015. **11**(7): p. 582.

144. Drużbicki, K., et al., *Unexpected cation dynamics in the low-temperature phase of methylammonium lead iodide: the need for improved models.* The journal of physical chemistry letters, 2016. **7**(22): p. 4701-4709.

145. Li, B., et al., *Polar rotor scattering as atomic-level origin of low mobility and thermal conductivity of perovskite CH 3 NH 3 PbI 3.* Nature communications, 2017. **8**: p. 16086.

146. Grimme, S., *Semiempirical GGA ‐type density functional constructed with a long ‐range dispersion correction.* Journal of computational chemistry, 2006. **27**(15): p. 1787-1799.

147. Park, M., et al., *Excited-state vibrational dynamics toward the polaron in methylammonium lead iodide perovskite.* Nature communications, 2018. **9**(1): p. 2525.

148. Pérez-Osorio, M.A., et al., *Vibrational properties of the organic–inorganic halide perovskite CH3NH3PbI3 from theory and experiment: factor group analysis, first-principles calculations, and low-temperature infrared spectra.* The Journal of Physical Chemistry C, 2015. **119**(46): p. 25703-25718.

149. Schlipf, M., S. Poncé, and F. Giustino, *Carrier Lifetimes and Polaronic Mass Enhancement in the Hybrid Halide Perovskite CH 3 NH 3 PbI 3 from Multiphonon Fröhlich Coupling.* Physical review letters, 2018. **121**(8): p. 086402.

150. Takabatake, T., et al., *Phonon-glass electron-crystal thermoelectric clathrates: Experiments and theory.* Reviews of Modern Physics, 2014. **86**(2): p. 669-716.

151. Rowe, D.M., *CRC handbook of thermoelectrics*. 1995: CRC press.

152. Niesner, D., et al., *Persistent energetic electrons in methylammonium lead iodide perovskite thin films.* Journal of the American Chemical Society, 2016. **138**(48): p. 15717-15726.

153. Whalley, L.D., et al., *Phonon anharmonicity, lifetimes, and thermal transport in CH 3 NH 3 PbI 3 from many-body perturbation theory.* Physical Review B, 2016. **94**(22): p. 220301.

154. Sutherland, B.R. and E.H. Sargent, *Perovskite photonic sources.* Nature Photonics, 2016. **10**(5): p. 295.

155. Zhang, Y., et al., *Synthesis, properties, and optical applications of low-dimensional perovskites.* Chemical communications, 2016. **52**(94): p. 13637-13655.

156. Oga, H., et al., *Improved understanding of the electronic and energetic landscapes of perovskite solar cells: high local charge carrier mobility, reduced recombination, and extremely shallow traps.* Journal of the American Chemical Society, 2014. **136**(39): p. 13818-13825.

157. Wehrenfennig, C., et al., *Charge-carrier dynamics in vapour-deposited films of the organolead halide perovskite CH 3 NH 3 PbI 3− x Cl x.* Energy & Environmental Science, 2014. **7**(7): p. 2269-2275.